CRANFIELD UNIVERSITY

EBENEZER MAYOWA ADEBAYO

HIGH-ORDER FINITE-VOLUME METHODS FOR COMPRESSIBLE MULTIPHASE FLOWS USING UNSTRUCTURED MESHES

SCHOOL OF AEROSPACE, TRANSPORT AND MANUFACTURING
Centre for Computational Engineering Sciences

PHD THESIS
Academic Year: 2019–2023

Supervisor: Dr Panagiotis Tsoutsanis
March 2023

CRANFIELD UNIVERSITY

SCHOOL OF AEROSPACE, TRANSPORT AND MANUFACTURING
Centre for Computational Engineering Sciences

PHD THESIS

Academic Year: 2019–2023

EBENEZER MAYOWA ADEBAYO

High-Order Finite-Volume Methods for Compressible Multiphase flows using Unstructured Meshes

Supervisor: Dr Panagiotis Tsoutsanis
March 2023

This thesis is submitted in partial fulfilment of the requirements for the degree of PHD THESIS.

© Cranfield University 2023. All rights reserved. No part of this publication may be reproduced without the written permission of the copyright owner.

Abstract

For the simulation of multi-component or multiphase compressible flows, presented in this thesis is a computationally efficient high-resolution numerical methods that capture shocks and interfaces in the finite-volume framework on unstructured grids. The robustness of the CWENO high-order schemes in capturing and resolving the material interface in multi-component or multiphase flows in the presence of strong gradients and material discontinuities with oscillation-free solutions and reduced numerical diffusion is demonstrated using the diffuse interface framework implemented in the open-source unstructured compressible flow `UCNS3D`. The UCNS3D is an in-house code in the finite volume framework written in FORTRAN that is being actively developed by members of Cranfield University. For this research, some additional multiphase features were implemented in the code and continuously improved throughout this thesis.

Stringent two- and three-dimensional compressible multiphase/multi-component test cases, including cavitation, were employed to assess the numerical methods. Results were compared with other high-order methods and existing experiments, demonstrating that CWENO is less dissipative, eliminates spurious oscillations at material boundaries, and provides a high-resolution description of material interfaces with minimal artificial smearing. These findings highlight CWENO's superior capability in accurately simulating complex multiphase or multi-component phenomena in compressible flows.

Contents

Abstract **iii**

Contents **iv**

List of Figures **vi**

List of Tables **xi**

Acknowledgements **xviii**

1 Introduction **2**
1.1 Aims and Objectives 9
1.2 Contributions to the Scientific Knowledge 10
1.2.1 Publications 11
1.3 Thesis Overview 12

2 Literature Review **13**
2.1 Non-equilibrium or Total Disequilibrium Models 18
2.1.1 Baer-Nunziato non-equilibrium model 19
2.1.2 Saurel-Abgrall non-equilibrium model 25
2.1.3 Romenski seven-equation model 27
2.2 Mechanical equilibrium Model 30
2.3 Velocity equilibrium or Pressure-disequilibrium model 37
2.4 Thermal-equilibrium and Mechanical equilibrium of Abgrall et al. 40
2.5 Choice of Equation of State EoS 45
2.5.1 Ideal Gas EoS 46
2.5.2 Tait's EoS 46
2.5.3 Van der Waals gas EoS 47
2.5.4 Stiffened gas EoS 47
2.5.5 Noble Abel Stiffened Gas' (NASG)EoS 48
2.5.6 Mie-Grüneisen EoS 48
2.6 High-order methods for DIM 50

3 Numerical framework **61**
3.1 Finite-volume formulation for the five-equation Models 61
3.2 Spatial discretisation 64
3.3 CWENO Scheme 68

3.4 The Riemann Problem for the Five-equation DIM . . . 71
3.5 Fluxes approximation & Temporal discretization. . . . 75
3.5.1 Harten-Lax-van Leer-Contact (HLLC) Solver . . . 75
3.5.2 Third-order explicit SSP-RK time stepping . . . 77

4 Boundary Conditions 79
4.0.1 Reflective Boundary Conditions . . . 81
4.0.2 Non-Reflecting (Transmissive) Boundary Conditions . . . 82
4.0.3 Periodic Boundary Conditions . . . 83
4.0.4 Inflow (Supersonic) and Outflow (Supersonic) . . . 84

5 Applications and Test Cases 86
5.1 Test Cases I . . . 87
5.1.1 Multi-species advection convergence study . . . 87
5.1.2 Advection of material interface . . . 89
5.1.3 Gas bubble collapse in water . . . 92
5.1.4 Shock-Helium bubble interaction . . . 98
5.2 Cavitation in Underwater Explosion (Test Cases II) . . . 104
5.2.1 Cut-off cavitation model . . . 110
5.2.2 2D underwater explosion near a free surface . . . 112
5.2.3 2D cylindrical underwater explosion near a planar rigid wall. . . . 120
5.2.4 3D underwater explosion in an enclosed, rigid cylindrical wall. . . 125
5.2.5 2D underwater explosion of two bubbles placed horizontally near a free surface . . . 129
5.2.6 3D Underwater of two bubbles placed vertically in an enclosed region. . . . 133

6 Conclusions and Recommendations 141
6.1 Conclusions . . . 141
6.2 Recommendation . . . 142

References 144

A Additional contours for 3D test cases 167

B FORTRAN code of the initial conditions 170
B.1 Multi-species advection convergence study . . . 170
B.2 Advection of contact discontinuity . . . 171
B.3 Gas bubble collapse in water . . . 173
B.4 Shock-Helium bubble interaction . . . 176
B.5 Underwater Explosion near a rigid wall . . . 182
B.6 Underwater Explosion near a free surface . . . 185
B.7 Underwater Explosion in a closed rigid cylinder . . . 187
B.8 Underwater Explosion of two bubbles placed horizontally near a free surface 189

List of Figures

1.1 Two-phase flows (Adapted from [154]). 3
1.2 The interface of compressible multiphase and multi-component flows . . 4

2.1 Diffused-interface models. 17
2.2 The hierarchy of the seven-equation total disequilibrium models. The Romenski model has similarities with the B-N-type model (Saurel-Abgrall) for isentropic cases. 19
2.3 Physical parameters of each fluid in a multiphase/multicomponent flow . 19

3.1 Schematic illustrating the direction normal to the cell interface between the two cells i and j under consideration. (Reproduced from [14]). 63
3.2 Schematic of a quadrilateral cell that has been segmented into triangles for the purpose of transforming it into reference space. (a) Quadrilateral cell (b) Decomposition into two triangles in a reference space. (Adapted from [168]). 65
3.3 The figure shows the stencils used in WENO and CWENO/CWENOZ schemes for P=4, where the red cell represents the cell of interest, and the main portion of the stencil is shown in grey, while the directional stencils are in different colors. It is observed that the directional stencils used in CWENO/Z schemes are smaller than those used in WENO schemes. For more information on interpreting the colors in the figure, please refer to the web version of the article. (Adapted from [14]). 70
3.4 One-dimensional Riemann problem profile of a fluid on the (x,t) plane. . 71
3.5 Schematic diagram of a discontinuous initial data with compressive characteristics on the (x,t) plane. The star region (*) represents the intermediate state. . . 72
3.6 Schematic diagram of a discontinuous initial data with compressive characteristics on the (x,t) plane. The star region (*) represents the intermediate state. . . 74

4.1 1D computational domain showing the N-number of discretization. Two ghost/fictitious cells are added at the end of each boundary. The red dots represent the cell centres. 80
4.2 Schematic diagram showing reflecting boundary condition (left and right side). The two-directional arrows indicates the wave reflected at the boundaries of the given computational domain. 81
4.3 Schematic diagram showing non-reflecting (transmissive) boundary condition (left and right side). The two-directional arrows indicates visually unimpeded wave propagation at the boundaries of the given computational domain. . 82

4.4 Schematic diagram showing periodic boundary conditions (left side). The state variable of cell $(N-1)$ and (N) re-entering into the computational domain from the left boundary 83
4.5 Schematic diagram showing inflow (a) and Outflow (b) boundary conditions. 84

5.1 Multi-species advection convergence study; the plot of computational time against the grid resolution using the CWENO and WENO schemes of varying order of accuracy (on the left). It shows for a given order of accuracy, the CWENO has a lower computational cost than the WENO. The L_2 errors are plotted against the grid resolution to show a convergence (on the right). The CWENO6 as expected is the most accurate. 90
5.2 Advection of a material interface; density contour showing the interface of the two inert gases Ni and He. 92
5.3 Advection of a material interface; here are illustrations of 2D unstructured meshes, comprising a triangular mesh (on the left) and a hybrid mesh (on the right). The zoomed-in area on the right provides a more detailed view of the mesh's structure. 92
5.4 Advection of material interface; the exact solution is represented by the solid line. At time t=2, graphs illustrating the density, temperature, pressure, and velocity were generated using CWENO3 techniques with both conservative and primitive variable reconstructions. It is evident from the velocity and pressure plots that the CWENO conservative variable reconstruction results in artificial oscillations, which are not present in the CWENO primitive variable reconstruction. 93
5.5 Advection of a material interface; the plot with a solid line represents the exact solution. The figures depict the density and temperature at time t = 2 using the CWENO3 and WENO3 methods, with reconstructions based on primitive variables. The results illustrate that the WENO3 schemes produces oscillations around the material interface, which are absent in the CWENO3. 94
5.6 Advection of a material interface; using CWENO schemes of third to sixth order accuracy,the exact solution is represented by a solid line in the temperature and density profiles. The top two figures on the left highlights a zoomed-in view for the marked region. The errors in the pressure and velocity profiles at t = 2 s are presented in the bottom plot for each accuracy order, and it can be observed that the small oscillations are almost at the machine precision level. 95
5.7 Computational domain setup for the gas bubble collapse in water test problem. 96
5.8 Gas bubble collapse test problem; Mach number (contours) and volume fraction (lines) plots at different duration are shown for the CWENO5 scheme. The figures demonstrate that the scheme successfully captures all the anticipated features of the problem. 97

5.9 Gas bubble collapse test problem; plots on the left and right demonstrate the variations of pressure and non-dimensional volume, respectively, along the central axis of the simulated area 97
5.10 Gas bubble collapse test problem; plots depicting the density contours (uppermost), volume fraction(middle), and the magnitude of density gradient (bottom) for varying time frames of the gas bubble collapse experiment. . 98
5.11 The computational domain setup for the helium bubble shock-wave test problem is depicted in the top image, while the corresponding fine mesh is shown in the bottom image. 100
5.12 Shock-Helium bubble interaction; this figure shows the definition of interfaces and their position evolution during the interaction between a shock and a helium bubble. The CWENO5 scheme was used on both the finest 2D and 3D meshes, and the results are shown in the plot. The position evolution of the interfaces is consistent with the findings of previous studies by Terashima and Tryggvason [160] and Quirk and Karni [121]. 101
5.13 (i) Top shows experimental shadowgraphs of Haas and Sturtevant 1987 [58] experiment and and bottom shows computational result from UCNS3D at selected times of : (a) t= 37 ms, (b) t= 102 ms, (c) t= 427 ms, (d) t= 674 ms using a medium grid. [58] 101
5.14 Shock-Helium bubble interaction; the density colour iso-levels showing the evolution of the bubble as it interacts with shock-wave-at different instants using the finest mesh structure. Kelvin-Helmholtz instabilities emerge at the interface between the materials at a later time of the bubble's evolution. As a result, asymmetric solution profiles are formed due to the breakdown of these instabilities. 102
5.15 Shockwave-Helium bubble interaction; colour iso-levels plots of the volume fraction at $t = 983\mu s$ using different mesh resolutions. At $t = 983\mu s$, the higher grid resolutions capture more vortical structures because physical viscosity is absent, and the solution is less diffused. 102
5.16 Typical Underwater Explosion near U.S Navy Carrier [Source: US Navy, 2010] [82] 105
5.17 Bulk cavitation near a free surface [Source: Costanzo, 2010]] [30] 105
5.18 Computational domain setup for two-dimensional underwater explosion near a free surface. 112
5.19 Underwater explosion near a free surface; 2D unstructured finest mesh with triangular elements used for this test case. The density of mesh elements in specific areas of the domain is increased to better capture the physical phenomena occurring in those regions.The zoomed-in area on the right provides a more detailed view of the mesh's structure. 113
5.20 Underwater explosion near a free surface; Schileren visualization of density gradient using a CWENO4 scheme on a resolution of 1600 × 1600 cells (finest mesh) at $t = (0.2, 0.4, 0.8, 1.2)$ ms. 116
5.21 UNDEX near a free surface; Schileren visualization of pressure gradient using a CWENO4 scheme on the finest mesh at t = (0.2, 0.4, 0.8 and 1.2)ms. 117

5.22 UNDEX near a free surface; contours of volume fraction for underwater explosion near a free surface using a CWENO4 scheme on finest grid at t = (0.2, 0.4, 0.8 and 1.2)ms. 118
5.23 UNDEX near a free surface; cross-sectional plot of the density distribution along x = 0 119
5.24 UNDEX near a free surface; cross-sectional plot of pressure along x = 0 . 119
5.25 UNDEX near a free surface; cross-sectional plot of density and pressure along x = 0 at instants t = (0.4; 0.8)ms using Allaire et al. [4] and Kapila et al. [79] models. 120
5.26 UNDEX near a free surface; cross-sectional plot of density and pressure along x = 0 at instants t = 1.2 ms using different grid resolutions. 120
5.27 UNDEX near a free surface; density gradient contours at t = (0.2, 0.4, 0.8, 1.2)ms. Captured using CWENO4 schemes with different grids resolution. More inter-facial structures are sharper as the grid resolution increases. 121
5.28 Computational domain setup for a two-dimensional underwater explosion near a planar rigid wall. 122
5.29 UNDEX near a rigid wall; the pressure contours at different instants. Captured using CWENO3 scheme with medium grid resolution. At very low pressure, cavitation can be noticed at time t = 4 ms and 5.3 ms near the rigid walls 124
5.30 UNDEX near a rigid wall; plots of pressure history for the underwater explosion near a planar rigid wall at the center location of the upper wall obtained with CWENO4 schemes, and compared with other published results [59, 99, 189]. 125
5.31 Computational domain setup for the three-dimensional underwater explosion in a rigid cylinder. 126
5.32 Mesh strategy of the fluid domain for three-dimensional cylindrical underwater explosions zone 127
5.33 Corresponding mesh refinement for simulation. zone. 128
5.34 Underwater explosion in an enclosed cylindrical container; plots of pressure history (at the centre location of the left wall) for the underwater explosion in an enclosed cylindrical wall with CWENO4 schemes, and compared with other published results. [24, 147, 193] 129
5.35 UNDEX in an enclosed cylindrical container; pressure gradient contours for the 3D underwater explosion in an enclosed, rigid cylindrical wall. Captured using CWENO3. 130
5.36 Computational domain setup for the two-dimensional underwater explosion of two bubbles placed horizontally near a free surface. 131
5.37 Underwater explosion two bubbles placed horizontally near a free surface; plots of pressure history (at the centre location of the left wall) for the underwater explosion in an enclosed cylindrical wall with CWENO4 schemes, and compared with other published results. [24, 147, 193] . . . 132

5.38 UNDEX of two bubbles placed horizontally near a free surface; contour of volume fraction using a CWENO4 scheme on a medium mesh at t=(0.2, 0.4, 0.8 and 1.2)ms for inter-bubble lengths of (0.3, 0.5, 0.7 and 0.9) m respectively. 134
5.39 UNDEX of two bubbles placed horizontally near a free surface; contour of pressure gradient for the single bubble (Top) and the two-bubbles cases subsequently below for inter-bubble lengths of (0.3, 0.5, 0.7 and 0.9) m respectively using a CWENO4 scheme on a medium mesh at t=(0.4, 0.8 and 1.06)ms. The red-yellow areas are cavitation zones. 135
5.40 Computational domain setup for the three-dimensional underwater of two bubbles placed vertically in an enclosed region 136
5.41 Underwater explosion of two bubbles vertically placed in an enclosed region; plots of pressure history (at the centre location of the left wall) for the underwater explosion in an enclosed cylindrical wall with CWENO4 schemes for inter-bubble lengths of (15, 30, and 60) mm 137
5.42 Underwater explosion of two bubbles vertically placed in an enclosed region; volume fraction contours for the 3D underwater explosion in an enclosed for $H_b = 30$ mm, rigid cylindrical wall.Captured using CWENO4. The green-yellow areas shows the interface between water and explosive. The two bubbles eventually merge into a single larger bubble. 137
5.43 Underwater explosion of two bubbles vertically placed in an enclosed region; pressure gradient contours for the 3D underwater explosion in an enclosed rigid cylindrical wall with three different inter -bubble distances: H_b= 15 mm(Top), 30 mm(Middle), 60 mm(Bottom) for varying time frames t = (1.54, 6, 30, 60 and 90) µs. Captured using CWENO4. The white-red-yellow areas are cavitation zones, the red regions are indicative of potential high cavitation activity. 138

A.1 Contour plots of volume fraction, vorticity magnitude at the centre of the computational domain and isosurfaces of three levels of volume fraction (0.25, 0.5, 0.9) of the computed solution of the shockwave 3D helium bubble interaction test problem at different instants. 168
A.2 Contour plots for 3D underwater explosion in an enclosed cylinder. Displayed are the colour maps of density and pressure fields on the central cross-sections and the iso-surface of the volume fraction of 0.5 that represents the moving interface at different instants. 169

List of Tables

2.1 A summarised overview of the hierarchy of diffuse interface models, and pros and cons for their use in compressible multiphase flow 42
2.3 Summarised overview of the EoS commonly used for compressible multiphase flow using the Diffuse interface models. 50
2.4 Summarised overview of the methods used to minimize numerical smearing for compressible multiphase flow using the Diffuse interface models. U: Used; NYU: Not Yet Used (to the author's best knowledge). 59

5.1 Multi-species advection convergence study; The orders of convergence for the schemes are evaluated based on the volume fraction and normalized wall clock time at $t = 1.0$, along with the errors $e_{L\infty}$ and e_{L2}. All of the schemes achieve the desired accuracy, and the CWENO schemes only need about 60– 80 percent of the time of an equivalent WENO scheme. . 89
5.2 Normalised wallclock time for the 2D advection of material interface at t = 2.0 [2]. 91
5.3 The simulation results were used to calculate the time-averaged velocities of various flow characteristics in the shock-bubble interaction problem. These values were then compared to the experimental findings of Haas and Sturtevant [58] and the computational results of Coralic and Colonius [29]. The velocities were averaged over time intervals of $[10, 52]\mu s$ for the upstream interface, $[140, 240]\mu s$ for the jet, and $[140, 240]\mu s$ for the downstream interface. It was observed that all of the predicted values were within the range of experimental variations and were in good agreement with the computational results of Coralic and Colonius [29]. 100
5.4 Summarised overview of the test cases, their purposes for this research and the key findings. 139
5.5 Summarised overview of the test cases involving cavitation, their use and key findings from this research 140

Nomenclature

ADIS Anti-Diffusion Interface Sharpening

BN Baer–Nunziato

BVD Boundary Variation Diminishing

CFD Computational Fluid Dynamics

CFL Courant Friedrichs Levy (number)

CWENO Central Weighted Essentially Non-Oscillatory scheme

DDT Dichlorodiphenyltrichloroethane

DG Discontinuous Galerkin

DIM Diffuse Interface Models

EoS Equation of State

FD Finite Difference

FV Finite Volume

HLL Harten, Lax, Van-Leer

HLLC Harten-Lax-van Leer-Contact Riemann solver

HPC High-performance Computing

IVP Initial Value Problem

MFM Multi-fluid Models

MOOD Multi-dimensional Optimal Order Detection

MUSCL Monotone Upstream-Centred Scheme for Conservation Laws

PDE Partial Differential Equation

PFM Phase Field Models

RHS Right-hand Side

RK Runge-Kutta

RP Riemann Problem

SA Saurel-Abgrall

SG Stiffened Gas (EoS)

SHTC Symmetric Hyperbolic and Thermodynamically Compatible

SIM Sharp Interface Models

SPH Smoothed-particle Hydrodynamics

SSP Strong Stability Preserving

THINC Tangent of Hyperbola for Interface Capturing

TV Total Variation

TVD Total Variation Diminishing

UCNS3D Unstructured Compressible Navier Stokes 3D

UNDEX Underwater Explosion

VoF Volume of Fluid

WENO Weighted Essentially Non-Oscillatory scheme

Symbol	Definition	Units
	Roman Symbols	
c	Speed of sound	m/s
∂	Partial differential operator	-
e	Specific internal energy	J/kg
E	Total energy	N/J^2
$\mathbf{F}$	Flux tensor	-
g	Gravity acceleration vectors	m/s^2
M	Mach number	-
n	Normal vector of cell face	-
∇	Gradient operator	$1/m$
$\nabla\cdot$	Divergence operator	$1/m$
$\mathbf{Q}$	Conserved variable vector	-
S	Entropy	-
t	Time	s
u	Velocity component in the x-axis	m/s
$\mathbf{u}$	Velocity field	m/s
v	Velocity component in the y-axis	m/s
w	Velocity component in the z-axis	m/s
	Greek Symbols	
α	Volume fraction	-
ε	Internal energy	N/J^2
γ	Heat capacity ratio	-
λ	Eigenvalues	-
ν	Kinematic viscosity	m/s^2
π_∞	Stiffened gas pressure	Pa

ρ	Density	kg/m^3

Supercripts

$'$	Reference status	-
lim	Limit	-
max	Maximum	-
min	Minimum	-
n	Temporal index	-
T	Transpose	-

Subcripts

0	Initial state	-
1	Fluid 1	-
2	Fluid 2	-
cav	Cavitation	-
(i)	Numerical index in the direction of x	-
I	Interface	-
(j)	Numerical index in the direction of y	-
(k)	Numerical index in the direction of z	-
k	Kinetic energy	-
L	Left state	-
m	Degree of Freedom	-
opt	Optimal	-
ref	Reference	-
R	Right state	-
sat	Saturation	-
T	Total energy	-

Accents

Ast	x^*	-
Bar	$\bar{x}$	-
Dot	$\dot{x}$	-
DDot	$\ddot{x}$	-
Vector	$\vec{x}$	-
Hat	$\hat{x}$	-
Overline	$\overline{x}$	-
Prime	$\acute{x}$	-
Tilde	$\tilde{x}$	-
Underline	$\underline{x}$	-
Vector	$\vec{x}$	-

Acknowledgements

My utmost gratitude goes to the Petroleum Technology Development Fund (PTDF) for funding my research and tuition throughout my PhD. This funding allowed me to carry out research that interested me without ambiguity.

I express my sincere gratitude to the late Prof. Emeritus A. I. Belousov, whose numerous discussions and our beautiful father-to-son relationship sparked my interest in pursuing a PhD after my master's programme under his tutelage in Russia. That phase in my life is the pillar and foundation of my research interest.

This work would not have been possible without the immense and painstaking contribution of my supervisor, Dr. Panagiotis Tsoutsanis, for his outstanding support, insightful comments, explicit recommendations, and guidance during my research. I couldn't have asked for a better supervisor.

I am especially indebted to Professor Christopher Odetunde, the current Vice Chancellor of Saint Augustine's University, Nigeria, who has been helpful in providing mentorship and has been supportive of my professional ambitions and personal development.

To my parents, Mr. and Mrs. H.B. Adebayo, and my siblings, I am grateful to have your support to push me to this point, regardless of how far we are from each other.

Above all, I would like to appreciate my newlywed wife, Bola, for her immeasurable love, support, and patience with me during my various mood swings and busy schedules, which are typical with such tasking research.

To God almighty, I thank you for the journey so far.

"Whatever is fluid, soft, and yielding will overcome whatever is rigid and hard. What is soft is strong."

- Laozi

Chapter 1

Introduction

A fluid consisting of more than one material phase or component, is called a **multiphase** or **multi-component**. Throughout this thesis, these terms will be used interchangeably and treated as synonym. Each will be described to avoid ambiguity. Phases are the states of matter, e.g., gas/vapour, liquid, or solid. The term "component" describes the chemical composition of substances in a phase. A flow in the same phase can have two or more components or species. An example is a two-phase flow of water (liquid) and steam (gas). They both have the same chemical constituent, (H_2O). This is an example of a multiphase flow with a single-component. Multiphase flow exists in different phases: two-phase and three-phase. The interest in this research is the two-phase flow. Such flows can be found in many man-made and natural phenomena; hot coffee flowing through a coffee machine, the blood flowing in bloodstream, suspended sediment transport caused by flowing water in lakes, rivers, oceans, and seas as well as the flow of viscous magma during volcanic eruptions.

There is a distinctive interface that separates the phases in every multiphase or multi-components fluid. Following Andrianov's definition [7], fluid problems can be categorised based on their material and interface properties. With this in mind, two-phase flows can be classified by their material properties into three types: **Liquid-solid flows** such as slurry flows, where solid particles are suspended in a liquid, and sediment transport, where

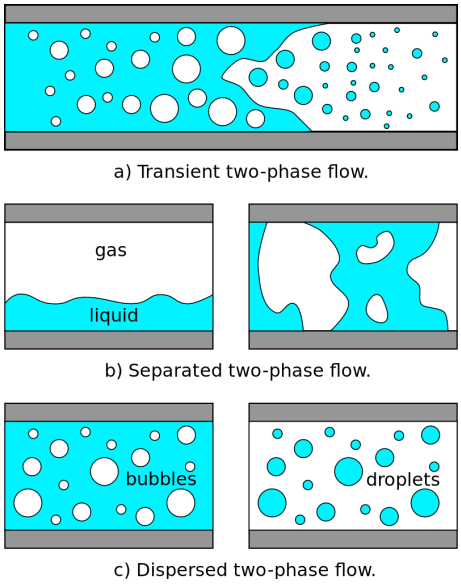

Figure 1.1: Two-phase flows (Adapted from [154]).

solid particles are transported by a flowing liquid.**Gas-liquid flows**, which include bubbly flows, where small gas bubbles are dispersed in a liquid, and slug flows, where elongated gas bubbles or slugs move through a liquid. **Gas-solid flows** which include fluidized beds, where solid particles are suspended and agitated by a gas flow, and pneumatic transport, where solid particles are transported by a gas flow. Based on the fluid's interfacial characteristics, they can exist in the following flow-regimes: **separated, transitional, and dispersed** flows (see Fig. 1.1). Separated flow involves the flow of the material in different continuous streams, separated by a distinct interface. The fluid phases flow as separate layers, while in dispersed flow, the materials flow in one continuous phase which allows intermixing of the participating fluids. This work is only on separated flow.

Although most multiphase flows are mostly treated as incompressible flows, compressibility in a flow can be induced by high pressure in the phases or a high flow Mach number. Single-phase compressible flows are ubiquitous in CFD and primarily concerned with two flow-regimes-laminar and turbulent. Single-phase flows are also primarily characterised by a discontinuous wave in the form of shock-waves and solved using the Euler or Navier-Stokes equations. Compressible multiphase, multi-component, or multi-material flows, on the other hand, can exist in the various flow-regimes mentioned earlier

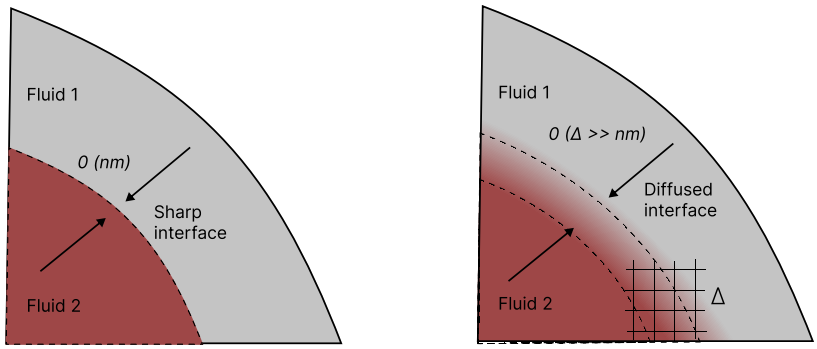

Figure 1.2: The interface of compressible multiphase and multi-component flows

and are characterised by not just shock-waves but a new form of discontinuity in the form of contact waves at the interface. The wide application of compressible multiphase flow in science and engineering has led to much work devoted to solving and understanding the models of the interfacial interactions between the fluids. Compressible multiphase and multi-component flows are helpful in explosives (detonation of heterogeneous materials), combustion (fuel injection in supersonic and hypersonic ramjet engines), desa-lination in a nuclear reactor, and underwater motion of high-speed projectiles. The interface of compressible multiphase and multi-component flows frequently has a different thermodynamic property than the two interacting fluids and can obey different equations of state (EoS). Numerical modelling of the material interface of compressible multiphase flows requires the Euler or Navier-Stokes equation for each fluid coupled with extra equation(s) for the interface. The complexity of the physics involved in the phase change of the mixture, the high gradients of flow variables, the choice of numerical discretization to capture these phenomena, and getting experimental results for validation are several factors that make the numerical modelling of such flows challenging. When numerically modelling compressible multiphase flow, two parameters are of interest and importance. How that interface is being treated and the location or position of the material interface between the two fluids. The location of the constantly changing interface must first be identified and

then treated either explicitly or as a diffuse zone. The traditional approach to treating the interface between two fluids is to consider the interface to be infinitely sharp, i.e., with a thickness of zero. The material interface in the flow between the fluids is treated as an infinitely thin free boundary. The physical internal structure of such an interface is not considered or resolved. This assumption is reasonable and straightforward in many cases, owing to the fact that the interface thickness of such a flow is infinitesimal, on the order of a few Angstroms ($1\mathring{A} = 10^{-10}m$). These methods described above in which the interface is advected and regarded as a sharp discontinuity are often regarded as the "sharp interface methods" SIM (Fig. 1.2).

Locating the position of the interface has two common approaches. The interface can be tracked using a Langragian moving mesh or a fixed Eulerian grid. The Lagrangian models deform with each fluid's particle and interface motion. They are commonly used for dispersed flow. The physical properties such as mass, velocity, temperature, and position of the single particles are tracked. This can be cumbersome, especially for a complex geometry and three-dimensional cases. This is because tracking the interface often leads to large deformations due to re-meshing. To circumvent this problem, interface tracking methods used for advecting the interface are the Volume of Fluid VoF, front-tracking, level set methods, and the ghost fluid method. Coupled with the momentum, energy, and volume species equations for each phase, the interface, treated as a free boundary, is supplemented with boundary conditions and equations. Many works have been done to improve on their significant drawbacks: low-speed flows, low density-viscosity ratios, and mass-conservation errors [167, 118, 94, 185]. In a wide range of situations, the interface is treated as a free boundary while its motion is tracked is sufficient and reasonable. These methods of tracking the interface, while the interface is referred to as a sharp feature, are regarded, in general terms, as interface tracking methods. In some literature, SIM is used interchangeably with the term "interface tracking method". In flows involving changes in the topology of the interface, the structural composition of the interface plays a critical role. In situations where the interface is involved, the physical

mechanisms that act on the interface may be of a scale similar to the thickness of the interface that separates the two fluids in contact. This can lead to a deformation of the interface and changes in the topology, such as the merging of bubbles or the breakup of liquid droplets, underwater explosions, etc.

Assuming a zero thickness for the interface can lead to errors in the calculation of the interfacial forces and in the mass transfer rates. In such cases, the interface may have a finite thickness due to interfacial tension effects or thermal diffusion, and neglecting this thickness can be erroneous.

To accurately capture the internal structure of the interface, another approach for treating the interface is to capture the interface as diffuse zones. This method provides a smooth representation of the interface, taking into account the interfacial thickness and the associated physical mechanisms. These methods are referred to as the **"Diffuse Interface Models" DIM**. In diffuse interface models, the two fluids are assumed to have different densities, viscosities, and other physical properties, but are allowed to mix across the interface zone. They are built upon the averaging procedures of the local conservation and thermodynamic laws. The average values of volume fraction and thermodynamic quantities like momentum, energy, and pressure of the fluids are determined by solving a set of unconditionally hyperbolic equations on a fixed Eulerian grid. The solution of the conserved quantities is then evolved across all computational cells via numerical discretization, resulting in numerical or artificial diffusion across multiple grids without the need to explicitly track or reconstruct them as in the SIM or interface tracking method. In order to comprehend the dynamics of phase transitions and the behavior of materials at interfaces, it is crucial to compute internal energies and temperatures at the interfaces in an accurate and efficient manner. The Diffuse Interface Model (DIM) has gained popularity in recent years due to advancements in computational power, which have allowed for more efficient and accurate simulations of multiphase, multicomponent and multispecies systems.

That being said, the focus of this research is on the diffused interface models based on

the Baer-Nunziato [17] seven-equations model. The Baer-Nunziato model consists of two mass conservation equations, two momentum equations, two energy equations, and one extra equation that describes the topology of the flow, such as advection or convection.

The original Baer-Nunziato model has a significant amount of waves, which can make it computationally expensive and difficult to use. It may also be sensitive to numerical relaxation techniques. Simplified versions of the Baer-Nunziato model have been created to address these problems, using equilibrium assumptions to lessen the number of waves and improve the model's computational efficiency.

The Baer-Nunziato equations are simplified by assuming thermodynamic equilibrium between the two phases, which allows for the elimination of some of the non-equilibrium terms in the equations. This reduces the number of waves in the system and makes the model more stable and easier to solve numerically. The equilibrium assumptions used in these models may include assumptions about temperature and pressure equilibrium, as well as assumptions about the mass transfer rates between the two phases.

Several simplified versions of the full Baer-Nunziato model have been developed that are widely used in practical engineering applications. Some of the most commonly used simplified models include the Kapila et al. model [79], the Allaire et al. model [4], the Saurel et al. model [133], the Murrone et al. model [102], and the Abgrall et al. model [131].

The "ideal" mathematical model for solving a compressible multiphase system is strictly hyperbolic, fully conservative, and follows thermodynamic laws [43]. However, it is often challenging to develop a model that meets all three criteria simultaneously, and trade-offs may need to be made between accuracy and computational efficiency.

In recent years, much work has been done to improve existing models and develop new models that better satisfy the "ideal" mathematical conditions. This includes the development of new numerical methods and algorithms that are better suited to solve the complex equations governing multiphase flows. Additionally, efforts have been made to incorporate more accurate thermodynamic models and equations of state into the models

to improve their accuracy.

A good spatial resolution is essential for accurately resolving the high gradients in the form of shock and contact discontinuities at the interface without excessive diffusion or oscillation. In comparison to lower-order techniques, high-order schemes present a relative advantage in enhancing the spatial resolution at the interface regions for multiphase compressible flows. Some commonly used high-order methods for diffuse interface models include: Discontinuous Galerkin (DG) method [64], Finite difference and finite volume weighted essentially non-oscillatory (WENO) schemes [73, 182, 29], Monotone Upstream-centred Scheme for Conservation Law (MUSCL) with the use of limiters and Multi-dimensional Optimal Order Detection (MOOD).

The present research uses the CWENO (Central Weighted Essentially Non-Oscillatory) schemes, which are a WENO variant. These schemes are implemented by Tsoutsanis and Dumbser [177] on unstructured meshes. This choice is motivated by the observed robustness and significantly enhanced computational efficiency of these methods compared to the original WENO schemes for unstructured meshes. Furthermore, these CWENO schemes have been effectively employed in previous studies utilizing the full seven equation Baer-Nunziato model by Dumbser et al. [40]. The improved robustness and efficiency are provided in the way the scheme computes the numerical fluxes at the cell interfaces. WENO uses a weighted combination of different stencil approximations, where the weights are chosen to minimize the amount of numerical oscillations in the solution. On the other hand, CWENO uses a weighted central stencil approximation, where the weights are computed based on the smoothness of the solution in the stencil. For more details on the CWENO, the reader is referred to [42, 177, 39, 90]. All the schemes and models used for this research are implemented in the open source community UCNS3D solver [14], which is written in Fortran 90 and parallelized using Message Passing Interface (MPI) to achieve high computational efficiency.

1.1 Aims and Objectives

Using diffuse interface models (DIM), this research aims to implement high-fidelity finite-volume numerical methods on unstructured meshes to accurately and efficiently solve multiphase, multi-component, and multi-species problems encountered in the energy, aerospace, and automotive sectors. The objectives include implementing the schemes and governing equations into the existing open-source computational framework (UCNS3D) [14], applying them to test problems involving compressible multiphase or multi-species or multi-component flows, comparing them with existing methods, and contributing to the field by publishing research articles and presenting findings at conferences. Overall, this research advances the knowledge and understanding of compressible multiphase flow simulation using unstructured meshes for diffuse interface models, making a significant contribution to the field. In order to achieve the main objective of this thesis, this research passes through a number of specific tasks, which are detailed below:

- Identification and critical evaluation of potential multiphase and multispecies flow equations in the framework of diffuse-interface methods through a detailed literature review.
- Application of a numerical framework for the multiphase flow based scheme on the in-house code to include parameters for solving compressible multiphase flow for any hyperbolic compressible system of multicomponent equations.
- Evaluation of the performance of various diffuse interface models and high-order numerical schemes for compressible multiphase flows in terms of accuracy, robustness, and computational efficiency.
- Investigating the impact of various model parameters and numerical settings on the accuracy and convergence of the simulations from compressible multiphase flow.
- Validation of the developed numerical framework against experimental and numerical data available in the literature for various benchmark 2D and 3D test problems.

- Exploring the potential applications of the developed numerical framework for solving challenging multiphase flow problems such as cavitation in engineering and science.

- Demonstrate the capabilities of the code by analysing the performance of the code computational clusters when tackling industrial-level problem.

1.2 Contributions to the Scientific Knowledge

In this thesis, a computationally efficient high-resolution numerical method designed to accurately capture shocks and interfaces within a finite-volume framework on unstructured grids is introduced. The CWENO high-order schemes is introduced to enhance the accuracy and robustness in resolving material interfaces in the context of multi-component or multiphase flows, especially in flow cases involving strong gradients and material discontinuities. This is achieved by ensuring oscillation-free solutions and minimizing numerical diffusion.

The research employs the diffuse interface framework implemented in the open-source unstructured compressible flow solver, UCNS3D. The UCNS3D serves as the computational framework for testing and demonstrating the effectiveness of the proposed CWENO high-order schemes. Throughout the course of this study, the UCNS3D code is not only utilized but also extended with additional multiphase features, reflecting a continual commitment to improving and refining the codebase.

The numerical results obtained from this study are compared rigorously with those from other high-order methods and experimental data available in the existing literature. The core findings of the results underline the superior capabilities of the CWENO finite-volume interface capturing schemes in accurately representing and simulating complex multiphase phenomena within compressible flows. Notably, the CWENO method exhibits reduced dissipative effects and effectively mitigates the occurrence of spurious oscillations at material boundaries. Furthermore, it offers a high-resolution and sharp depiction of

moving material interfaces at a lower computational cost, achieving minimal artificial smearing compared to other existing high-order schemes.

With the results obtained from this research, the thesis advances the understanding of numerical techniques for simulating multi-component or multiphase compressible flows. It not only introduces innovative computational method of using the CWENO finite-volume interface capturing schemes but also substantiates the capabilities through a rigorous evaluation against both established numerical approaches and experimental data. The contributions of this research have implications for a wide range of applications in fluid dynamics, particularly in cases where accurate and robust representation of interfaces is crucial.

1.2.1 Publications

The findings and research presented in this thesis have been published or submitted in the peer-reviewed articles listed below:

- P. Tsoutsanis, E. M. Adebayo, A. C. Merino, A. P. Arjona, and M. Skote, CWENO finite-volume interface capturing schemes for multi-component flows using unstructured meshes, *Journal of Scientific Computing* (2022) [172].

- E. M. Adebayo, K. Jenkins, P. Tsoutsanis, Application of CWENO Finite-Volume Interface Capturing Schemes for Modeling Cavitation Induced by an Underwater Explosion, *Physics of Fluids (2023)* (Submitted)

- Published a conference paper for the European Community on Computational Methods in Applied Sciences ECCOMAS CONGRESS 2022 in Oslo, Norway as "E. Adebayo, P. Tsoutsanis and K. Jenkins, Application of interface capturing schemes on multiphase or multicomponent compressible flow of underwater explosion, *Eccomas 2022 Computational Fluid Dynamics (2022)*"

1.3 Thesis Overview

This thesis is structured as follows: **Chapter 1** introduces multiphase flow in general with the definition and description of terms relevant to our research. The research remit is then narrowed then narrowed down to compressible multiphase and multi-component flows, discussing the models that apply to such flows, their advantages and shortcomings. The chapter continues with the diffuse interface model definition, and the set of possible hyperbolic equations used in this model category.

In **Chapter 2**, a detailed and up-to-date review of existing literature and current works that have been done so far using diffuse interface models in the numerical modelling of compressible multiphase flow was carried out. In this in-depth review, the mathematical models currently in use for solving compressible multiphase flows were identified; the limitations and strengths were discussed in detail, and the set of equations to be used for the research was recalled. The various equation of states EOS often used to provide closure to this set of hyperbolic equations are also discussed.

The finite volume (FV) numerical discretization of the five-equation set of diffuse interface models is the focus of **Chapter 3**. As the chosen fluxes and temporal discretization are described, the CWENO scheme reconstruction process is thoroughly explained. The Riemann problem for the five-equation mechanical equilibrium model developed by Kapila et al. [79] and by Allaire et al. [4] used in this study is also detailed.

Chapter 4 of the dissertation evaluates the robustness of central-weighted essentially non-oscillatory (CWENO) reconstruction schemes with the use of five-equations diffuse interface models developed by Allaire et al. [4] and Kapila et al. [79] in the finite volume framework. The assessment is conducted through subjecting the methods to a series of demanding benchmark cases and test problems, which encompass various gas-liquid combinations. The outcomes are compared with analytical solutions, computational results, and previously published experimental data.

In the concluding chapter, we summarize the study's conclusions, pinpoint areas needing further research, and offer recommendations for future studies.

Chapter 2

Literature Review

A thorough review of the Diffuse Interface Models (DIM) is carried out from a historical perspective to highlight the development of this class of models. Applications and computations using these models for compressible multiphase flow are discussed in each case. The drawbacks associated with each diffuse-interface model are then discussed. Other authors who have done extensive work in this category are acknowledged [87, 136, 131, 101]. The idea of an interface separating a multiphase flow has existed since at least two centuries ago. Young, Gauss, and Laplace proposed the initial concept of an interface having zero thickness in the early 18th century [87]. An interface was assumed to be a free boundary with surface tension. Physical parameters such as capillarity sustained across the interface were represented by boundary conditions and described by the Young-Laplace equation. Other physical properties (density, pressure, and viscosity) at the interface were assumed to be discontinuous. The idea evolved in the late 18th century, and predicting interface thickness was of interest. The approach of taking the interface as a thin layer with a non-zero thickness (i.e. a diffuse zone) surface can be traced to the works of Clausius, Poisson (1831) [141], Maxwell (1876) and Gibbs (1876) [53] [6]. In Gibbs's paper[53], "The equilibrium of heterogeneous substances", he examined the thermodynamic theory of capillarity at the interface. From this fundamental theory, Rayleigh (1892) [124] and Van der Waals (1893) [130] developed gradient theories for

predicting the thickness of an interface. Van der Waals utilized his equation of state (EoS) for thermodynamic consistency to derive gradients at the interface, using the density of the flow as the phase parameter. This method was used extensively in the statistical mechanics of non-uniform states [107]. Rayleigh and Van der Waal were unable to account for the properties and changes in interfacial energy caused by the introduction of non-equilibrium material [22], and thus could not estimate the thickness of the interface precisely. Ono (1951) and Hillert (1956) [69] were notably the first to calculate the equilibrium thickness describing the interfacial phenomena of multiphase flows. Cahn and Hilliard (1959) [22] extended the Van der Waals idea from single-component fluid to binary fluid or alloys undergoing spinodal decomposition. This development can be regarded as the beginning of diffuse interface methods (DIM), even though the applications were solely for incompressible flow.

Over the last two decades, computational power has increased tremendously. Due to this technological advancement, more attention has been focused on the diffuse model methods, and further work developed, especially with the compressible flow in focus. From the above historical perspective, all DIMs, in general, treat the interface as a volumetric region or thin layer. The DIM can be classed into two broad categories. The Phase Field Models (PFM) and the Multi-Fluid Models (MFM). The PFM models are formulated based on the Cahn–Hilliard (C.H.) equation [22], which describes the phase separation process. Notable authors such as Kawasaki (1972) [37], Hohenberg and Halperin (1977) [66], Siggia (1979) [149] extended this into two-phase hydrodynamics. The PFM considers the interface as a transition layer, and these models can handle complex interfaces with varying topology, such as multiple phases with arbitrary shapes. They referred to these methods as the “model-H” or “H-model”. This group of models was later renamed the diffuse interface method DIM [87]. They are beneficial for immiscible liquids geometrically constrained to a small scale (microfluidics) and turbulent two-phase flows, and can also capture phenomena such as coalescence, break-up, and phase separation. Their key features are interface motion and thickness estimation. Recent works published on the

DIM based on the C.H. equation can be found in [77].

The second group is the multi-fluid model (MFM). This group treats the interface as a diffuse surface with artificial mixing. The two states are allowed to mix. The individual phase has its own distinct fluid and governing equations. The interface is represented as a transition region between the fluids, and its thickness is usually taken as a small but finite value. MFM is generally less computationally expensive than PFM, but may not be able to capture complex interface topologies as accurately. MFM is more suitable for flows with large density ratios between the phases which is our focus in this research. Most of these models in the category of MFM have their fundamentals from the Volume of Fluid (VoF) methods developed by Hirts and Nicols [65]. The Baer–Nunziato (B-N) model is considered one of the complete models in the MFM category. The Baer–Nunziato (B-N), which was formulated in 1986 to solve Dichlorodiphenyltrichloroethane (DDT) detonation problems between solids is built upon averaging (volume averaging [186, 19, 36] and time averaging-Ishii (1975) [70]) procedures of the local conservation laws. The phase of an individual fluid can be identified and characterised by a separate equation of state (EoS). Each phase has its own equations and thermodynamic properties, i.e., density, pressure, and internal energy. The B-N set of models is regarded as non-equilibrium because there is a total disequilibrium of velocity and pressure between the two phases. The challenges of this model are due to its non-conservative nature. It cannot be expressed in a conservative or a divergent form, although many recent researchers have found a way to go around this through numerical relaxation procedures. The main challenges of DIM multiphase flow numerical modelling and formulations lie in the development of a mathematical model that is **hyperbolic (symmetric hyperbolicity)**, **fully conservative** and **consistent with the thermodynamic laws**.

The reduced or sub-model of the B-N full seven equations is derived through asymptotic expansions where physical properties such as pressure, velocity, and temperature are assumed to be in equilibrium between phases. To the author's best knowledge, Saurel and Abgrall 1999 [133] were the pioneers of the sub-models of the full B-N and first

extended this approach to compressible multiphase flow. Several other models have emerged, and these sub-models can be classified based on equilibrium assumptions or relaxation procedures introduced to the non-equilibrium full B-N equations. Since each k-phase has different pressures p_k, temperatures T_k, velocities v_k and chemical potentials μ_k, many authors have employed various relaxation procedures to bring the mixture into a phase equilibrium. Among them are relaxations towards a **mechanical equilibrium** (where velocity and pressure are driven towards equilibrium at the interface), **thermal equilibrium** (no net transfer of heat between the phases), **velocity equilibrium** and **pressure equilibrium** or a combination of two numerical relaxations (for example, mechanical and thermal equilibrium) (Fig. 2.1). Each of these numerical relaxations is carried out to suit the specific compressible multiphase flow that is being modelled, the researcher's expectations, and the computational resources available for the numerical simulation. The number of equations in the existing reduced models ranges from six to four, depending on the relaxation procedures. These sub-models have also been successfully applied to compressible multiphase flow problems. For specific flow problems, additional phenomena such as surface tension, heat conduction, viscous stresses, and gravity effects can be incorporated into the sub-models.

The mechanical equilibrium models proposed by Allaire and Massoni (2002) [4], Guillard and Murrone (2005) [102], and Kapila (2009) [79] have gained considerable recognition. Also among these is the Saurel's six-equation model (1999) that takes into account velocity equilibrium. Furthermore, a newer seven-equation model has been introduced by Romenski (2019). However, the focus in this study lies on the mechanical equilibrium models proposed by Kapila et al. [79] and Allaire et al. [4].

They offer the following advantages :

- Simpler to implement.
- Able to treat interfaces between immiscible fluids (liquid-gas).
- Able to treat mixtures evolving in mechanical equilibrium.

- Able to treat complicated flows correctly, such as those involving cavitations.
- Simplicity of incorporating extra physics such as surface tension, mass-transfer, viscous effects, phase change effects, and cavitation.

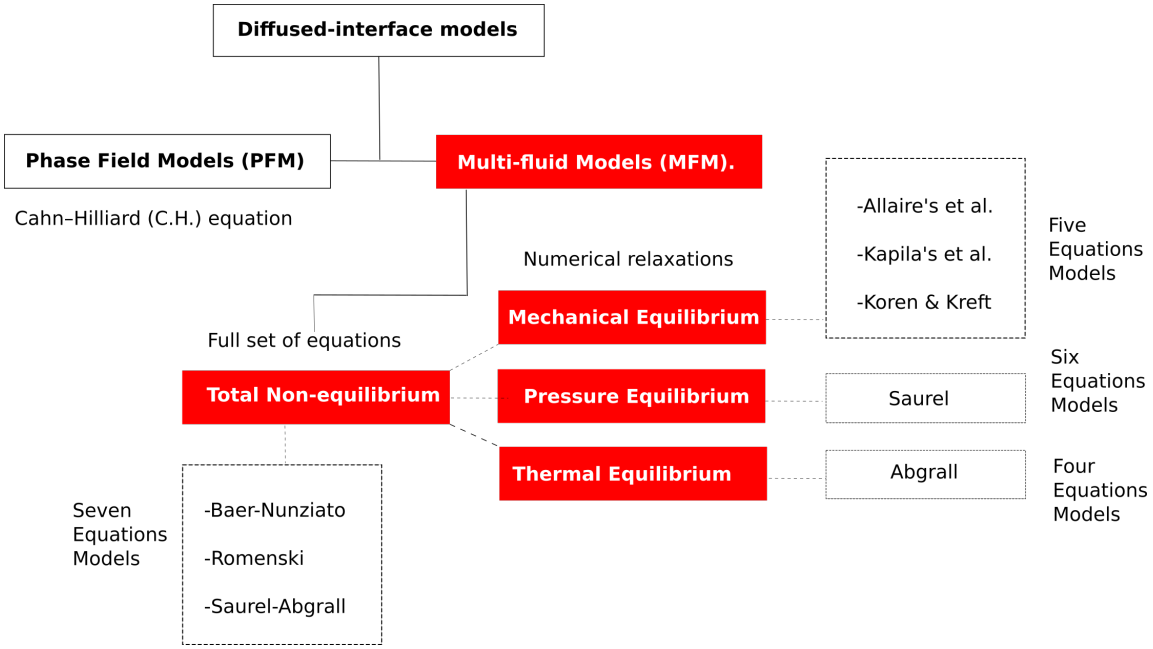

Figure 2.1: Diffused-interface models.

The next section, we will detail the total disequilibrium models and give a model hierarchy by categorising the sub-models based on the numerical relaxation or procedure used.

2.1 Non-equilibrium or Total Disequilibrium Models

The most general forms of the diffuse interface model for multifluids are the total non-equilibrium models. These models are mostly seven (7) sets of hyperbolic partial differential equations (PDE), in which each fluid phase has its own pressure, temperature, velocity, and other physical parameters. They are regarded as non-equilibrium due to the total disequilibrium of physical variables (pressure, temperature, velocity, temperature, and chemical compositions) assumed between the two different phases. The seven equations consist of two mass equations, two energy equations, two momentum equations, and one equation for each phase to describe the volume fraction or topology of the interface. The models in this category are **Baer-Nunziato** seven-equations, **Saurel-Abgrall** seven-equations, and **Romenski** seven-equations (Fig. 2.2). This thesis uses the abbreviation B-N for the Baer-Nunziato model. Although complete and capable of handling a wide range of multiphase flows and trivial cases, these total disequilibrium models are usually computationally expensive and too complicated to solve numerically, as they often contain source terms that are not conservative. These source terms are usually differential or algebraic expressions for the interfacial forces of the fluid. Using the ensemble averaging procedures of Drew and Passmann [38], Saurel-Abgrall developed a seven-equations based on the full B-N seven equations by neglecting the dissipating terms. Romenski proposed another set of equations to circumvent the non-conservative nature of B-N model types, his approach resulted in another seven conservative equations that are hyperbolic (non-symmetric) and can be expressed in divergent forms. The seven equations of Saurel-Abgrall and B-N are hyperbolic but non-symmetric. The three non-equilibrium models mentioned above will be discussed in detail below.

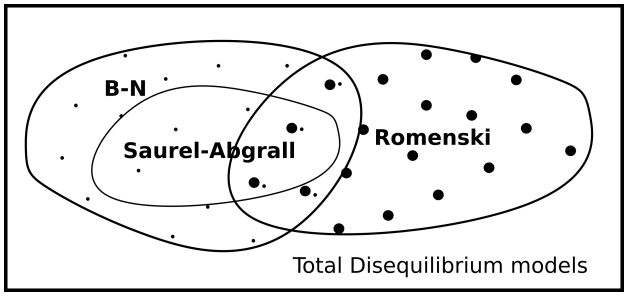

Figure 2.2: The hierarchy of the seven-equation total disequilibrium models. The Romenski model has similarities with the B-N-type model (Saurel-Abgrall) for isentropic cases.

2.1.1 Baer-Nunziato non-equilibrium model

Baer-Nunziato's (B-N) model, as stated previously, is a high fidelity model and the basis of most models in the MFM category of the diffuse-interface methods. The hyperbolic set of seven equations were developed by Baer and Nunziato in 1986 to solve the deflagration to detonation transition in explosive materials (DDT) and is now widely applied to other areas of compressible multiphase flows. This is one of the most widely used and general full non-equilibrium multiphase flow models for this type of DIM. The equations include the conservation of mass, momentum, and energy for each phase, as well as equations that describe the interfacial area and the phase change process. The conservation equations for each phase include terms that account for the interfacial momentum and energy transfer between the phases on an Eulerian grid system. The challenges of this model are its non-conservative nature, as mentioned earlier, in its original form, it cannot be expressed in a conservative or a divergent form. The Baer-Nunziato model has seven equations; two

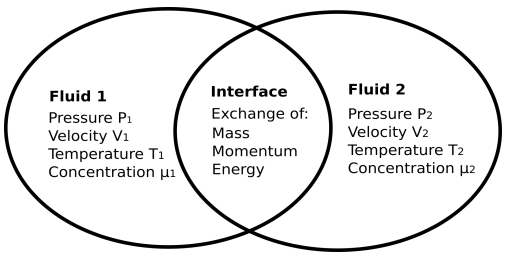

Figure 2.3: Physical parameters of each fluid in a multiphase/multicomponent flow

mass conservation 2.2, two momentum equations (2.3), two energy equation (2.4), and one extra equation (2.1) describing the volume fraction. Each phase can be identified

and characterised by separate thermodynamic properties: pressure, velocity, temperature, and, chemical potential (Fig. 2.3). A revised version of the Baer-Nundiato seven-equation model is provided by Lund et al. [97, 49] with mass exchange and heat transfer. The revised version constitutes the possible relaxation processes expressed explicitly as source terms on the right-hand side (RHS) of the equation.

- Volume advection:

$$\frac{\partial \alpha_1}{\partial t} + \vec{u}_I \cdot \nabla \alpha_1 = \Psi, \tag{2.1}$$

- Mass conservation:

$$\begin{aligned} \frac{\partial}{\partial t}(\rho_1 \alpha_1) + \nabla \cdot (\alpha_1 \rho_1 \vec{u}_1) &= \Phi, \\ \frac{\partial}{\partial t}(\rho_2 \alpha_2) + \nabla \cdot (\alpha_2 \rho_1 \vec{u}_2) &= -\Phi, \end{aligned} \tag{2.2}$$

- Momentum conservation:

$$\begin{aligned} \frac{\partial}{\partial t}(\alpha_1 \rho_1 u_1) + \nabla \cdot (\alpha_1 (\rho_1 \vec{u}_1 + p_1)) - p_I \cdot \nabla \alpha_1 &= \Lambda, \\ \frac{\partial}{\partial t}(\alpha_2 \rho_2 u_2) + \nabla \cdot (\alpha_2 (\rho_2 \vec{u}_2 + p_2)) - p_I \cdot \nabla \alpha_1 &= -\Lambda, \end{aligned} \tag{2.3}$$

- Energy balance:

$$\begin{aligned} \frac{\partial}{\partial t}(\alpha_1 \rho_1 E_1) + \nabla \cdot (\alpha_1 \vec{u}_1 (\rho_1 E_1 + p_1)) - p_I u_I \cdot \nabla \alpha_1 &= \Gamma, \\ \frac{\partial}{\partial t}(\alpha_2 \rho_2 E_2) + \nabla \cdot (\alpha_2 \vec{u}_2 (\rho_2 E_2 + p_2)) + p_I u_I \cdot \nabla \alpha_1 &= -\Gamma, \end{aligned} \tag{2.4}$$

Where the subscript 1 and 2 are the phases i and α_i, ρ_i, $\vec{u}_i$, p_i , E represent the volume fraction, density, the velocity vector, pressure, total energy per unit mass of each phase and must satisfy the saturation constraint $\alpha_1 + \alpha_2 = 1$, p_I and u_I are the interfacial pressure and velocity which is expressed as:

$$p_I = \alpha_1 p_1 + \alpha_2 p_2,$$

$$u_I = \frac{\alpha_1\rho_1 u_1 + \alpha_2\rho_2 u_2}{\alpha_1\rho_1 + \alpha_2\rho_2}.$$

The R.H.S are represented by source terms $\Psi, \Phi, \Lambda, \Gamma$ which are terms for volume transfer, momentum transfer, mass transfer and energy transfer. They are dependent terms on the relaxation coefficients $\mathscr{J}, \mathscr{K}, \mathscr{L}, \mathscr{M}$ (See 2.5). The relaxation coefficients are functions of pressures, chemical potential, velocities and temperatures of the two-phase flow. They control the rate at which equilibrium is reached and are expressed below as:

$$\begin{aligned}
\Psi &= \mathscr{J}(p_1 - p_2) \\
\Phi &= \mathscr{K}(\mu_1 - \mu_2) \\
\Lambda &= \mathscr{K}(\mu_1 - \mu_2) + \mathscr{L}(u_1 - u_2) \\
\Gamma &= (\mu + \frac{1}{2}v^2)\mathscr{K}(\mu_1 - \mu_2) + p\,\mathscr{J}(p_1 - p_2) + \mathscr{M}(T_1 - T_2).
\end{aligned} \tag{2.5}$$

Relaxation processes are typically assumed for the B-N equations since the mixture will tilt towards phase equilibrium. The possible relaxation assumptions can be categorised into four(4) types: and they leads to the hierarchy of the sub-models for two-phase flow models some of which will be presented later in this thesis. In [92, 1, 98] in-depth analyses of the hierarchy can be seen. The relaxations possible are:

- **Velocity relaxation**, denoted as $u - relaxation$ (as $\mathscr{L} \to +\infty$):

  Due to velocity differences in the phases, a momentum transfer is assumed between the two phases or fluids leading to a velocity equilibrium i.e. $u = u_1 \equiv u_2$. With the assumption that the phase velocities are in equilibrium, the parameter $\mathscr{L}$ tends to infinity. The relaxation occurs in the terms $\mathscr{L}(u_1 - u_2)$ in the momentum equation.

- **Pressure relaxations**, denoted as as $p - relaxation$ (as $\mathscr{J} \to +\infty$):

  Due to the differences in pressure between the interacting fluid in the flow, a volume transfer is assumed between the two phases or fluids leading to pressure equilibrium i.e. $p = p_1 \equiv p_2$. A relaxation of the velocity and pressure at the same time results

into a mechanical equilibrium, where $p = p_1 \equiv p_2$ and $u = u_1 \equiv u_2$. These terms can be seen in $\mathscr{J}(p_1 - p_2), \mathscr{L}(u_1 - u_2)$.

- **Thermal relaxations**, denoted as $T - relaxation$ (as $\mathscr{M} \to +\infty$):

  Due to temperature differences between the phases, heat exchange is assumed between the two phases or fluids leading to thermal equilibrium between the phases. With $T = T_1 \equiv T_2$, a single energy equation applies to both fluid. These terms are $\mathscr{M}(T_1 - T_2)$ in the energy equation.

- **Chemical relaxations**, denoted as $\mu - relaxation$ (as $\mathscr{K} \to +\infty$):

  Due to chemical potential between the phases, a mass transfer assumed between the two phases or fluids leads to chemical equilibrium. These terms are in the mass conservation equation as $\mathscr{K}(\mu_1 - \mu_2)$, $u_I \mathscr{K}(\mu_1 - \mu_2)$ in the momentum conservation equation as $(\mu + \frac{1}{2}v^2)\mathscr{K}(\mu_1 - \mu_2)$ in the energy equation.

The B-N equation presented previously can be expressed below in the compact vector form:

$$\frac{\partial \mathbf{Q}}{\partial t} + \nabla \cdot \mathbf{F}(\mathbf{Q}) + \mathbf{H}(\mathbf{Q}) \cdot \nabla \alpha_1 = \mathbf{S}(\mathbf{Q}), \tag{2.6}$$

where the vector Q contains evolution variables, the flux of the system is determined by the vector F, and the velocity field is represented by the vector u. The non-conservative quantities are H and S. The S-vector includes all of the source terms, leaving H as a zero vector in this case.

$$\mathbf{Q}=\begin{bmatrix}\alpha_1\\ \alpha_1\rho_1\\ \alpha_1\rho_1 u_1\\ \alpha_1\rho_1 E_1\\ \alpha_2\rho_2\\ \alpha_2\rho_2 u_2\\ \alpha_2\rho_2 E_2\end{bmatrix}, F=\begin{bmatrix}\alpha_1\vec{u}_{\mathrm{I}}\\ \alpha_1\rho_1\vec{u}_1\\ \alpha_1\rho_2\vec{u}_2\\ \alpha_1(\rho_1\vec{u}_1+p_1)\\ \alpha_2(\rho_2\vec{u}_2+p_2)\\ \alpha_1\vec{u}_1\left(\rho_2E_1+p_1\right)\\ \alpha_1\vec{u}_2\left(\rho_2E_2+p_2\right)\end{bmatrix}, H=\begin{bmatrix}0\\ 0\\ 0\\ -p_I\\ p_I\\ -p_Iu_I\\ p_Iu_I\end{bmatrix} \quad \mathbf{S}=\begin{bmatrix}\Psi\\ \Phi\\ -\Phi\\ -\Lambda\\ \Lambda\\ \Gamma\\ -\Gamma\end{bmatrix} \tag{2.7}$$

Closure system:

From Eq.(2.7), the number of unknowns exceeds that of the equations. The number of variables in Eq.(2.7) and the number of equations do not coincide, an additional relation is needed to augment. To solve for the independent variables, additional closure relationship are required.. The B-N model can be closed using the following considerations:

- An Equation of State (EoS) for each phase that describes the behavior of each phase in terms of its pressure, density, and internal energy.
- Including a volume fraction constraint $\alpha_1+\alpha_2=1$ i.e. $\sum_{i=1}^{N}\alpha_i=1$.

Notwithstanding, the relationship above is not enough to solve for the unknown variables. To circumvent this, many authors reduced the equations to lesser unknowns by making equilibrium assumptions for pressure, velocity, and temperature in mixture regions that contain more than one fluid component. These formed the hierarchy of the reduced models. Some of them later in this thesis and using them for this research. These assumptions make it computationally less expensive, as solving the original seven equations is a numerically expensive task. The original full Baer-Nundiato model has a large number of waves and is susceptible to relaxation procedures. Andrianov [9] investigated the Riemann problem for a reduced two-phase flow Baer-Nunziato model, and was able to perform a singular value decomposition on the set of equations. The

characteristic velocities are from the eigenvalues of the hyperbolic equations and are

$$\lambda_{1,3} = U_i, \quad \lambda_2 = U_i - c_i, \quad \lambda_4 = U_i + c_i, \quad \lambda_5 = U_j, \quad \lambda_6 = U_j - c_j, \quad \lambda_7 = U_j + c_j$$

where the subscript i and j denotes the phases under consideration.
The speed of sound is given as:

$$c_i = \sqrt{\gamma_i(p_i + \pi_i/\rho_i} \tag{2.8}$$

The eigenvalues are real and linearly independent and as such the set of equations are hyperbolic although not strictly hyperbolic.

2.1.2 Saurel-Abgrall non-equilibrium model

In 1999, Saurel and Abgrall, using Drew's ensemble averaging procedure [38], modified Baer and Nunziato's for immiscible two-phase flow applications. The Saurel–Abgrall model differs from the Baer-Nunziato model in the manner in which pressure and velocity at the interface are characterized. The numerical approximation of non-conservative terms when the functions are discontinuous (presence of shock-wave and interface) is one of the model's challenges. The solution of the Riemann problem to the equations is difficult as the seven waves generated are not orderly. Several authors [131, 7, 8, 198, 51, 5, 28, 197], have made improvements and contributions to this model.

The original Saurel-Abgrall models have seven equations, but there are many other simplified sub-models with fewer equations depending on the application. The seven equations are form on a hyperbolic system of equations that describe the conservation of mass, momentum, and energy in each phase, as well as the evolution of the interface between the phases. The seven-equation model is expressed as:

$$
\begin{cases}
\textbf{Phase 1} \\
\frac{\partial}{\partial t}\alpha_1 + \vec{u}_I \cdot \nabla\alpha_1 = \mathscr{J}(p_1 - p_2) \\
\frac{\partial}{\partial t}(\alpha_1\rho_1) + \nabla\cdot(\alpha_1\rho_1\vec{u}_1) = 0 \\
\frac{\partial}{\partial t}(\alpha_1\rho_1 u_1) + \nabla\cdot(\alpha_1(\rho_1\vec{u}_1 + p_1)) - p_I\cdot\nabla\alpha_1 = \mathscr{L}(u_2 - u_1) \\
\frac{\partial}{\partial t}(\alpha_1\rho_1 E_1) + \nabla\cdot(\alpha_1\vec{u}_1(\rho_1 E_1 + p_1)) - p_I u_1\cdot\nabla\alpha_1 = \bar{u}_I\mathscr{L}(u_2 - u_1) - \mathscr{K}\bar{p}_I(p_1 - p_2) \\
\textbf{Phase 2} \\
\frac{\partial}{\partial t}(\alpha_2\rho_2) + \nabla\cdot(\alpha_2\rho_2\vec{u}_2) = 0 \\
\frac{\partial}{\partial t}(\alpha_2\rho_2 u_2) + \nabla\cdot(\alpha_2\vec{u}_2(\rho_2 + p_2)) + p_I\cdot\nabla\alpha_1 = \mathscr{L}(u_2 - u_1) \\
\frac{\partial}{\partial t}(\alpha_2\rho_2 E_2) + \nabla\cdot(\alpha_2\vec{u}_2(\rho_2 E_2 + p_2)) - p_I u_I\cdot\nabla\alpha_1 = -\bar{u}_I\mathscr{L}(u_2 - u_1) + \bar{p}_1\mathscr{J}(p_1 - p_2)
\end{cases}
\tag{2.9}
$$

These models can presented in a compact vector form below

$$
\frac{\partial \mathbf{Q}}{\partial t} + \nabla\cdot\mathbf{F}(\mathbf{Q}) + \mathbf{H}(\mathbf{Q})\cdot\nabla\alpha_1 = \mathbf{S}_v(\mathbf{Q}) + \mathbf{S}_p(\mathbf{Q}) \tag{2.10}
$$

where Q is the vector of conserved variables, F represents the flux tensor, and vector u is the velocity field. The S-vector includes all of the source terms, leaving H as a zero vector in this case. S_p is the non-conserved variables for the pressure relaxation and S_v is the non-conserved variables for the velocity relaxation.

$$\mathbf{Q}=\begin{bmatrix}\alpha_1\\ \alpha_1\rho_1\\ \alpha_1\rho_1\mathbf{u}\\ \alpha_1\rho_1E_1\\ \alpha_2\rho_2\\ \alpha_2\rho_2\mathbf{u}\\ \alpha_2\rho_2E_2\end{bmatrix},\quad F=\begin{bmatrix}\alpha_1\mathbf{u}_I\\ \alpha_1\rho_1\mathbf{u}\\ \alpha_1\rho_1\mathbf{u}^2+\alpha_1p_1\\ \alpha_1\mathbf{u}(E_1+p_1)\\ \alpha_2\rho_2\mathbf{u}\\ \alpha_2\rho_2\mathbf{u}^2+\alpha_2p_2\\ \alpha_2\mathbf{u}(E_2+p_2)\end{bmatrix},\quad \mathbf{H}(\mathbf{Q})=\begin{bmatrix}-u_I\\ 0\\ p_I\\ u_Ip_I\\ 0\\ -p_I\\ -u_Ip_I\end{bmatrix},\quad \mathbf{S}_v=\begin{bmatrix}\mathscr{J}(p_1-p_2)\\ 0\\ 0\\ \mathscr{J}p_1(p_1-p_2)\\ 0\\ 0\\ \mathscr{J}p_1(p_1-p_2)\end{bmatrix},$$

$$\mathbf{S}_p=\begin{bmatrix}0\\ 0\\ -\mathscr{L}(u_1-u_2)\\ -\mathscr{L}u_I(u_1-u_2)\\ 0\\ \mathscr{L}(u_1-u_2)\\ -\mathscr{L}u_I(u_1-u_2)\end{bmatrix}$$

Closure system:

To provide closure to the Saurel-Abgrall seven-equations, in addition to the volume fraction constraint of both phases $\alpha_1+\alpha_2=1$ and equation of state for each phase, interfacial velocities and interfacial pressure are symmetric for both phases and are defined as:

$$u_I=\overline{\mathrm{u_I}}+\mathrm{sgn}(\nabla\cdot(\alpha_1))\frac{p_2-p_1}{Z_1+Z_2}, \tag{2.11}$$

$$p_I=\overline{\mathrm{p_I}}+\mathrm{sgn}(\nabla\cdot\alpha_1)\frac{Z_1Z_2}{Z_1+Z_2}(u_2-u_1), \tag{2.12}$$

where the interface velocity $\overline{u_I}$ and volume average pressure $\overline{p_I}$ both acting within the cloud of droplet or bubble are given as:

$$\overline{u_I} = \frac{Z_1 u_1 + Z_2 u_2}{Z_1 + Z_2} \tag{2.13}$$

$$\overline{p_I} = \frac{Z_2 p_1 + Z_1 p_2}{Z_1 + Z_2} \tag{2.14}$$

Eq. 2.15 and 2.16 expresses the pressure relaxation $\mathscr{J}$ and velocity relaxation $\mathscr{L}$ rates which controls how the relaxation process tends towards mechanical equilibrium i.e pressure and velocity equilibrium. As the fluid undergoes advection, the volume fraction of each phase changes due to pressure differences within the fluid. These variations are controlled by the $\mathscr{J}(p_1 - p_2)$.

$$\mathscr{J} = \frac{A_I}{Z_1 + Z_2} \tag{2.15}$$

and

$$\mathscr{L} = \frac{1}{2}\mathscr{J} Z_1 Z_2, \tag{2.16}$$

where $Z_i = \rho_i c_i$ is the acoustic impedance of each phase i and c_i is the speed of sound of each phase i, A_I represents the mixture's interfacial area.

For most cases, the next sub-models that will be discussed are more conservative, robust, and computationally efficient for separated flow (the main area of interest in this research), where the phase boundary is described in detail.

2.1.3 Romenski seven-equation model

The B-N and S-A seven equations, as explained previously, are non-conservative. Romenski proposed and created a new set of seven (7) conservative and hyperbolic equations that are similar to the B-N-type models. His derivations were founded on extended irreversible thermodynamic laws and a thermodynamically compatible formalism system [43, 129, 161] . They are referred to as the Symmetric Hyperbolic and Thermodynamically Compati-

ble (SHTC) model in the diffuse interface schemes. They differ from the B-N and S-A equations in one dimension due to the definition of interfacial pressure. The differences are clearer for the multidimensional case, where the momentum equations of the individual phases are coupled with lift forces that are related to phase vorticities. The characterization of interfacial velocity is identical to that specified in the Saurel-Abgrall seven-equation model. This model has been applied by authors([161, 129, 128]) to solve the compressible multiphase problem, and some modifications have been made to suit certain conditions. The original equation is expressed using the state parameters of the mixture instead of the state parameters of each individual phase, as in the B-N and S-A models. For comparison purposes with the B-N-type model, Romenski and Toro [129] reformulated the Romenski seven-equation model in terms of parameters of state for the individual phases using the individual density and velocity for each phase. The phases are characterised using volume fraction and mass fraction constraints and presented below in one dimension for simplicity [129].

$$\begin{cases} \frac{\partial}{\partial t}\left(\alpha_1\rho_1+\alpha_2\rho_2\right)+\frac{\partial}{\partial x}\left(\alpha_1\rho_1u_1+\alpha_2\rho_2u_2\right)=0 \\ \frac{\partial}{\partial t}\left(\alpha_1\rho_1u_1+\alpha_2\rho_2u_2\right)+\frac{\partial}{\partial x}\left(\alpha_1\rho_1u_1^2+\alpha_2\rho_2u_2^2+\alpha_1p_1+\alpha_2p_2\right)=0 \\ \frac{\partial}{\partial t}\left(\left(\alpha_1\rho_1+\alpha_2\rho_2\right)\alpha\right)+\frac{\partial}{\partial x}\left(\left(\alpha_1\rho_1u_1+\alpha_2\rho_2u_2\right)\alpha\right)=-\Phi \\ \frac{\partial}{\partial t}\left(\alpha_1\rho_1\right)+\frac{\partial}{\partial x}\left(\alpha_1\rho_1u_1\right)=0 \\ \frac{\partial}{\partial t}\left(u_1-u_2\right)+\frac{\partial}{\partial x}\left(\frac{u_1^2}{2}-\frac{u_2^2}{2}+e_1+\frac{p_1}{\rho_1}-e_2-\frac{p_2}{\rho_2}\right)=-\Pi \\ \frac{\partial}{\partial t}\left(\alpha_1\rho_1e_1+\alpha_2\rho_2e_2+\frac{u_1^2}{2}+\frac{u_2^2}{2}\right)+ \\ \frac{\partial}{\partial x}\left(\alpha_1\rho_1u_1\left(e_1+\frac{p_1}{\rho_1}+\frac{u_1^2}{2}\right)+\alpha_2\rho_2u_2\left(e_2+\frac{p_2}{\rho_2}+\frac{u_2^2}{2}\right)\right)=0. \end{cases} \tag{2.17}$$

Where source terms at the RHS are expressed as:

$$\Phi=-\frac{1}{\tau}\left(p_1-p_2\right),\Pi=-\kappa\frac{\left(\alpha_1\rho_1\alpha_2\rho_2\right)}{\rho^2}(u_1-u_2), \tag{2.18}$$

where the pressure relaxation parameter τ and coefficient of interfacial friction κ are functions of parameters of state of the mixture.

The interfacial speed is the same as that of Baer-Nunziato and is expressed as follows:

$$u_I = \frac{\alpha_1\rho_1 u_1 + \alpha_2\rho_2 u_2}{\alpha_1\rho_1 + \alpha_2\rho_2}, \tag{2.19}$$

and the interfacial pressure is given as:

$$p_I = \frac{\alpha_1\rho_1 p_2 + \alpha_2\rho_2 p_1}{\alpha_1\rho_1 + \alpha_2\rho_2}. \tag{2.20}$$

In one dimension, the Romenski's model can generally be expressed in compact-vector format below.

$$\frac{\partial \mathbf{Q}}{\partial t} + \frac{\partial}{\partial x}\mathbf{F}(\mathbf{Q}) = \mathbf{S}(\mathbf{Q}) \tag{2.21}$$

where Q is the vector of conserved variables, F represents the flux tensor, and vector u is the velocity field. S is the source terms.

$$\mathbf{Q} = \begin{bmatrix} \alpha_1\rho_1 + \alpha_2\rho_2 \\ \alpha_1\rho_1 u_1 + \alpha_2\rho_2 u_2 \\ (\alpha_1\rho_1 + \alpha_2\rho_2)\,\alpha \\ \alpha_1\rho_1 \\ u_1 - u_2 \\ \alpha_1\rho_1 e_1 + \alpha_1\rho_1 e_1 + \frac{p_1}{\rho_1} + \frac{u_1^2}{2} \end{bmatrix}, \quad F = \begin{bmatrix} \alpha_1\rho_1 u_1 + \alpha_2\rho_2 u_2 \\ \alpha_1\rho_1 u_1^2 + \alpha_2\rho_2 u_2^2 + \alpha_1 p_1 + \alpha_2 p_2 \\ (\alpha_1\rho_1 u_1 + \alpha_2\rho_2 u_2)\alpha \\ \alpha_1\rho_1 u_1 \\ \frac{u_1^2}{2} - \frac{u_2^2}{2} + e_1 + \frac{p_1}{\rho_1} - e_2 - \frac{p_2}{\rho_2} \\ \alpha_1\rho_1 u_1(e_1 + \frac{p_1}{\rho_1} + \frac{u_1^2}{2}) + \alpha_2\rho_2 u_2(e_2 + \frac{p_2}{\rho_2} + \frac{u_2^2}{2}) \end{bmatrix},$$

$$\mathbf{S}_v = \begin{bmatrix} 0 \\ 0 \\ -\Phi \\ -\Pi \\ 0 \\ 0 \\ \\ \end{bmatrix}$$

2.2 Mechanical equilibrium Model

The mechanical equilibrium model, also called the ”one pressure, one velocity” model, assumes that momentum, energy, and mass transfer between different phases of a fluid reach equilibrium due to differences in their thermodynamic properties. This model maintains a single pressure and a single velocity for all the components of the fluid. When considering two-dimensional space with the dimensions x and y, the model provides the velocity components and pressure for each component at multi-material interfaces and is given as:

$$p_1 = p_2 \equiv p,$$

$$u_1 = u_2 \equiv u,$$

$$v_1 = v_2 \equiv v$$

This is enforced through the isobaric assumption of the B-N equations. Due to the pressure difference between the interacting components or phases, a volume transfer is assumed. Mechanical phase equilibrium is achieved when two phases or fluids interact. With mechanical equilibrium implemented, the full seven (7) Baer-Nundiato seven equations are mostly reduced into five-equation models , which are now simpler to solve numerically. These categories of models are tailored for treating the interface of non-miscible fluids in non-reacting flows such as a liquid-gas mixture and flows that involve a free surface or pure interface . Note that this model only assumes mechanical equilibrium in the fluid; each phase remains in thermal disequilibrium as there is no heat exchange between the two phase. The most popular models in this category are Allaire et al. (2002) and Kapila et al. (2001).

These equations include two continuity equations for each phase of the fluid, one momentum equation, and one energy equation. In addition to these conservative equations, there is an additional non-conservative advection equation for the volume fraction equation that is coupled with them. Models in this category all have the same four conservative equations, presented in Eq.(2.22), with slightly varying formulations in the non-conservative advection equation for the volume fraction, which is used to determine the position of

the material interface between the two fluids. Kapila et al. [79] differ in the advection equation by including a $K\nabla \cdot u$ term (2.22) that describes the compressibility and thermodynamic properties of the two-phase fluid's mixture region. For flows involving bubble dynamics, the additional $K\nabla \cdot u$ in the Kapila model allows for the prediction of gas bubble collapse and rebound in a liquid [138, 164], as it accounts for expansion and compression in mixture regions, which are absent in Allaire et al.'s 5-equation model.

The Allaire et al. [4] five-equation is very robust and uses the 'mixture-mixture' speed of sound (Eq. 2.29), which is monotonic and derived from the mixture rule. Kreeft and Koren improved upon the Kapila et al.'s five equation models by replacing the advection equation Eq.(2.30) to describe the topology of the volume fraction of two-fluid flow. The mechanical and thermodynamical exchange of energy between the two interacting fluids is well described in the additional energy equation Eq.(2.30) included by Kreeft and Koren. These five-equation class of models have been used extensively by many authors [138, 172, 59, 10, 199, 2, 29].

According to authors such as Saurel (2019) and Panchal (2022), the non-monotonic nature of the mixture speed of sound in the Kapila model, as well as the non-conservative terms of the volume fraction equation, present a challenge of numerical instability near strong shocks and difficulty maintaining volume fraction positivity. But with an algebraic method for presenting the non-conservative terms using Johnsen and Colonius [73] approach and also the introduction of monotonic speed of sound to the 5-equation model of Kapila [199, 172], the issues mentioned or noted above are of less concern and this is the motivation for using the 5-equation models in this research rather than the 6-equation pressure equili-brium model. This work, uses the mixture-mixture speed of sound instead of the Wood speed of sound in the five-equation model of Kapila et al.; this is consistent with Zhang's paper [199] and has been used successfully by other authors [102, 114, 143, 29]. It is now well established that the non-motononic behaviours of the Wood's speed of sound has been solved and replaced by the mixture-mixture speed of sound. Other additional parameters (such as capillarity and viscous effects, [114],

surface tension, mass transfer [127], gravitational effect [99], cavitation [31]) have been included into the five-equation model by various authors.

$$\text{Four equations for a two-phase flow:} \begin{cases} \frac{\partial \alpha_1 \rho_1}{\partial t} + \nabla \cdot (\alpha_1 \rho_1 \mathbf{u}) & = 0 \\ \frac{\partial \alpha_2 \rho_2}{\partial t} + \nabla \cdot (\alpha_2 \rho_2 \mathbf{u}) & = 0 \\ \frac{\partial \rho \mathbf{u}}{\partial t} + \nabla \cdot (\rho \mathbf{u} \otimes \mathbf{u}) + \nabla p & = 0 \\ \frac{\partial \rho E}{\partial t} + \nabla \cdot (\rho E + p)\mathbf{u} & = 0 \end{cases} \tag{2.22}$$

where the subscript 1, 2 represents the fluid's component, α is the volume fraction of each component, ρ is the density, $\mathbf{u} = (u, v, w)$ is the velocity, p is the pressure and E is the total specific energy.

The advection equation for volume fraction in the Allaire's et al. 5-equation model

$$\begin{cases} \frac{\partial \alpha_1}{\partial t} + \mathbf{u} \cdot \nabla \alpha_1 = 0 \,, \end{cases} \tag{2.23}$$

The advection equation for volume fraction in the Kapila's et al. 5-equation model

$$\begin{cases} \frac{\partial \alpha_1}{\partial t} + \mathbf{u} \cdot \nabla \alpha_1 = K \nabla \cdot \mathbf{u} \end{cases} \tag{2.24}$$

Tiwari[164, 199] recast the Eq. 2.24 into Eq. 2.25 so it can be in conservative form as seen below:

$$\begin{cases} \frac{\partial \alpha_1}{\partial t} + \nabla \cdot \alpha_1 \mathbf{u} = K \nabla \cdot \mathbf{u} \end{cases} \tag{2.25}$$

where the K term in the advection equation above is defined as:

$$K = \frac{\alpha_1 \rho_1 c_2^2}{\alpha_2 \rho_1 c_1^2 + \alpha_1 \rho_2 c_2^2} \tag{2.26}$$

The Wood's speed of sound for the mixture in the original Kapila et al. model is :

$$\frac{1}{\rho c^2} = \frac{\alpha_1}{\rho_1 c_1^2} + \frac{\alpha_2}{\rho_2 c_2^2} \tag{2.27}$$

where the speed of sound of each phase is given as:

$$c_1 = \sqrt{\frac{\gamma_1}{\rho_1}(p + p_{c,1})}, c_2 = \sqrt{\frac{\gamma_2}{\rho_2}(p + p_{c,2})} \tag{2.28}$$

The 'mixture-mixture' of Allaire et al. speed of sound which derived from the mixture stiffened-gas SG-EoS is given as :

$$c = \sqrt{\frac{\gamma(p + \pi_\infty)}{\rho}} \tag{2.29}$$

where γ is the specific heat ratios and π_∞ is a reference pressure, which is set to 0 for gases, the mixture density $\rho = \alpha_1\rho_1 + \alpha_2\rho_2$.
The energy equation by Koren and Kreft replacing the volume fraction in the Kapila's et al. 5-equation model is presented below

$$\left\{ \frac{\partial(\alpha\rho_1 E_1)}{\partial t} + \nabla \cdot (\alpha\rho_1 E_1 \mathbf{u}) + \nabla \cdot (\alpha p \mathbf{u}) = W_M + W_T \right. \tag{2.30}$$

The W_M and W_T term represent the energy-exchange terms of mechanical work rate and thermodynamic work rate between fluid 1 and fluid 2.

$$W_M = p\mathbf{u} \cdot \nabla\alpha + (\alpha - \beta)\mathbf{u} \cdot \nabla p \tag{2.31}$$

$$W_T = p\alpha(1-\alpha)\frac{\tau_2 - \tau_1}{\tau}\nabla \cdot \mathbf{u} \tag{2.32}$$

where τ_1 and τ_2 are isentropic compressibilities

$$\tau = \tau_1 + \tau_2 = \frac{\alpha_1}{\rho_1 c_1^2} + \frac{\alpha_2}{\rho_2 c_2^2} \tag{2.33}$$

These models can generally be expressed as a non-linear system of PDE in two phase

fluid are presented below.

$$\frac{\partial \mathbf{Q}}{\partial t} + \nabla \cdot \mathbf{F}(\mathbf{Q}) + \mathbf{H}(\mathbf{Q}) \nabla \cdot u = \mathbf{S}(\mathbf{Q}) \tag{2.34}$$

where Q is the vector of conserved variables, F represents the flux tensor, and vector u is the velocity field. The S-vector includes all of the source terms, in which in this case is a zero vector.

Q, F and H are then defined in the form as presented in Eq.(2.35) (Allaire et al. model) and Eq. (2.36) (Kapila et al.) for a two-phase flow.

The Allaire's et al. 5-equation model presented in a vector form:

$$Q = \begin{bmatrix} \alpha_1 \\ \alpha_1\rho_1 \\ \alpha_2\rho_2 \\ \rho\mathbf{u} \\ \rho E \end{bmatrix}, \quad F = \begin{bmatrix} \alpha_1\mathbf{u} \\ \alpha_1\rho_1\mathbf{u} \\ \alpha_2\rho_2\mathbf{u} \\ \rho\mathbf{v}^2 + p \\ \mathbf{u}(\rho E + P) \end{bmatrix} \quad H = \begin{bmatrix} -\alpha_1 \\ 0 \\ 0 \\ 0 \\ 0 \end{bmatrix}. \tag{2.35}$$

The Kapila's et al. 5-equation model presented in a vector form:

$$Q = \begin{bmatrix} \alpha_1 \\ \alpha_1\rho_1 \\ \alpha_2\rho_2 \\ \rho\mathbf{u} \\ \rho E \end{bmatrix}, \quad F = \begin{bmatrix} \alpha_1\mathbf{u} \\ \alpha_1\rho_1\mathbf{u} \\ \alpha_2\rho_2\mathbf{u} \\ \rho\mathbf{u}^2 + p \\ \mathbf{u}(\rho E + P) \end{bmatrix} \quad H = \begin{bmatrix} -\alpha_1 - \mathbf{K} \\ 0 \\ 0 \\ 0 \\ 0 \end{bmatrix}. \tag{2.36}$$

The density, momentum, kinetic energy, and internal energy of the mixture are presented below.:

$$\rho = (\alpha\rho)_1 + (\alpha\rho)_2 = \sum_{i=1}^{N} (\alpha\rho)_i : \text{ mixture density} \tag{2.37}$$

$$\rho\vec{u} = ((\alpha\rho)_1 + (\alpha\rho)_2)\vec{u} = \sum_{i=1}^{N}(\alpha\rho)_i\vec{u} \ : \text{ mixture momentum} \tag{2.38}$$

$$\rho e_{\mathrm{K}} = \frac{\rho_i.u^2}{2} : \text{ mixture kinetic energy.} \tag{2.39}$$

$$\rho e_{\mathrm{I}} = (\alpha\rho)_1 e_1 + (\alpha\rho)_2 e_2 = \sum_{i=1}^{N}(\alpha\rho\ e)_i \ : \text{ mixture internal energy.} \tag{2.40}$$

The total energy can now be expressed as:

$$\rho E_{\mathrm{T}} = ((\alpha\rho)_1 e_1 + (\alpha\rho)_2 e_2 + \sum_{i=1}^{N}\frac{\rho_i.\mathbf{u}\cdot\mathbf{u}}{2}) \tag{2.41}$$

To determine the internal energy and solve the equations, it is practical to apply the stiffened equation of state (EoS) to both components of the fluid, which is given as:

$$p_i = (\gamma_i - 1)\,\rho_i e_i - \gamma_i p_{c,i}, \ \ i = 1,2 \tag{2.42}$$

Using the stiffened EoS, the internal energy can now be expressed as:

$$\rho e_i = \frac{p + \gamma_i.p_c,i}{\gamma_i - 1}) \tag{2.43}$$

and the total energy below:

$$\rho E = \sum_{i=1}^{N}\alpha_i(\frac{p + \gamma_i.p_c,i}{\gamma_i - 1} + \frac{\rho_i.\mathbf{u}\cdot\mathbf{u}}{2}) \tag{2.44}$$

From the five-equations, as shown in Eq. (2.23) and Eq. (2.30), the advection equation of the volume fraction is in a non-conservative form which will present some difficulties when solving our five-model equations.The advection equation is restated in conservative form using the Johnsen and Colonius [73] approach.

First, let f represent a vector in three-dimension and is defined as, $f = \alpha_1 u = [\alpha_1\mathbf{u}, \alpha_1 v, \alpha_1 w]^{\mathrm{T}}$

Divergence of f then is:

$$\nabla \cdot f = \frac{\partial}{\partial x}(\alpha_1 u) + \frac{\partial}{\partial y}(\alpha_1 v) + \frac{\partial}{\partial z}(\alpha_1 w)$$

$$= \alpha_1 \left(\frac{\partial u}{\partial x} + \frac{\partial v}{\partial y} + \frac{\partial w}{\partial z} \right) + \left(u\frac{\partial \alpha_1}{\partial x} + v\frac{\partial \alpha_1}{\partial y} + w\frac{\partial \alpha_1}{\partial z} \right)$$

$$= \alpha_1 \nabla \cdot \mathbf{u} + \mathbf{u} \cdot \nabla \alpha_1$$

and then,

$$\mathbf{u} \cdot \nabla \alpha_1 = \nabla \cdot f - \alpha_1 \nabla \cdot \mathbf{u}.$$

Substituting $\alpha_1 \nabla \cdot \mathbf{u}$ into the non-conservative volume fraction equation in Eq. (2.23) and Eq. (2.30) to obtain the quasi-conservative form, the equation for the advection of the volume fraction can be written as Eq. (2.45) and Eq. (2.46).

For Allaire's et al.

$$\frac{\partial \alpha_1}{\partial t} + \nabla \cdot f = (\alpha_1) \nabla \cdot \mathbf{u} \tag{2.45}$$

For Kapila's et al.

$$\frac{\partial \alpha_1}{\partial t} + \nabla \cdot f = (\alpha_1 + K) \nabla \cdot \mathbf{u} \tag{2.46}$$

In the quasi-conservative form, the advection equation for the volume fraction in the Allaire's model is explicitly solved. It directly updates the volume fraction based on the gradient of the volume fraction and the velocity field ($\mathbf{u}$) without any additional terms. It's a straightforward and computationally efficient approach, and well-suited for problems that don't involve strong shocks or intricate thermodynamic interactions.

Conversely, in the quasi-conservative form of the Kapila's model, the extra term ($K\nabla \cdot \mathbf{u}$) introduces an implicit treatment in the model to address the impact of compressibility and thermodynamic properties. As a result, Kapila's model can be considered a quasi-implicit treatment, as it combines both explicit and implicit approach. Although the explicit approach for solving the advection of volume fraction, as seen in Allaire's model,

are simpler and computationally efficient, on the other hand, solving implicitly as in Kapila's model, offer more stability especially for strong shocks but demand higher computational resources due to the way the equation is being treated.

2.3 Velocity equilibrium or Pressure-disequilibrium model

As noted by Saurel et al. [136] and previously mentioned, one of the difficulties experienced by authors is the non-monotonicity of Wood's speed of sound (Eq.2.33) used in the Kapila 5-equation model, as well as the non-conservative nature of the K term. Saurel [135] tried to circumvent this by proposing a six-equation model and introducing a monotonic mixture speed of sound called the monotonic frozen speed of sound. The Saurel six-equations models are pressure disequilibrium models from the Saurel-Abgrall seven-equations previously discussed. Assuming the velocity of the two interacting fluids is in equilibrium $u_1 = u_2 \equiv u$. The result is a single-velocity, compressible, two-phase flow model with two pressures for the mixture phase. The set of six equations encompasses conservation laws for the quantities of mass, momentum, and energy for both phases, along with an equation for the volume fraction of one of the phases. Zein [198] introduced heat transfer into the original six-equation model, which, in its absence of mass and heat transfer, can be expressed as follows:

$$
\begin{cases}
\textbf{Phase 1} \\
\frac{\partial}{\partial t}\alpha_1 + \mathbf{u}\cdot\nabla\alpha_1 = \mu(p_1 - p_2) \\
\frac{\partial}{\partial t}(\alpha_1\rho_1) + \nabla\cdot(\alpha_1\rho_1\mathbf{u}) = 0 \\
\frac{\partial}{\partial t}(\alpha_1\rho_1 E_1) + \nabla\cdot(\alpha_1\mathbf{u}(\rho_1 E_1 + p_1)) = -\mu\bar{p}_I(p_1 - p_2) \\
\textbf{Phase 2} \\
\frac{\partial}{\partial t}(\alpha_2\rho_2) + \nabla\cdot(\alpha_2\rho_2\mathbf{u}) = 0 \\
\frac{\partial}{\partial t}\alpha_1\rho_1 E_1 + \nabla\cdot\alpha_1(\rho_1 E_1 + p_1\mathbf{u}) = 0 \\
\frac{\partial}{\partial t}(\alpha_2\rho_2 E_2) + \nabla\cdot(\alpha_2\mathbf{u}(\rho_2 E_2 + p_2)) = \mu\bar{p}_I(p_1 - p_2)
\end{cases}
\tag{2.47}
$$

These models, which can generally be expressed as a non-linear system of PDE in a two phase fluid, are presented below.

$$\frac{\partial \mathbf{Q}}{\partial t} + \nabla \cdot \mathbf{F}(\mathbf{Q}) + \mathbf{H}(\mathbf{Q}) \nabla \mathbf{u} = \mathbf{S}(\mathbf{Q}) \tag{2.48}$$

where Q is the vector of conserved variables, F represents the flux tensor, and vector u is the velocity field. The S and H are are non-conservative quantities which includes all of the source terms.

$$\mathbf{U} = \begin{bmatrix} \alpha_1 \\ \alpha_1\rho_1 \\ \alpha_2\rho_2 \\ \rho\mathbf{u} \\ \alpha_1\rho_1 E_1 \\ \alpha_2\rho_2 E_2 \end{bmatrix}, \quad \mathbf{F} = \begin{bmatrix} \alpha_1\mathbf{u} \\ \alpha_1\rho_1\mathbf{u} \\ \alpha_2\rho_2\mathbf{u} \\ \rho\mathbf{u}\otimes\mathbf{u} + p\mathbf{I} \\ \alpha_1\rho_1 E_1\mathbf{u} \\ \alpha_2\rho_2 E_2\mathbf{u} \end{bmatrix}, \quad \mathbf{H} = \begin{bmatrix} -\alpha_1 \\ 0 \\ 0 \\ \mathbf{0} \\ \alpha_1 p_1 \\ \alpha_2 p_2 \end{bmatrix}, \quad \mathbf{S} = \begin{bmatrix} \mu(p_1 - p_2) \\ 0 \\ 0 \\ 0 \\ -\mu p_I(p_1 - p_2) \\ \mu p_I(p_1 - p_2) \end{bmatrix} \tag{2.49}$$

Interfacial pressure is expressed same as the Saurel's seven-equations and corresponds to the mixture total pressure:

$$p_I = \frac{Z_1 p_1 + Z_2 p_2}{Z_1 + Z_2} \tag{2.50}$$

The variable Z_i denotes the acoustic impedance of phase i, where ρ_i represents the density of the phase and c_i is the speed of sound in that particular phase.The mechanical equilibrium state is reached at the end of relaxation processes controlled by the pressure relaxation term $\mu > 0$.

As $\mu \to +\infty$, the six-equations in the presence of pressure relaxation converges to the Kapila five-equation models. The speed of sound of the mixture is defined to be monotonic and given as:

$$c^2 = \sum_{i=1}^{2} \frac{\alpha_i \rho_i c_i^2}{\rho} \tag{2.51}$$

The mixture's energy equation is the sum of the internal energies of the two fluids or phases:

$$\frac{\partial}{\partial t}\left(\rho e+\frac{1}{2}\rho u^2\right)+\nabla\cdot\left(\rho e+\frac{1}{2}\rho u^2+\alpha_1 p_1+\alpha_2 p_2\right)=0, \tag{2.52}$$

where the mixture density and internal energies are given as:

$$\rho=\alpha_1\rho_1+\alpha_2\rho_2 \tag{2.53}$$

$$\rho e=\alpha_1\rho_1 e_1+\alpha_2\rho_2 e_2 \tag{2.54}$$

According to the study by Schmidmayer et.al. [138], pressure-disequilibrium models are approximately 5% more computationally intensive than the models developed by Allaire et al. and Kapila et al.

2.4 Thermal-equilibrium and Mechanical equilibrium of Abgrall et al.

The four-equation model introduced by Abgrall [131] assumes a thermal and mechanical equilibrium between the interacting fluids in the mixture using the seven-equation system of Baer-Nunziato. It is the simplest model in the DIM category, formulated from the Baer-Nunziato seven equation models. The four equations consist of one equation for the conservation of mass for each phase i and an equation for the mixture's momentum and internal energy. Temperature, velocity fields and pressure between the two phases are assumed to be homogeneous. The four-equation model's straightforward nature allows for integration of additional physical phenomena, such as viscosity, surface tension, and phase change, through source terms. Demou et al. [33] incorporated the effects of viscosity, thermal conductivity, surface tension and gravity into the classically conservative four-equation model developed by Abgrall to address nucleate boiling flow and phase change.

$$\text{Four equations:} \begin{cases} \frac{\partial \alpha_1 \rho_1}{\partial t} + \nabla \cdot (\alpha_1 \rho_1 u) & = \Gamma \\ \frac{\partial \alpha_2 \rho_2}{\partial t} + \nabla \cdot (\alpha_2 \rho_2 u) & = \Gamma \\ \frac{\partial \rho u}{\partial t} + \nabla \cdot (\rho u \otimes u) + \nabla p & = 0 \\ \frac{\partial \rho E}{\partial t} + \nabla \cdot (\rho E + p) u & = 0 \end{cases} \tag{2.55}$$

where the subscripts 1, 2 represents the phases, α is the volume fraction of each phase or component, ρ is the mixture density, $\mathbf{u} = (u, v, w)$ is the mixture velocity, p is the mixture pressure and E is the mixture total specific energy, Γ are the source terms which are zero if additional physics such as mass transfer are not included. The energy of the mixture is given as $E = e + \frac{1}{2}u^2$ with the internal energy $e = \alpha_1 e_1 + \alpha_2 e_2$. The speed of sound is the Wood's speed of sound, which is the same as the one in Kapila et al. five-equation models and is given as

$$c_{wood} = \sqrt{\rho \left(\frac{\alpha_1}{\rho_1 c_1^2} + \frac{\alpha_2}{\rho_2 c_2^2} \right)} \tag{2.56}$$

where $\rho = \alpha_1 \rho_1 + \alpha_2 \rho_2$

In a non-linear system of PDE , the Abgrall equation can be written and presented below.

$$\frac{\partial \mathbf{Q}}{\partial t} + \nabla \cdot \mathbf{F}(\mathbf{Q}) + \mathbf{H}(\mathbf{Q}) \nabla \cdot \mathbf{u} = \mathbf{S}(\mathbf{Q}). \tag{2.57}$$

where Q is the vector of conserved variables , F is a flux tensor, **u** is the velocity field, and H and S are non-conservative quantities. S here is a zero vector.

In a compact matrix-vector form, the four equations:

$$Q = \begin{bmatrix} \alpha_1 \rho_1 \\ \alpha_2 \rho_2 \\ \rho \mathbf{u} \\ \rho E \end{bmatrix}, \quad F = \begin{bmatrix} \alpha_1 \rho_1 \mathbf{u} \\ \alpha_2 \rho_2 \mathbf{u} \\ \rho \mathbf{u}^2 + p \\ \mathbf{u}(\rho E + p) \end{bmatrix} \quad H = \begin{bmatrix} \Gamma \\ \Gamma \\ 0 \\ 0 \end{bmatrix}. \tag{2.58}$$

Table 2.1: A summarised overview of the hierarchy of diffuse interface models, and pros and cons for their use in compressible multiphase flow

Diffuse Interface Models	**Pros**	**Cons**
1. Baer-Nunziato 7-eqn.	- Can be used for a large scale of problems.	- Difficult to solve numerically. - Hyperbolic (non-symmetric). - Cannot be expressed fully in a conservative form.
2. Saurel-Abgrall 7-eqn.	- Able to deal with permeable and impermeable interfaces [89, 136].	- Computationally costly.
3. Romenski 7-eqn.	- It is fully conservative and has the opportunity for a direct formulation of discontinuous solutions. - Hyperbolic (symmetric)	- Expressed using the state parameters of the mixture instead of the state parameters of each individual phase. [129]. - Computationally expensive.
4. Allaire et al. 5-eqn.	- Very robust.	- Cannot take into account the compression and expansion in the mixture zone. [139].

Table 2.1 (Continued): A summarised overview of the hierarchy of diffuse interface models, and pros and cons for their use in compressible multiphase flow

Diffuse Interface Models	Pros	Cons
	- Uses the monotonic ”mixture-mixture” speed of sound.	- For the Rayleigh collapse problem, it cannot provide a prediction for the minimum radius or collapse time. [139].
5. Kapila et al. 5-eqn.	- Allows the prediction of gas bubble collapse and rebound in a liquid for flows [138] involving bubble dynamics. - Thermodynamically consistent model.	- Non-monotonic nature of the mixture speed of sound. - Non-conservative terms of the volume fraction equation. - Instabilities in the vicinity of the interface during intense compression and expansion of fluid.

6. Saurel's 6-eqn.	- It preserves the positivity of the volume fraction [126].	- Computationally costlier than the mechanical equilibrium models of Allaire et al. and Kapila et al. [139].
7. Abgrall 4-eqn.	- Very simple to use. - Can be used only for a limited scale.	- Effects such as viscosity, surface tension, thermal conductivity, and gravity can easily be included in the equation.

2.5 Choice of Equation of State EoS

To provide closure to the hyperbolic system of equations in the diffuse interface models, the thermodynamic properties of the compressible multiphase fluid are expressed as a function of the fluid's physical paramters, such as pressure, temperature, density, specific internal energy, and specific entropy.

Common EoS used for the numerical simulation of DIM with interest in liquid-gas flows or mixtures are the **Ideal gas, Stiffened Gas, NASG , Van der Waals and Tait EoS** (see Table 2.3). They are specified for each phase and used in addition to other closure systems close the equations of the DIM. The stiffened EoS is widely used in DIM models for compressible multicomponent flow to describe immiscible fluids such as mixtures of gases and liquids [72, 147, 31, 138, 29, 199, 59]. It allows for the modelling of physics such as the attractive and repulsive effects of a material at the molecular level, which explains its popularity in compressible multiphase flow [131]. A brief description of the EoS used for compressible multicomponent flows is provided in the interface capturing paradigm. This research uses the stiffened gas (SG) EoS. The stiffened gas equation is suitable for gases and liquids, while the Tait EoS is used for liquids such as water. The van der Waals EoS is computationally more expensive than the SG EoS for gas, as noted in the paper [76], where various EoS are considered and compared shows that the van der Waals EoS requires a significant number of time steps and CPU time to obtain the same solution as that of SG EoS. For fluids such as water, the Tait EoS and the SG EoS had similar computational times for the same result.

The advantage of the DIM is that it can be used different EoS for each phase, such as SG EoS for the gas phase and Tait's EoS for the liquid phase. This is necessary sometimes when more than a particular EoS is needed for both fluid phases.

2.5.1 Ideal Gas EoS

The ideal gas equation of state is very useful when one of the interacting fluids is an inert gas. The other fluid can be given other EoS such as SG EoS. The pressure of the fluid is simply expressed as:

$$p_i = (\gamma_i - 1)\rho_i e_i. \tag{2.59}$$

where γ_i is the adiabatic specific heat ratio for the gas in consideration.

2.5.2 Tait's EoS

Tait's EoS is also called the isentropic stiffened gas EoS. This is a relatively simple EoS used frequently in compressible multiphase flow for liquids such as water. In Tait's EoS, the thermodynamical variable of interest is the fluid's density. The pressure of a fluid is expressed as a thermodynamic function of only its density, $p = p(\rho)$. Various authors have used it for compressible multiphase [185, 190, 94, 76]. The Tait EoS estimates the low pressure more accurately than the Stiffened Gas EoS in cases where cavitation occurs in specific regions of the flow [94]. Tait's EoS is suitable for fluid pressures of up to 2000 MPa [94].

$$p_i = (\gamma - 1)\rho e - \gamma(\text{B-A}). \tag{2.60}$$

The constants A and B are γ are constants that are chosen based on the fluid in consideration. For water, $A = B = 3.31 \times 10^8$ Pa, $\gamma = 7.15$, $\rho_0 = 1000$ kg/m^3.

The speed of sound for the mixture is expressed below:

$$c = \sqrt{\frac{dp}{d\rho}} \tag{2.61}$$

2.5.3 Van der Waals gas EoS

The Van der Waals equation is appealing for computing pressure in compressible multiphase flow with phase transition, such as in boiling flows, and is presented below:

$$p = \frac{\gamma - 1}{1 - \rho b}(\rho e - \pi + a\rho^2) - (\pi + a_i\rho^2). \tag{2.62}$$

where the variable a represents a constant that characterizes the attractive forces between gas molecules, b represents the specific co-volume, i.e. the volume occupied by the molecules, π is the osmotic pressure. The values of these constants vary depending on the specific gas being considered and the conditions under which it exists.

2.5.4 Stiffened gas EoS

The SG EoS introduced by Harlow and Amsden [60]. is used to describe the thermodynamic properties of a liquid, gas and also solid. It is often used in simulations of compressible multiphase flow problems.

The EOS is typically expressed in the form of pressure for each phase or fluid and given as:

$$p_i = (\gamma_i - 1)\rho_i e_i - \gamma_i \pi_{\infty,i}, \tag{2.63}$$

For the mixture in general, the EoS is given below:

$$\xi = \frac{1}{\gamma - 1} = \sum_i \frac{\alpha_i}{\gamma_i - 1}, \tag{2.64}$$

$$\frac{\pi_\infty \gamma}{\gamma - 1} = \sum_i a_i \frac{\pi_{\infty,i}\gamma_i}{\gamma_i - 1}, \tag{2.65}$$

$$p = (\gamma - 1)\rho e - \gamma \pi_\infty. \tag{2.66}$$

2.5.5 Noble Abel Stiffened Gas' (NASG)EoS

Noble Abel Stiffened Gas' (NASG) is hybrid of the "Noble–Abel" and the "Stiffened Gas" equations of state. It has a lot of potential for compressible multiphase flows as it considers the thermal and compressibility effects of a fluid. Introduced by Le Métayer and Saurel, it has been used successfully in the DIM by several authors [89, 122, 194]. The NASG EoS relates the fluid's pressure as a function of the internal energy and the specific volume: $p = p(e,v)$. For more details on the NASG , see [89].

$$p_i(\rho_i, e_i) = (\gamma_i - 1)\frac{\rho_i(e_i - q_i)}{(1 - \rho_i b_i)} - \gamma_i \pi_{\infty i}, \tag{2.67}$$

where $(\gamma - 1)(e - q)$ represents thermal agitation and $1 - \rho_k b_k$ is the short distances repulsion.

2.5.6 Mie-Grüneisen EoS

The Mie-Grüneisen equation of state (EoS) is a very general form of EoS that is used to model compressible multiphase flow. It is incomplete because it is defined by a Grüneisen coefficient that is only a function of density and ignores temperature and entropy.

The general form of the Mie-Grüneisen equation of state (EoS) is :

$$p_i(\rho_i e_i) = \Gamma_i(\rho_i)[\rho_i e_i - \rho e_{ref}(\rho_i)] + p_{ref}(\rho_i). \tag{2.68}$$

where $p_{ref}(\rho)$, $e_{ref}(\rho)$ are the pressure and internal energy of reference state chosen along a p-V reference curve, $\Gamma(\rho, e)$ is the Grüneisen coefficient which is given as

$$\Gamma(\rho, e) = \frac{1\partial p}{\rho \partial e} \tag{2.69}$$

It is usually extended to complete EoS such as Ideal, Van der Waal, Tait, Stiffened, and NASG EoS. These EoS can expressed in the form Mie-Grüneisen EoS below.

$$\text{Ideal gas:} \begin{cases} \Gamma(\rho) = \gamma - 1 \\ p_{ref}(\rho) = 0 \\ e_{ref}(\rho) = 0 \end{cases} \tag{2.70}$$

$$\text{Tait:} \begin{cases} \Gamma(\rho) = \gamma - 1 \\ p_{ref}(\rho) = -\gamma(B - A) \\ e_{ref}(\rho) = 0 \end{cases} \tag{2.71}$$

$$\text{Stiffened gas:} \begin{cases} \Gamma(\rho) = \gamma - 1 \\ p_{ref}(\rho) = -\gamma_i \pi_i \\ e_{ref}(\rho) = 0 \end{cases} \tag{2.72}$$

$$\text{Van der Waals:} \begin{cases} \Gamma(\rho) = \frac{\gamma - 1}{1 - b\rho} \\ p_{ref}(\rho) = -a\rho^2 \\ e_{ref}(\rho) = -a\rho \end{cases} \tag{2.73}$$

$$\text{NASG:} \begin{cases} \Gamma(\rho) = \frac{\gamma - 1}{1 - b\rho} \\ p_{ref}(\rho) = -\gamma_i \pi_i \\ e_{ref}(\rho) = 0 \end{cases} \tag{2.74}$$

Table 2.3: Summarised overview of the EoS commonly used for compressible multiphase flow using the Diffuse interface models.

EoS	Used in	Equation
Ideal gas	[135]	$p_i = (\gamma_i - 1)\rho_i e_i$
Tait	[185, 190, 94, 76]	$p_i = (\gamma_i - 1)\rho_i e_i - \gamma(B - A)$
Van der Waals	[76, 155]	$p = \frac{\gamma-1}{1-\rho b}(\rho e - \pi + a\rho^2) - (\pi + a_i\rho^2)$
Stiffened Gas	[172, 2, 31, 59, 29, 199]	$p_i = (\gamma_i - 1)\rho_i e_i - \gamma_i \pi_{\infty,i}$
NASG	[155, 194, 89, 122, 195]	$p_i(\rho_i, e_i) = (\gamma_i - 1)\frac{\rho_i(e_i - q_i)}{(1-\rho_i b_i)} - \gamma_i \pi_{\infty i}$
Mie–Gruneisen	[119, 144, 188, 145]	$p_i(\rho_i e_i) = \Gamma_i(\rho_i)[\rho_i e_i - \rho e_{ref}(\rho_i)] + p_{ref}(\rho_i)$

2.6 High-order methods for DIM

It has been 10 years since the first ever international workshop (2012) on high-order schemes in CFD was held in Nashville, Tennessee, U.S.A. High-order schemes for the solution of hyperbolic conservation laws have become an active area of research among CFD researchers and are already a workhorse for compressible multiphase flow CFD. These flows are challenging to simulate due to the complex interactions between the fluids and the physical phenomena that occur at the interface between them. Because shock-waves and discontinuities occur frequently in compressible multiphase flow, computational methods need to be efficient enough to correctly resolve the interfaces such that the discretization can give a resolution smaller than the interface thickness while also avoiding excessive diffusion across such an interface. Schemes that can potentially achieve these requirements must be high-order accurate, especially in regions of the flow where the solution changes smoothly, and not near discontinuities such as shocks or interfaces between different fluids, suppress oscillations near discontinuities, and preserve numerical stability. The common argument against high-order schemes is that they are computationally

expensive, but this is not necessarily true. To achieve the same level of accuracy as a high-order method, a lower-order method typically needs to use a denser mesh or more computational elements, which in the long run makes it more computationally expensive. By mathematical definition, a numerical method is considered to be of order k (or the k^{th} order) if the error in the solution, denoted as $\mathcal{O}(\Delta t^k)$ for a time step Δt, decreases at a rate proportional to Δt^k. This means that for a higher-order method, the error decreases more rapidly with decreasing time step size, allowing for more accurate solutions with a smaller number of computational elements [183]. Following [24], this thesis refer to high-order methods as those that have an order of accuracy of at least three as determined by local truncation errors where the solution is smooth. High-order shock methods have been applied extensively in single-phase flow to capture these discontinuities, which can be in the form of shock-waves, contact waves, etc. In recent times, this has been extended to multiphase and multifluid flow [2, 172, 179]. However, when different fluids are present, very strong gradients are developed across material interfaces, which can result in oscillations at interfaces. This presents a challenging problem at the interface where oscillations exist, and how to correctly capture the discontinuities is very important. Most of the existing numerical methods used to suppress these oscillations are first- and second-order schemes with the Roe flux limiter solver and HLLC to upwind the fluxes. First- and second-order schemes are often the preferred choice, mostly because of their simplicity, robustness, and the fact that they give an output result, but their accuracy is often something to be concerned about. The major drawback of first- and second-order methods is the introduction of excessive dissipation and low resolution in smooth regions; these problems are tackled well by the high-order accurate methods. This section of the review will concentrate on the practicality of the various high-order methods, with less emphasis on the theoretical and mathematical foundations of the methods. The choice of a high-order method for compressible multiphase flow depends on the specific characteristics of the problem, such as the nature of the flow, the presence of shock-waves, and the desired level of accuracy. These methods can be computationally expensive, but

they can provide more accurate solutions that are essential for many engineering and scientific applications. The common high-order methods used for compressible multiphase simulations in the DIM framework are the Discontinuous Galerkin DG [50, 125] and ADER-DG methods [26] for finite elements , and in the finite-volume and finite-difference framework, Weighted essentially non-oscillatory (WENO) [31, 10, 73, 29], Central Weighted Essentially Non-Oscillatory (CWENO) [2, 172], a Multidimensional Optimal Order Detection (MOOD) [47] and the Monotone Upstream-centred Scheme for Conservation Law (MUSCL) [139, 143, 142, 148, 23, 3] with the use of limiters such BVD or TVD (Total Variation Diminishing). The use of finite difference Weighted Essentially Non-Oscillatory (WENO) schemes is limited to uniform meshes or smooth curvilinear coordinates in multidimensional computations. However, finite volume WENO schemes, although more computationally demanding and challenging to implement, provide a significant advantage in compressible multiphase flow.

While the discontinuous finite element method may be simpler to use with an unstructured or distorted mesh, WENO and other higher-order finite volume schemes are more robust in the presence of strong shocks and less computationally expensive. To ensure the proper directionality of the fluxes, the WENO method is often combined with an HLL or HLLC (Harten-Lax-van Leer Contact) approximate Riemann solver. In the diffuse interface finite-volume framework, one of the earliest applications of unstructured mesh to compressible multiphase flow was by Dumbser (2013) [40] for the seven-equation B-N models using WENO schemes. Tsoutsanis et al. [47] took a similar approach, employing Multidimensional Optimal Order Detection (MOOD) for the five-equation model on an unstructured mesh. Chiapolino et al.[25] and Pandare et al.[110] also used the MUSCL schemes with limiters for compressible two-phase flows on hybrid unstructured grids for the six-equation single pressure model. Price et al. [119], Faucher et al.[48], and Cheng et al. [23] have also expanded the DIM to unstructured meshes. Either by finite difference or finite volume techniques, an exact or approximate solution to the Riemann problem of DIM equations is needed as a reference solution to verify the accuracy of

our numerical methods [166]. Riemann problems resulting from the reconstruction of Diffuse Interface Models (DIM) are computationally expensive, as all exact solvers use iterative schemes. Some of the common Riemann approximate solvers used to tackle this are the Roe Solver [109], HLL solvers [62], Lax-Friedrichs solvers, and the HLLC solver [166]. Of all the solvers, HLLC, which is an extension of HLL that takes into account the different phase velocities and sound speeds, is the preferred solver, especially when computing problems where low densities and pressures are expected, which is found in some compressible multiphase flow. Although the Roe solvers are less dissipative, they are more computationally expensive and do not preserve the positivity of densities, energies, and volume fractions [45, 120, 44]. The exact Riemann solution to the DIM is complex to achieve [15, 84]. To reach a computational solution for the two-phase B-N seven-equation model, most authors focus only on the convective part of the system, ignoring the source terms. Tokareva and Toro [165] first proposed an HLLC-type approximate Riemann solver for a homogeneous Baer-Nunziato model with one-stage Newton iterations. Lochon et al. [96] proposed a new HLLC-type Riemann solver for the Baer-Nunziato model based on Tokareva and Toro's [165] HLLC-type. Hennessey et al. [63] improved upon the HLLC-type Riemann solver with the Mie–Grüneisen equations of state to consider reactive flow dynamics. Andrianov and Warnecke (2004) [9] presented an inverse procedure to construct exact solutions to the Riemann problem for the homogeneous B-N model. More recently, the exact solutions to the Riemann problem for the Romenski seven-equation model were presented by Ferdinand Thein (2022) [161]. Saurel introduced the exact Riemann solution to the six-equation model equations. Saurel-Abgrall (1999) first proposed a Godunov-type scheme with Riemann problem solver approximation in HLL for the six-equations model. The method was straightforward but too dissipative. Furfaro and Saurel [51] later developed the HLLC for the same six-equations model. For the five-equation mechanical equilibrium models, Coralic and Colonius [29] first used the HLLC to upwind the fluxes of the Allaire et al. [4] mechanical equilibrium model. Li et al. [91] built a 3-wave HLLC Riemann solver.

Tian and Toro [162] developed an HLLC-type Riemann solver for the five-equation model, a simplified version of Saurel and Abgrall's seven equations. Deledicque and Papalexandris [32] presented an exact Riemann solver for compressible two-phase flow models containing non-conservative products.

Although the discontinuous finite element method is easier to use with an unstructured or distorted mesh, WENO and other finite volume higher-order schemes on an unstructured mesh are more robust in the presence of strong shocks and cost less to compute. To upwind the fluxes, the WENO is frequently used in conjunction with an HLL or HLLC Harten-Lax-van Leer Contact HLLC approximate Riemann solver. There are several variants of WENO schemes in the diffuse interface method that have been developed to accurately simulate such complex flows to minimize numerical oscillations and provide high-order accuracy. Some of the variant of WENO includes WENO-Z, WENO-JS,WEN0-UP. The WENO-Z scheme for example combines the WENO scheme with a Zalesak limiter, that limits the fluxes across the interface to prevent overshoots and undershoots in the solution. Overall, these WENO schemes have shown promise in accurately simulating compressible multiphase flow and have been used to simulate a wide range of multiphase flow problems, including bubble dynamics, droplet collisions, and shock/bubble interactions.

The most prominent drawback of the DIM, as observed by many authors [136, 147, 138], is the introduction of artificial smearing at the interface. To counteract this diffusion effect, different approaches are used in conjunction with the high order methods, such as the MUSCL and Weighted Essentially Non-Oscillatory (WENO) schemes. These techniques are used to improve the accuracy and resolution of the interface between two phases in compressible multiphase flow simulations. The first approach developed by Kokh and Lagoutiere [82] is the **Anti-diffusion Interface Sharpening (ADIS) technique** commonly used with the WENO high-order methods as a post-processing step. To do this, an anti-diffusion (Eq. 2.75) with a positive diffusion coefficient is introduced into the volume-fraction after each time step to control interface sharpness [82, 34, 153]. See [82] for a more detailed description of this method.

$$\frac{\partial \alpha}{\partial t} = -\nabla \cdot (D \nabla \alpha) \tag{2.75}$$

where t is a pseudo time to evolve the anti-diffusion correction and $D > 0$ is an anti-diffusion coefficient.

The abbreviation "AD" will be employed to denote "anti-diffusion," specifically when dealing with variables or quantities obtained through the implementation of the anti-diffusion sharpening technique. Consequently, by applying regularization based on the minmod limiter, the new flux F_{AD}^{α} is calculated at the interface between two arbitrary cells, designated as i and j, using the limited cell-averaged gradient value $\alpha, (\nabla \alpha)_{lim}$ for the cells under consideration.

$$F_{AD}^{\alpha} = \begin{cases} -D\left((\overline{\nabla \alpha})_{\text{lim}}\right)_i \cdot \mathbf{S}_{ij} & \text{if} \quad \left|\left((\overline{\nabla \alpha})_{\text{lim}}\right)_i\right| \leqslant \left|\left((\overline{\nabla \alpha})_{\text{lim}}\right)_j\right|, \\ -D\left((\overline{\nabla \alpha})_{\text{lim}}\right)_n \cdot \mathbf{S}_{ij} & \text{if} \quad \left|\left((\overline{\nabla \alpha})_{\text{lim}}\right)_j\right| < \left|\left((\overline{\nabla \alpha})_{\text{lim}}\right)_i\right|, \end{cases} \tag{2.76}$$

The vector $\mathbf{S}_{ij}$ represents the surface area of the face between the cells i and j.

Using the obtained F_{AD}^{α}, the R.H.S of Eq. 2.75 is expressed as:

$$\overline{\nabla \cdot (-D(\nabla \alpha))} = \frac{\sum_{cf}\left(F_{AD}^{\alpha}\right)}{V}, \tag{2.77}$$

where $\sum_{cf}$ denotes the summation over all cell faces and V is the cell volume. The volume fraction is advanced in pseudo time by an explicit Euler scheme:

$$\alpha^{n+1} = \alpha^{n} + \overline{\nabla \cdot (-D\,(\nabla \alpha^{n}))} \Delta t \tag{2.78}$$

with N being the pseudo time index, and the time step limit on pseudo time,

$$\Delta t = \frac{1}{4}\frac{(\Delta x_{\min})^2}{D}, \tag{2.79}$$

where $\Delta x_{\min}$ is the minimum cell width.

In the MUSCL schemes, a hybrid-scheme is also developed to reduce numerical smearing or oscillations at the interface , this second method are referred to as the **THINC (Tangent of Hyperbola for Interface Capturing)** interface sharpening technique introduced by Shyue and Xiao [148, 34]. The interpolation of the volume fraction is done as a pre-processing step using THINC interface sharpening techniques, while the other variables are maintained with the MUSCL interpolations [158, 147, 93, 111]. Only the MUSCL schemes are better suited for this approach. A parameter β in the hyperbolic tangent function controls interface sharpness. This MUSCL-hybrid method has been applied successfully to the Allaire et al. five-equation mechanical equilibrium model [147]. When the cell under consideration is in the mixture zone of the interface, a nonlinear reconstruction is performed for the linear cell interpolation, and the volume fraction is calculated using a hyperbolic tangent function in the manner shown below for one-dimension across a cell i :

$$\alpha(x) = 0.5\left\{1 + \sigma_i \tanh\left[\beta\left(\frac{x - x_{i-1/2}}{\Delta x}\right) - \tilde{x}_o\right]\right\}, \tag{2.80}$$

where σ_i is the sign function of the volume fraction, Δx_i is the grid resolution, β is a flexible user's parameter to vary the thickness and slope, $\beta \approx 2 - 3.5$.

The interface position is determined below as:

$$\tilde{x}_o = \frac{1}{2\beta}\ln\left[\frac{-1 + \exp\left(\beta\left(1 + \sigma_i - 2\bar{\alpha}_i\right)/\sigma_i\right)}{1 - \exp\left(\beta\left(1 - \sigma_i - 2\bar{\alpha}_i\right)/\sigma_i\right)}\right] \tag{2.81}$$

where $\bar{\alpha}_i$ is given as

$$\bar{\alpha}_i = \frac{1}{\Delta x_i} \int_{x_{i-1/2}}^{x_{i+1/2}} \alpha_i(x) dx. \tag{2.82}$$

The third approach to interface sharpening is to apply a limiter function to the conventional MUSCL schemes, which restricts the steepness of the concentration gradient in regions where the interface is diffuse. This is carried out through a volume fraction gradient limitation. This ensures that the interface remains sharp and well-defined even in regions where the scalar variable has a small gradient. The limiter function can be based on a variety of criteria, such as the distance between the cell center and the interface, the local curvature of the interface, or the local density or pressure gradient. Chiapolino et al. (2017) [25] developed a new variant of **the TVD limiter technique** that is specifically tailored for use on unstructured grids in simulations of compressible multiphase flow for the five-equation Kapila et al. models. In the total variation diminishing limiter technique for compressible multiphase flow, the interface sharpening limiters "Superbee", "Overbee", and "Ultrabee" can be utilised. However, it has been demonstrated that the "Overbee" limiter is more accurate near sharp gradients and interfaces, which may result in better accuracy in some circumstances [136].

As presented in the paper of Harten (1983) [62], the TVD measures oscillations for any solution Q at time step n with a total variation (TV) defined by,

$$TV(Q^n) = \sum_{i=-\infty}^{\infty} |Q_i^n - Q_{i-1}^n|, \tag{2.83}$$

which must satisfy the condition for the Total Variation Diminishing (TVD) with time, as given below:

$$TV(Q^{n+1}) \leq TV(Q^n). \tag{2.84}$$

In [25], the slope limiter α_{ij} is given as:

$$\alpha_{ij} = \begin{cases} \frac{Q^{\max} - Q_i}{2\left(Q_{ij}^{nlim} - Q_i\right)} & \text{if } \left(Q_{ij}^{n\lim} - Q_i\right) > 0, \\ \frac{Q^{\min} - Q_i}{2\left(Q_{ij}^{nlim} - Q_i\right)} & \text{if } \left(Q_{ij}^{n\lim} - Q_i\right) < 0, \\ 1 & \text{if } \left(Q_{ij}^{nlim} - Q_i\right) = 0, \end{cases} \tag{2.85}$$

$Q^{\max}$ and $Q^{\min}$ are the maximum and minimum value of the state variables, $Q_{ij}^{nlim} = Q_i + \vec{r}_{ij}.\nabla Q_i$ is the reconstructed solution of the considered cell i and all of its neighbouring cells. The limiter function is expressed as:

$$\theta\left(\alpha_{ij}\right) = \max\left[0, \min\left(\beta\alpha_{ij}, 1\right), \min\left(\alpha_{ij}, \beta\right)\right], \tag{2.86}$$

Another approach to reducing the artificial smearing at the interface is **the interface compression technique**. In this approach, the interface is represented by a Following the technique used by Olsson and Kreiss (2005) [46] specifically for incompressible flow using the level set method, Shukla et al. (2010) [143] proposed a modification of the original Olsson et al. (2007) [106] technique for compressible flows for diffuse interface models . The Shukla et al. (2010) technique has since been extended to the Kapila model, which is a widely used model for simulating compressible two-phase flow. The extension was proposed by Tiwari et al. [164], in which the advection equation in the five-equation of Kapila (Eq.2.24)is expressed as:

$$\frac{\partial \alpha}{\partial t} + \mathbf{u} \cdot \nabla \alpha = \mathscr{U}_o \mathbf{n} \cdot \nabla \left[\varepsilon_b |\nabla \alpha| - \alpha(1-\alpha)\right], \tag{2.87}$$

where $(\varepsilon_b|\nabla\alpha|)$ is the interface balance function and $(\alpha(1-\alpha))$ is the diffusion function are used to maintain the interface thickness. The symbol ε_b denotes the thickness of the interface, which is chosen independently and chosen to be greater than the minimum grid size Δx_{min}. The symbol $\mathscr{U}_o$ represents the characteristic regularization rate, and the

symbol **n** represents the interface normal vector, which can be expressed as:

$$\mathbf{n} = \nabla\alpha / |\nabla\alpha|, \tag{2.88}$$

and α is determined as a function x by:

$$\alpha(x) = 0.5\left[1 + \tanh\left(\frac{s(x)}{2\varepsilon_b}\right)\right]. \tag{2.89}$$

where $s(x)$ is the normal coordinate to the interface.

Very active research is ongoing on how to improve these methods described above and the choice of technique depends on the suitability to the compressible multiphase flow simulation being studied. A comparative analysis, if carried out, would be helpful for comprehending the advantages and disadvantages of various interface sharpening techniques, which may identify the best outcomes under various conditions. The table below present the various techniques or methods of minimizing numerical smearing for compressible multiphase flow discussed above and their application in different diffuse interface models as seen in published literature.

Table 2.4: Summarised overview of the methods used to minimize numerical smearing for compressible multiphase flow using the Diffuse interface models. U: Used; NYU: Not Yet Used (to the author's best knowledge).

Methods	5-eqn. DIM	6-eqn. DIM	7-eqn. DIM
Anti-diffusion	U[82, 147]	U[82, 153]	NYU
THINC	U[76, 155, 203, 158, 100]	U[93]	NYU
Limiter technique e.g TVD, BVD	U [25, 99, 199]	NYU	NYU
Interface Compression	U[103, 157, 143, 142]	NYU	NYU

Dumbser et al. (2017) [41] introduced the Compact WENO (CWENO) scheme, a variant of the high-order Weighted Essentially Non-Oscillatory (WENO) scheme, for the Baer-Nunziato homogeneous model on unstructured meshes. When compared to traditional WENO schemes, it uses only one set of valid nonlinear weights and one set of valid linear weights for each point in a cell. This reduces the size of directional stencils, making the approximation less complicated and less computationally expensive. These features make CWENO more suitable for deployment in frameworks such as DG [204]. One of the overlooked benefits of CWENO is its robustness since the smaller directional stencils increase the probability of at least one stencil lying in a region with a smooth variation of data. The CWENO scheme's high accuracy, reduced computational cost as compared to other high-order methods such as WENO, and ability to handle complex geometries on an unstructured grid make it the preferred choice for simulating high-fidelity multiphase flows. In the following chapter, the CWENO reconstruction process is described for the mechanical equilibrium five-equation model proposed by Allaire et al. and Kapila et al. (2001), using the HLLC approximate solver for flux approximation and the 3rd-order Runge-Kutta method for temporal integration.

Chapter 3

Numerical framework

3.1 Finite-volume formulation for the five-equation Models

Consider a three-dimensional flow domain Ω, which is composed of conforming cells of different shapes, including tetrahedral, hexahedral, prism, and pyramid cells. Each cell has a unique index represented by a mono-index i. Integrating the five-equation model over the domain of interest with boundary $\partial\Omega$, the equations that govern the behavior of the fluid in this region are expressed as follows in vector form:

$$\frac{\partial}{\partial t}\int_{\Omega_i}\mathbf{Q}\,d\Omega+\int_{\Omega_i}(\nabla\cdot\mathbf{F}(Q))\,d\Omega=\int_{\Omega_i}\mathbf{H}\,d\Omega \tag{3.1}$$

where the vectors **Q**, **F** and **H** are given by:

$$Q=\begin{bmatrix}\alpha_1\\ \alpha_1\rho_1\\ \alpha_2\rho_2\\ \rho\mathbf{u}\\ \rho E\end{bmatrix},\quad F=\begin{bmatrix}\alpha_1\mathbf{u}\\ \alpha_1\rho_1\mathbf{u}\\ \alpha_2\rho_2\mathbf{u}\\ \rho\mathbf{u}^2+p\\ \mathbf{u}(\rho E+P)\end{bmatrix},\ H_{Allaire}=\begin{bmatrix}-\alpha_1\\ 0\\ 0\\ 0\\ 0\end{bmatrix};H_{Kapila}=\begin{bmatrix}-\alpha_1-\mathbf{K}\\ 0\\ 0\\ 0\\ 0\end{bmatrix}. \tag{3.2}$$

By applying the Gauss divergence theorem, the flux term is transformed from a surface integral into a volume integral as follows:

$$\int_{\Omega_i} (\nabla \cdot \mathbf{F}(Q))\, d\Omega = \int_{\Omega_i} \mathbf{F}(Q) \cdot \mathbf{n}\, dS \tag{3.3}$$

Then Eq. 3.1 becomes:

$$\frac{\partial}{\partial t} \int_{\Omega_i} \mathbf{Q}\, d\Omega + \int_{\Omega_i} \mathbf{F}(Q) \cdot \mathbf{n}\, dS = \int_{\Omega_i} \mathbf{H}\, d\Omega \tag{3.4}$$

If the domain $\partial\Omega$ is partitioned into smaller elements or voxels (V_i) with individual volumes $(|V_i|)$, for $(i = 1, \ldots, N)$, then the left-hand side of Eq. 3.4 can now be written as follows:

$$\frac{d\mathbf{Q}_i}{dt}|V_i| + \int_{\partial V_i} \mathbf{F}(Q) \cdot \mathbf{n}\, dS = \frac{d\mathbf{Q}_i}{dt}|V_i| + \sum_{f \in \partial V_i} \mathbf{F}_f(Q)|f|, \tag{3.5}$$

where $\mathbf{Q}_i$ is the volume-averaged vector of the state variables, and $\mathbf{F}_f$ is the normal-averaged flux, defined as:

$$\mathbf{Q}_i = \frac{\int_{V_i} \mathbf{Q}\, dV}{|V_i|}, \quad \mathbf{F}_f = \frac{\int_f \mathbf{F}(Q) \cdot \mathbf{n}\, dS}{|f|}. \tag{3.6}$$

.

The normal-averaged flux $\mathbf{F}_f$ of the face integral is calculated using a suitable Gauss-Legendre quadrature and presented below:

$$F_f = \sum_{\alpha=1}^{N_{qp}} \omega_\alpha F(U(x_{f,\alpha})) \cdot N_f. \tag{3.7}$$

N_f represents the number of faces per element, and N_{qp} is the number of quadrature points used for approximating the surface integrals. The high-order approximations of the solutions for cells i and j are denoted as $\mathbf{Q}^L(\mathbf{x}_{f,\alpha}, t)$ and $\mathbf{Q}^R(\mathbf{x}_{f,\alpha}, t)$, respectively, where α represents different Gaussian integration points $\mathbf{x}_\alpha$ and weights ω_α over each face. The volume-averaged volume fraction of cell i at time level n is given by $\alpha_{i,1}^n$ (See Figure 3.1).

The numerical flux $\mathbf{F}(\mathbf{Q}(\mathbf{x}_{f,\alpha}))$ is computed by an approximate Riemann solver using

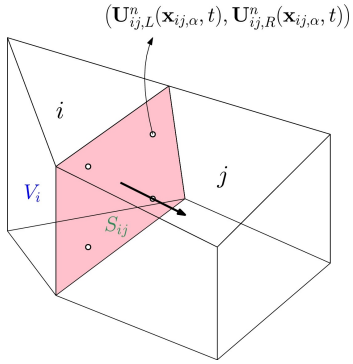

Figure 3.1: Schematic illustrating the direction normal to the cell interface between the two cells i and j under consideration. (Reproduced from [14]).

the left (L) and right (R) states of the high-order approximations of the solutions at the cell interfaces i and j, respectively. The expression for this is:

$$\mathbf{F}(\mathbf{Q}(\mathbf{x}_{f,\alpha})) \approx \mathbf{F}(\mathbf{Q}^L(\mathbf{x}_{f,\alpha}),\mathbf{Q}^R(\mathbf{x}_{f,\alpha})). \tag{3.8}$$

Substituting Eq.3.8 into Eq.3.7

$$Q_i^{n+1} = Q_i^n - \Delta t \frac{1}{|V_i|} \sum_{j=1}^{N_f} \sum_{\alpha=1}^{N_{qp}} F\left(\left(\mathbf{Q}^L(\mathbf{x}_{f,\alpha}),\mathbf{Q}^R(\mathbf{x}_{f,\alpha}) - \mathbf{a}^n_{i,1} \cdot u^{Riem}_n\left(\mathbf{x}_{f,\alpha}\right)\right)\omega_\alpha |f\right) \tag{3.9}$$

The source term $\mathbf{H}$ corresponds to $\alpha_1 \nabla \cdot \mathbf{u}$ in the Allaire equation (2.45), and $(\alpha_1 + K)\nabla \cdot \mathbf{u}$ in the Kapila five-equation model. To approximate the source term numerically, the approach proposed by Johnsen and Colonius [73] is used, where a surface integral is computed instead of a volume integral, and the same velocity estimate gotten from the approximate Riemann solver is used as that for evaluating the fluxes as shown below:

$$\overset{Allaire}{\int_{\Omega_i}} \alpha_1 \nabla \cdot \mathbf{u}\, d\Omega \approx \alpha_1\, d\Omega \cdot \int_{\partial\Omega_i} (\mathbf{u}^{Riem.} \cdot \mathbf{n})\, dS. \tag{3.10}$$

$$\overset{Kapila}{\int_{\Omega_i}} (\alpha_1 + K)\nabla \cdot \mathbf{u}\, d\Omega \approx (\alpha_1 + K)\, d\Omega \cdot \int_{\partial\Omega_i} (\mathbf{u}^{Riem.} \cdot \mathbf{n})\, dS. \tag{3.11}$$

where n is defined as the cell unit normal.

3.2 Spatial discretisation

In this section, we present a reconstruction procedure designed for mixed-element unstructured meshes in three-dimensional space. This procedure will be employed later in the development of the CWENO method. Applying this reconstruction procedure to a scalar variable $u(x,y,z)$, the spatial computational domain is discretized into conforming elements V_i, each with a volume denoted as $|V_i|$, and these elements are uniquely indexed by a mono-index, i as mentioned earlier in the previous section 3.1. The center of each element is defined by coordinates (x_i, y_i, z_i). The focus of the reconstruction procedure is to construct a high-order polynomial, $p_i(x,y,z)$, in such a way that it has the same average value as Q within the target cell V_i.

$$\mathbf{Q}_i = \frac{1}{|V_i|}\int_{V_i} \mathbf{Q}(x,y,z) = \frac{1}{|V_i|}\int_{V_i} \mathbf{p}_i(x,y,z)\, dV. \tag{3.12}$$

The `ucns3d` open-source CFD code utilizes a variable reconstruction process, based on the techniques developed by Tsoutsanis et al. [173, 177, 172] and Titarev et al. [163], for solving smooth and discontinuous flow problems. These techniques have been previously applied in various studies on flow problems, such as turbulence modelling for iLES, rotational bodies etc.[170, 152, 150, 16, 151, 175, 12, 11, 13, 83, 178, 163, 156, 176, 174, 47, 177, 172, 14, 180].

To perform the reconstruction, a method introduced by Dumbser et al. [39, 42] is used to transform the data from physical space to a reference space, which reduces scaling effects that occur when dealing with unstructured meshes made up of elements of varying shapes and sizes. In particular, the decomposition strategy described in [180, 173] is employed, where each element is decomposed into triangular (2D) or tetrahedral (3D) elements and one of the decomposed elements is used as the reference element for the coordinate system transformation.

Consider a 3D general element with vertices $\mathbf{vx}_{ij}$, where $j = 1,2,\ldots J_i$. If the element is non-tetrahedral, it is segmented into tetrahedrals, and one of the tetrahedrals is chosen

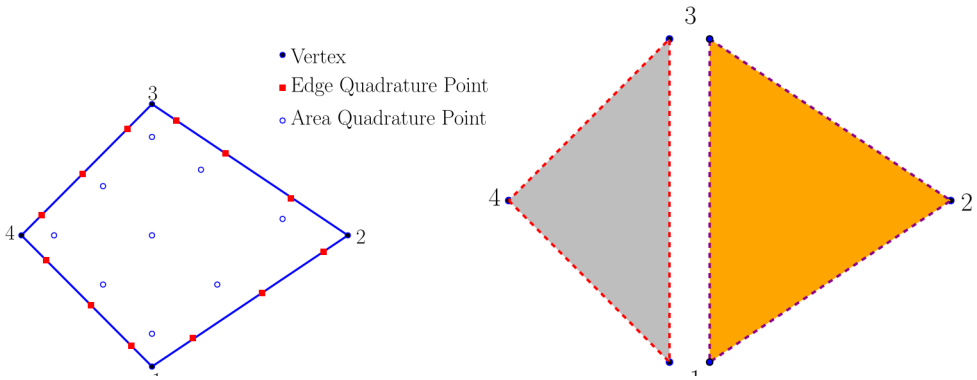

Figure 3.2: Schematic of a quadrilateral cell that has been segmented into triangles for the purpose of transforming it into reference space. (a) Quadrilateral cell (b) Decomposition into two triangles in a reference space. (Adapted from [168]).

with vertices $\mathbf{w}_1 = (x_1, y_1, z_1)$, $\mathbf{w}_2 = (x_2, y_2, z_2)$, $\mathbf{w}_3 = (x_3, y_3, z_3)$, and $\mathbf{w}_4 = (x_4, y_4, z_4)$. The transformation from the Cartesian coordinates (x, y, z) to a reference space (ξ, η, ζ) is given by the following equations:

$$\begin{pmatrix} x \\ y \\ z \end{pmatrix} = \begin{pmatrix} x_1 \\ y_1 \\ z_1 \end{pmatrix} + J \cdot \begin{pmatrix} \xi \\ \eta \\ \zeta \end{pmatrix}, \tag{3.13}$$

with the Jacobian matrix given by:

$$J = \begin{bmatrix} x_2 - x_1 & x_3 - x_1 & x_4 - x_1 \\ y_2 - y_1 & y_3 - y_1 & y_4 - y_1 \\ z_2 - z_1 & z_3 - z_1 & z_4 - z_1 \end{bmatrix}. \tag{3.14}$$

The transformation of an element V_i to an element V_i' in the reference coordinate system can be achieved through an inverse mapping represented by the equation below.

$$\mathbf{vx}'_{ij} = J^{-1} \cdot \left(\mathbf{vx}_{ij} - \mathbf{w}_1\right), \quad j = 1, 2, \ldots J_i. \tag{3.15}$$

The transformation does not alter the spatial average of the conserved variable $\mathbf{Q}_i$.

$$\mathbf{Q}_i = \frac{1}{|V_i|}\int_{V_i} \mathbf{Q}(x,y,z)\, dV \equiv \frac{1}{|V_i'|}\int_{V_i'} \mathbf{Q}(\xi,\eta,\zeta)\, d\xi d\eta d\zeta. \tag{3.16}$$

The process of creating the reconstruction polynomial involves using a central stencil $\mathscr{S}^1$ that includes $M+1$ cells, with one of the cells being the considered cell i, and the remaining cells are added recursively. To achieve a higher degree of robustness in regions of poor quality meshing, the stencil-based compact (SBC) algorithm described in [171] is used. The SBC algorithm is known for its affordability in terms of computation and improved robustness, and in this study, $M = 2K$ is set to enhance its robustness, as reported in several previous studies [171, 105, 35]. Here, K refers to the total number of polynomial coefficients used.

$$K(r,d) = \frac{1}{d!}\prod_{l=1}^{d}(r+l)\,, \tag{3.17}$$

The value of d corresponds to the space dimensions, which is within the range of 2 to 3. The central stencil $\mathscr{S}^1$ is defined as:

$$\mathscr{S}_i^c = \bigcup_{m=0}^{M_c} \Omega_m, \tag{3.18}$$

where m is the numbering (locally) of the stencils element and starts from the first cell with the numbering 0. In the reconstruction process, a central stencil $\mathscr{S}^1$ is used, which includes the considered cell i and M neighbouring cells, forming a total of $M+1$ cells.

$$p(\xi,\eta,\zeta) = \sum_{k=0}^{K} a_k \phi_k(\xi,\eta,\zeta) = \mathbf{Q}_0 + \sum_{k=1}^{K} a_k \phi_k(\xi,\eta,\zeta), \tag{3.19}$$

The vector $\mathbf{Q}_0$ represents the conserved variables at cell i, while a_k refers to the degrees of freedom of the polynomial. The degrees of freedom for each cell m are calculated in such a way that the cell average of the reconstruction polynomial $p(\xi,\eta,\zeta)$ matches the

cell average of the solution $\mathbf{Q}_m$.

$$\int_{V'_m} p(\xi,\eta,\zeta)\,d\xi d\eta d\zeta = |\Omega'_m|\mathbf{Q}_0 + \sum_{k=1}^{K} \int_{\Omega'_m} a_k \phi_k\, d\xi d\eta d\zeta = |V'_m|\mathbf{Q}_m, \quad m = 1,\ldots,M. \tag{3.20}$$

Equation (3.12) must also be satisfied by the basis functions ψ_k for hexahedrons, prisms, and pyramids, as it is not always feasible to convert their elements to a unit cell. The definition of the basis functions ψ_k utilized for all stencil elements is as follows:

$$\phi_k(\xi,\eta,\zeta) \equiv \psi_k(\xi,\eta,\zeta) - \frac{1}{|\Omega'_0|}\int_{V'_0} \psi_k\, d\xi d\eta d\zeta \quad k = 1,2,\ldots,K, \tag{3.21}$$

For this investigation, Legendre polynomials are used as the basis functions, denoted by ψ_k, for all of the elements within the stencil. The equations for determining the integrals of basis function k over stencil cell m, denoted as A_{mk}, and the right-hand side vector b, are as follows:

$$A_{mk} = \int_{V'_m} \phi_k\, d\xi d\eta d\zeta, \quad b_m = |V'_m|(\mathbf{Q}_m - \mathbf{Q}_0),$$

The equations that relate to the degrees of freedom a_k can be restated in the form of a matrix.

$$\sum_{k=1}^{K} A_{mk} a_k = b_m, \quad m = 1,2,\ldots M. \tag{3.22}$$

The system of linear equations obtained from the previous step is solved using a QR decomposition method based on Householder transformation. To solve this system, the Moore-Penrose pseudo-inverse of A_{mk} is used, which is computed only once at the beginning of the simulation, as described in [171].

3.3 CWENO Scheme

The Central WENO (CWENO) scheme, which is an improvement over the WENO scheme, uses a central stencil to compute numerical fluxes, resulting in increased accuracy and efficiency. To achieve high-order accuracy in smooth regions of the solution while maintaining stability and accuracy in regions of high gradients and shocks, the CWENO scheme combines the WENO scheme with a central scheme. In this research, the CWENO scheme utilized follows the approach proposed by Tsoutsanis and Dumbser [177]. This approach involves constructing an optimal polynomial p_{opt} using a central stencil and lower-order polynomials using directional stencils. The optimal polynomial provides high-order accuracy when the solution varies smoothly, while the lower-order polynomials minimize oscillations in the solution when dealing with discontinuous data. All polynomials are obtained through constrained least-squares technique, ensuring they match the cell averages of the solution. The directional stencils follow the Type3 definition, which includes one directional stencil per element face, as explained by Tsoutsanis [171]. The optimal polynomial is defined as:

$$p_{opt}(\xi,\eta,\zeta) = \sum_{s=1}^{s_t} \lambda_s p_s(\xi,\eta,\zeta), \tag{3.23}$$

The central stencil has an index of 1, while the directional stencils have indexes of $2,3$, and so on, with s_t being the total number of stencils. The linear coefficients, λ_s, correspond to each stencil and their sum is equal to 1. The optimum polynomial, $p_{opt}(\xi,\eta,\zeta)$, is calculated by subtracting the lower-order polynomials from the p_1 polynomial:

$$p_1(\xi,\eta,\zeta) = \frac{1}{\lambda_1}\left(p_{opt}(\xi,\eta,\zeta) - \sum_{s=2}^{s_t} \lambda_s p_s(\xi,\eta,\zeta)\right). \tag{3.24}$$

The CWENO reconstruction polynomial is a combination of all the polynomials, where the weight assigned to each polynomial is non-linear and given below:

$$p(\xi,\eta,\zeta)^{\text{cweno}} = \sum_{s=1}^{s_t} \omega_s p_s(\xi,\eta,\zeta), \tag{3.25}$$

The weight is denoted by ω_s and is assigned to each polynomial, and it depends on the smoothness of the data in the region. In regions with smooth data, the weight is approximately equal to the linear coefficient, λ_s, which gives a high-order approximation. On the other hand, regions that have discontinuous solutions are primarily impacted by the lower-degree polynomials of the directional stencils when it comes to the reconstructed solution. The reconstructed degrees of freedom are represented by $\tilde{a}_k$, and the non-linear weight ω_s is determined according to a specific definition below:

$$\omega_s = \frac{\tilde{\omega}_s}{\sum_{s=1}^{s_t} \tilde{\omega}_s} \quad \text{where} \quad \tilde{\omega}_s = \frac{\lambda_m}{(\varepsilon + \mathscr{SI}_s)^b}. \tag{3.26}$$

The smoothness indicator $\mathscr{SI}_m$ is given by:

$$\mathscr{SI}_s = \sum_{1\le|\beta|\le r} \int_{V_0'} \left(\mathscr{D}^\beta p_s(\xi,\eta,\zeta)\right)^2 (d\xi, d\eta, d\zeta), \tag{3.27}$$

The equation includes multiple variables: β represents a set of indices, r represents the order of the polynomial, and λ_m represents the linear weight. The value of ε is set to 10^{-6} to prevent division by zero. The derivative operator is denoted by $\mathscr{D}$ and b is a constant with a value of 4. The smoothness indicator can be expressed as a quadratic function of the degrees of freedom (a_k^s). Equation (3.27) can be reformulated as:

$$\mathscr{SI}_s = \sum_{k=1}^{K} a_k^s \left(\sum_{q=1}^{K} \mathscr{O}\mathscr{I}_{kq} a_q^s \right), \tag{3.28}$$

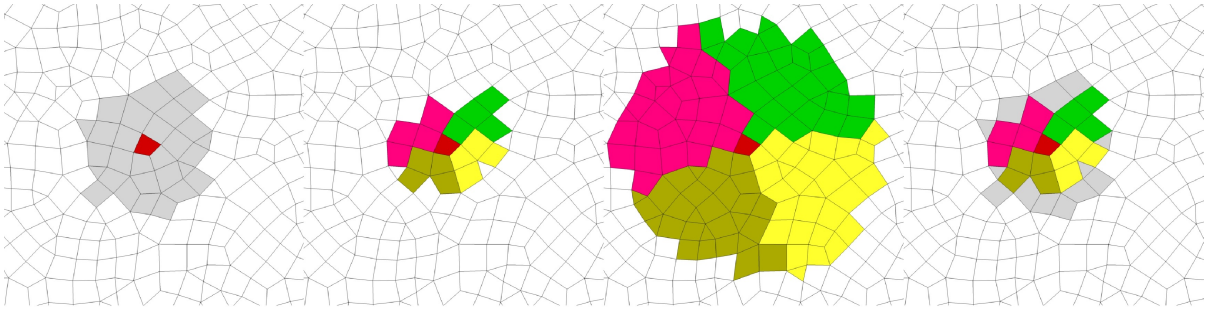

(a) Central Stencil (b) CWENO/CWENOZ directional stencils (c) WENO directional stencils (d) CWENO/CWENOZ stencils

Figure 3.3: The figure shows the stencils used in WENO and CWENO/CWENOZ schemes for P=4, where the red cell represents the cell of interest, and the main portion of the stencil is shown in grey, while the directional stencils are in different colors. It is observed that the directional stencils used in CWENO/Z schemes are smaller than those used in WENO schemes. For more information on interpreting the colors in the figure, please refer to the web version of the article. (Adapted from [14]).

where the oscillation indication matrix $\mathscr{OI}_{kq}$ is given by:

$$\mathscr{OI}_{kq} = \sum_{1\leq|\beta|\leq r} \int_{V_0'} \left(\mathscr{D}^{\beta}\phi_k(\xi,\eta,\zeta)\right)\left(\mathscr{D}^{\beta}\phi_q(\xi,\eta,\zeta)\right)(d\xi,d\eta,d\zeta), \tag{3.29}$$

The values can be calculated in advance and saved at the start of the simulation. The 2nd-order accuracy for the directional stencils is obtained using $r = 1$ and their associated polynomials, while the polynomial associated with the central stencil can have any order of accuracy. The linear weights are determined by assigning an arbitrary non-normalized linear weight $\lambda_1^{'}$ to the central stencil and then normalizing it using the following formula:

$$\lambda_1 = 1 - \frac{1}{\lambda_1^{'}}, \tag{3.30}$$

The linear weights related to polynomials of lower-order are identical and can be obtained from the given expression:

$$\lambda_s = \frac{1-\lambda_1}{s_t - 1}, \tag{3.31}$$

The number of stencils employed in the scheme is denoted by s_t, and a numerical value indicating the scheme's order will be added to its name, such as CWENO3 or WENO4. These labels represent a 3rd-order CWENO scheme and a 4th-order WENO scheme, respectively.

3.4 The Riemann Problem for the Five-equation DIM

The Riemann problem is an initial value problem (IVP) that involves finding solutions for hyperbolic partial differential equations, such as the five-equation diffuse interface model. The problem is characterized by having piecewise constant initial conditions, except for a single discontinuity located at a specific point, denoted as x_0.

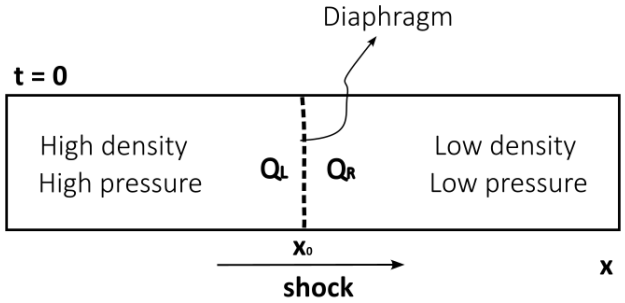

Figure 3.4: One-dimensional Riemann problem profile of a fluid on the (x,t) plane.

Consider a scenario involving a tube filled with a fluid (see Fig: 3.4). The two-phase fluid is characterized by two distinct initial states referred to as the "left" and "right" states. These states are defined by prescribed state variables such as volume fraction, pressure, density, and velocity. A diaphragm acts as a separator between these two states, positioned precisely at $x = 0$ and $t = 0$. The previously isolated "left" and "right" states interact when the diaphragm is suddenly removed (see Fig. 3.5).

The initial conditions are defined as:

$$\mathbf{Q}(x,0) = \begin{cases} \mathbf{Q}_L, & x \leq 0, \\ \mathbf{Q}_R, & x \geq 0, \end{cases} \tag{3.32}$$

Here, $\mathbf{Q}_L$ and $\mathbf{Q}_R$ represent the left and right states, respectively. These initial states establish the starting point for the Riemann problem, taking into account the discontinuity at x_0.

Solving the Riemann problem entails finding the intermediate state denoted as "*" (Fig.3.5) and the wave structure that forms between the left and right states, typically involving shock waves, rarefaction waves, and contact discontinuities.

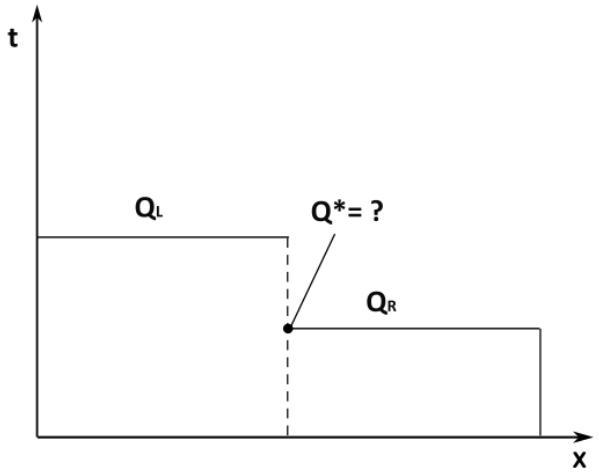

Figure 3.5: Schematic diagram of a discontinuous initial data with compressive characteristics on the (x,t) plane. The star region (*) represents the intermediate state.

To develop the Riemann problem for the 5-equation diffuse interface models of Kapila et al. and Allaire et al., it is simpler to present the conservative variables $\mathbf{Q} = (\alpha_1,\ \alpha_1\rho_1,\ \alpha_2\rho_2,\ \rho\mathbf{u}, \rho E,)^T$ in primitive "entropic" variables W= $(Y_1, s_1, s_2, \mathbf{u}, p)^T$ where the mass fraction $Y_i = \alpha_i\rho_i/\rho$ [102]. The new modification of the Eq. 2.22 is presented below in terms of phasic specific entropy in one dimension, see [102] for a details of this approach:

$$\frac{Ds_1}{Dt} = 0, \tag{3.33}$$

$$\frac{Ds_2}{Dt} = 0, \tag{3.34}$$

$$\frac{Du}{Dt} + \frac{1}{\rho}\nabla p = 0, \tag{3.35}$$

$$\frac{Dp_1}{Dt} + \rho c^2 \nabla \cdot u = 0, \tag{3.36}$$

$$\frac{DY_2}{Dt} = 0, \tag{3.37}$$

where ρ is the mixture density and c is the mixture speed of sound as defined in Eq. 2.28.

The five-equation diffuse interface models can now be expressed in a quasi-linear

form given below:

$$\frac{\partial \mathbf{W}}{\partial t} + A(\mathbf{W})\frac{\partial \mathbf{W}}{\partial x} = 0 \tag{3.38}$$

where $\mathbf{W}$ is the vector of conserved quantities, $\mathbf{A}(\mathbf{W})$ is the Jacobians matrix of the fluxes,

$$\mathbf{W} = \begin{bmatrix} s_1 \\ s_2 \\ u \\ p \\ Y_1 \end{bmatrix} \tag{3.39}$$

$$\mathbf{A}(\mathbf{W}) = \begin{bmatrix} u & 0 & 0 & 0 & 0 \\ 0 & u & 0 & 0 & 0 \\ 0 & 0 & u & \frac{1}{\rho} & 0 \\ 0 & 0 & \rho c^2 & u & 0 \\ 0 & 0 & 0 & 0 & u \end{bmatrix}. \tag{3.40}$$

From matrix A(W), the equation for the eigenvalues is given as:

$$\det[A(W) - \lambda I] = 0$$

and the characteristics of the jacobian A takes the form $(u-\lambda)^3((u-\lambda)^2 - c^2) = 0$ from which three (3) wave speeds with eigenvalues:

$$\lambda_1 = u - c, \quad \lambda_{2,3,4} = u, \quad \lambda_5 = u + c, \tag{3.41}$$

where c is the speed of sound for the mixture, which for the Kapila et al. five-equation is :

$$\frac{1}{\rho c^2} = \frac{\alpha_1}{\rho_1 c_1^2} + \frac{\alpha_2}{\rho_2 c_2^2} \tag{3.42}$$

The solution for the 5-equations diffuse interface model is strictly hyperbolic since

the eigenvalues are real and distinct. The corresponding right eigenvectors through the relation $A(W)r_i(W) = \lambda_i(W)r_i(W)$ (for $i \in \{1,\ldots,5\}$) are given below:

$$\mathbf{r}_1 = \begin{bmatrix} 0 \\ 0 \\ c \\ -\rho c^2 \\ 0 \end{bmatrix}, \quad \mathbf{r}_2 = \begin{bmatrix} 1 \\ 0 \\ 0 \\ 0 \\ 0 \end{bmatrix}, \quad \mathbf{r}_3 = \begin{bmatrix} 0 \\ 1 \\ 0 \\ 0 \\ 0 \end{bmatrix}, \quad \mathbf{r}_4 = \begin{bmatrix} 0 \\ 0 \\ 0 \\ 1 \\ 0 \end{bmatrix}, \quad \mathbf{r}_5 = \begin{bmatrix} 0 \\ 0 \\ c \\ \rho c \\ 0 \end{bmatrix} \tag{3.43}$$

The wave speed can be traced on a space-time diagram as seen in Fig. 3.6.

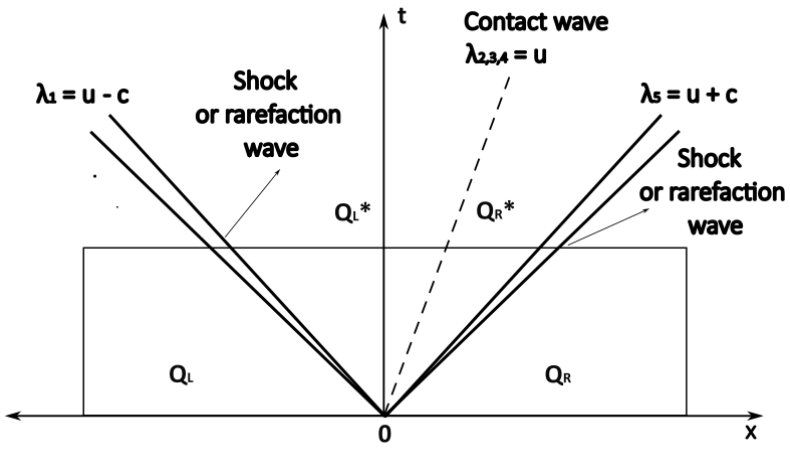

Figure 3.6: Schematic diagram of a discontinuous initial data with compressive characteristics on the (x,t) plane. The star region (*) represents the intermediate state.

3.5 Fluxes approximation & Temporal discretization.

To calculate the inviscid fluxes the exact Riemann solver will create some difficulties in solving, there is a need for an approximate Riemann solver. The fluxes are calculated using the HLLC Riemann solver of Toro, which is explained in section 3.5.1. To discretize the temporal domain, the third-order explicit Strong Stability Preserving (SSP) Runge-Kutta method is used, which is stable for CFL values up to 1. All volume, surface, or line integrals are approximated using a suitable Gaussian quadrature rule based on the polynomial order. Reconstruction is performed on either conserved or primitive variables, with transformation to conservative variables before flux calculation. These schemes are implemented in the open-source UCNS3D CFD code, written in Fortran 2003, and utilizing MPI message passing and OpenMP for parallelization. Further information on implementation and performance benchmarks can be found in [174, 169].

3.5.1 Harten-Lax-van Leer-Contact (HLLC) Solver

The HLLC solver which is an extension of the HLL (Harten-Lax-van Leer) solver, is a popular approximate Riemann solver for solving the five-equations DIM models and has been shown to be effective in the simulation of a range of compressible multiphase flows, including shock-tube problems, cavitation, droplet impact, and bubble dynamics. The HLLC solver includes an additional step to account for the presence of contact waves, which can arise in compressible multiphase flows when different phases interact and come to a pressure and velocity equilibrium. The method uses a local Riemann problem at each cell interface to determine the wave structure and speeds of the flow.

To calculate the fluxes in Eq. (2.36), the classical HLLC Riemann solver of Toro (1999) [166] for compressible single-phase flow is used to construct similarly for the hyperbolic set of equations in the diffuse interface paradigm for compressible multiphase flow. Applying the same principle to each phase separately by dividing the fluid into three regions: the left, middle, and right states. The left (L) and right states (R) are the states

on either side of a given cell interface, while the middle state is a special state that is defined based on the left and right states. The HLLC solver computes the fluxes across the cell interface based on the left, middle (contact wave), and right states, as well as the wave speeds associated with each state.This allows for an accurate prediction of the flow behavior at the interface between different phases.

The conservative part of the five-equations is written in the quasi-linear form below, where the conserved variables Q and the state flux F are represented in one-dimension below for simplicity.

$$\frac{\partial \mathbf{Q}}{\partial t} + \frac{\partial}{\partial x}\mathbf{F}(\mathbf{Q})) = 0, \tag{3.44}$$

where $\mathbf{Q} = (\alpha_1, \alpha_1\rho_1, \alpha_2\rho_2, \rho\mathbf{u}, \rho E)^T$, and $\mathbf{F}(\mathbf{Q}) = \left(\alpha_1\mathbf{u}, \alpha_1\rho_1\mathbf{u}, \alpha_2\rho_2\mathbf{u}, \rho\mathbf{u}^2 + p, \mathbf{u}(\rho E + p)\right)^T$

Four (4) regions of constant states that are separated by three (3) discontinuous waves is obtained. The discontinuous waves have two outer waves, which are shockwaves, and a middle one in the form of contact discontinuity. The middle region is denoted with a superscript and referred to as the "star region".

$$\tilde{\mathbf{Q}}(x,t) = \begin{cases} \mathbf{Q}_L, & \text{if } \frac{x}{t} \leq s_L \\ \mathbf{Q}_L^*, & \text{if } s_L \leq \frac{x}{t} \leq s^* \\ \mathbf{Q}_R, & \text{if } s^* \leq \frac{x}{t} \leq s_R \\ \mathbf{Q}_R^*, & \text{if } \frac{x}{t} \geq s_R \end{cases} \tag{3.45}$$

The wave speed of the three (3) discontinuous waves is given as:

$$s_L = \min\left\{u_L - c_L, u_R - c_R\right\}. \tag{3.46}$$

$$s_R = \max\left\{u_L + c_L, u_R + c_R\right\}. \tag{3.47}$$

$$s^* = \frac{\left(\rho u^2 + P\right)_L - \left(\rho u^2 + P\right)_R - s_l(\rho u)_L + s_R(\rho u)_R}{(\rho u)_L - (\rho u)_R - s_L\rho_L + s_R\rho_R}. \tag{3.48}$$

A flux across each of the wave speeds is constructed, s_L, s^* and s_R such that

$$\mathbf{F}_{j+\frac{1}{2}}^{HLLC} = \begin{cases} \mathbf{F}_L & 0 \leq s_L \\ \mathbf{F}_L^* = \mathbf{F}_L + s_L(\mathbf{Q}_L^* - \mathbf{Q}_L) & s_L \leq 0 \leq s^* \\ \mathbf{F}_R^* = \mathbf{F}_R + s_R(\mathbf{Q}_R^* - \mathbf{Q}_R) & s^* \leq 0 \leq s_R \\ \mathbf{F}_R & 0 \geq s_R \end{cases} \tag{3.49}$$

In a similar way, Toro (1999) [166] presented for single-phase, $\mathbf{Q}_L$ and $\mathbf{Q}_R$ can be expressed below as:

$$\mathbf{Q}_\mathbf{k}^* = \begin{bmatrix} \alpha_1\rho_1 \frac{s_k - u_k}{s_k - s^*} \\ \alpha_2\rho_2 \frac{s_k - u_k}{s_k - s^*} \\ \rho \frac{s_k - u_k}{s_k - s^*} s^* \\ \rho \frac{s_k - u_k}{s_k - s^*} \left[E_k + (s^* - u_k) \times \left[s^* + \frac{p_k}{\rho_k(s_k - u_k)} \right] \right] \end{bmatrix} \tag{3.50}$$

Where the mixture density $\rho = \alpha_1\rho_1 + \alpha_2\rho_2$ and k = L, R.

3.5.2 Third-order explicit SSP-RK time stepping

With $\partial Q/\partial t$ now evaluated using the HLLC, as detailed in the preceding section, the solution is advanced in time. The temporal integration employed in this thesis is the third-order explicit Runge-Kutta (RK) method that satisfies the Strong Stability Preserving (SSP) condition, developed by Gottlieb and Shu [56], and Spiteri and Ruuth, as implemented in [176] . This is a variant of the classic Runge-Kutta method of Shu and Osher and is able to preserve the stability and accuracy of the solution in the presence of non-linearities and other challenging features such as shock waves and discontinuities found in compressible multiphase flow.

The Eq. (3.1) can be rewritten in the following semi-discrete form

$$\frac{d\mathbf{Q}_i}{dt} = \mathbf{R}_i \tag{3.51}$$

where $\mathbf{R}_i$ represents the residual on the right-hand side, that should converge towards machine zero.

The 3rd-order explicit SSP-RK method is presented below, with $\mathbf{R}_i$ given by Eq. (3.51) :

$$\left.\begin{aligned} \mathbf{Q_i}^1 &= \mathbf{Q_i}^n + \Delta t \cdot \mathbf{R}_i\left(\mathbf{Q_i}^n\right) \\ \mathbf{Q_i}^2 &= \tfrac{3}{4}\mathbf{Q_i}^n + \tfrac{1}{4}\mathbf{Q_i}^1 + \tfrac{\Delta t}{4} \cdot \mathbf{R}_i\left(\mathbf{Q}^1\right) \\ \mathbf{Q_i}^{n+1} &= \tfrac{1}{3}\mathbf{Q_i}^n + \tfrac{2}{3}\mathbf{Q_i}^2 + \tfrac{2\Delta t}{3} \cdot \mathbf{R}_i\left(\mathbf{Q_i}^2\right) \end{aligned}\right\} \tag{3.52}$$

The time step Δt is given as follows:

$$\Delta t = K \min_i \frac{h_i}{S_i} \tag{3.53}$$

The CFL number for unsplit finite-volume schemes is defined as $K \leq 1/3$ according to reference [166].S_i represents the maximum propagation speed in cell i, which is determined by Eq. (3.54). h_i refers to the radius of the inscribed sphere of cell i.

$$S_i = sp_x \cdot n_x + sp_y \cdot n_y + sp_z \cdot n_z \tag{3.54}$$

where

$$sp_x = |u + c|, \quad , sp_y = |v + c|, \quad sp_x = |w + c|$$

$n = (n_x, n_y, n_z)$ denotes the unit normal vector pointing outward from the face of cell i, and c represents the speed of sound.

Chapter 4

Boundary Conditions

In this chapter, the boundary conditions that are applicable or of interest to the test problems that will be discussed in Chapter 5 are presented. Five categories of boundary conditions are considered in this thesis: *non-reflective (or transmissive), reflective, periodic, inflow and outflow*. Each is selected to suit the specific condition of the given test case. Non-reflective or transmissive boundary conditions are modelled to allow waves to exit or pass through the boundary without reflecting back. The conditions imply that the waves propagate out of the computational domain. In reflective boundary conditions, the fluid acts as if it is bouncing off an impermeable or solid wall. Periodic boundary conditions are characterized by their periodicity, which is important when the flow across the opposite sides of the computational domain is identical [123]. The periodicity constraint implies that the variables at the opposite ends of the computational domain have similar values. For test cases where a cyclical or periodic behavior is of interest, this is very useful [166]. Inflow boundary conditions are used to prescribe boundary conditions at the entrance or inlet of a computational domain. Given free-stream values describing the physical state, such as velocity, pressure, density, and temperature of the incoming flow, the initial flow state is used to initialise the simulation.In an outflow boundary condition, the state variables (pressure, volume fraction, velocity, and density) within the fictitious or dummy cell are copied from the adjacent cell located within the domain. This is done to mimic

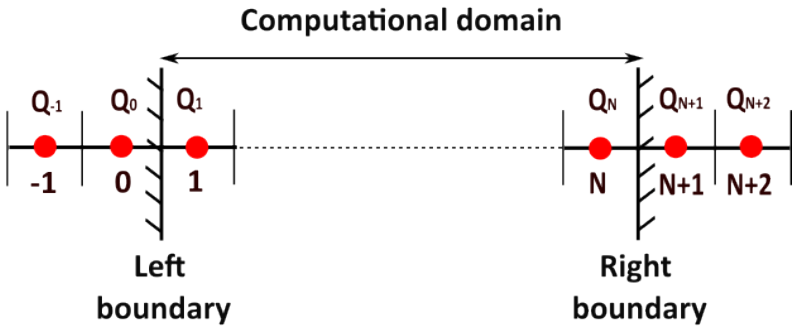

Figure 4.1: 1D computational domain showing the N-number of discretization. Two ghost/fictitious cells are added at the end of each boundary. The red dots represent the cell centres.

the flow behaviour as continuous as if there were no abrupt termination at the boundary as it exits the computational domain.

For the sake of simplicity, a 1D computational domain is focused on, as depicted in Figure 4.1. The domain is discretized into N cells, with the solutions located precisely at the center of each cell. To account for boundary conditions, additional fictitious or ghost cells along the edges of the domain are introduced. This extension increases the discretization from N cells to $N+2$ cells. In the context of these newly introduced cells, the Riemann problem is addressed to determine the fluxes, just as it is done for the interior cells. This augmentation enables us to appropriately handle the interactions at the boundaries. Specifically, the solution for the primitive variables $Q = (\alpha, \rho, u, p)$ at the center of each cell is computed at the onset of every time step, preceding the progression to the subsequent time step.

The aforementioned boundary conditions will be discussed below using Fig.4.1.

4.0.1 Reflective Boundary Conditions

In reflective boundary conditions, as shown in Fig. 4.2, all the state variables of Q_{N+1} at the right boundary within the fictitious $N+1$ cell are prescribed to have the same values as Q_N on the neighbouring N cell, with the exception of the normal velocity component, which is given a negative sign ($u_{N+1} = -u_N$) to represent the opposite direction of the wave being reflected. A similar procedure is used to derive the variables of Q_{N+2} on cell $N+2$ from those of Q_{N-1} (see Eq. 4.1). For the left boundary, Q_0 also takes the variables Q_1 and Q_{-1} from Q_2 (see Eq. 4.2). This condition essentially gives the boundary a reflective nature while preserving specific qualities or characteristics at the interface [123].

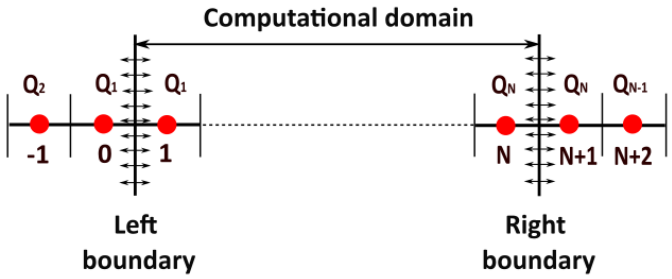

Figure 4.2: Schematic diagram showing reflecting boundary condition (left and right side). The two-directional arrows indicates the wave reflected at the boundaries of the given computational domain.

$$\mathbf{Q}_{N+1} = \mathbf{Q}_N \begin{bmatrix} \alpha_N \\ \rho_N \\ -u_N \\ p_N \end{bmatrix}, \quad \mathbf{Q}_{N+2} = \mathbf{Q}_{N-1} \begin{bmatrix} \alpha_{N-1} \\ \rho_{N-1} \\ -u_{N-1} \\ p_{N-1} \end{bmatrix} : \text{Right boundary} \tag{4.1}$$

$$\mathbf{Q}_0 = \mathbf{Q}_1 \begin{bmatrix} \alpha_1 \\ \rho_1 \\ -u_1 \\ p_1 \end{bmatrix}, \quad \mathbf{Q}_{-1} = \mathbf{Q}_2 \begin{bmatrix} \alpha_2 \\ \rho_2 \\ -u_2 \\ p_2 \end{bmatrix} : \text{Left boundary} \tag{4.2}$$

4.0.2 Non-Reflecting (Transmissive) Boundary Conditions

Transmissive or non-reflective boundary conditions, as opposed to reflective boundary conditions, allow for unimpeded wave propagation without the waves being perturbed, which would otherwise result in reflection. This simply implies that the variables Q_{N+1}

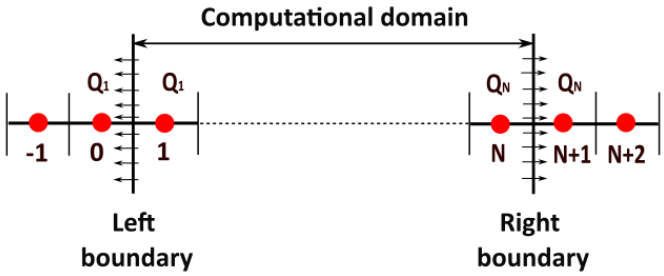

Figure 4.3: Schematic diagram showing non-reflecting (transmissive) boundary condition (left and right side). The two-directional arrows indicates visually unimpeded wave propagation at the boundaries of the given computational domain.

and Q_{N+2} at the ghost cells $N+1$ and $N+2$ correspond to the right boundary variables Q_N, whereas the variables Q_{-1} and Q_0 correspond to the left boundary variables Q_1. The non-reflective boundary condition on a 1D computational domain is depicted in Fig.4.3. For more details on non-reflective boundary, see [54, 166, 18].

$$\mathbf{Q_{N+1,N+2}} \Leftrightarrow \mathbf{Q_N} \begin{bmatrix} \alpha_N \\ \rho_N \\ u_N \\ p_N \end{bmatrix} : \text{Right boundary} \tag{4.3}$$

$$\mathbf{Q_{0,-1}} \Leftrightarrow \mathbf{Q_1} \begin{bmatrix} \alpha_1 \\ \rho_1 \\ u_1 \\ p_1 \end{bmatrix} : \text{Left boundary} \tag{4.4}$$

4.0.3 Periodic Boundary Conditions

In this approach, the flow is conditioned to go through one boundary and re-enters the opposite boundary, simulating the domain to appear continuous, despite the finite nature of the computational grid. From Fig. 4.4, consider the state variable Q_N at the right boundary. It re-enters the domain from the left boundary and exchanges the state variables of (Q_0. Similarly, the variable Q_{N+1} at cell $N+1$, as it exits the right boundary, is substituted with the value of Q_1 from the left boundary. This operation results in the interchange of all variables between the left and right boundaries, transforming them as follows: $Q_{-1}, Q_0, Q_1 \Leftrightarrow Q_{N-1}, Q_N, Q_{N+1}$..

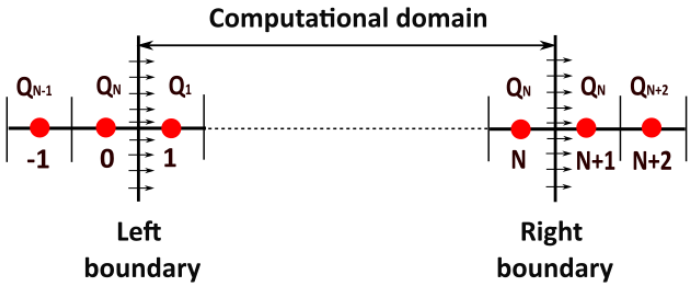

Figure 4.4: Schematic diagram showing periodic boundary conditions (left side). The state variable of cell $(N-1)$ and (N) re-entering into the computational domain from the left boundary

$$\mathbf{Q_{-1}} \Leftrightarrow \mathbf{Q_{N-1}} \begin{bmatrix} \alpha_{N-1} \\ \rho_{N-1} \\ u_{N-1} \\ p_{N-1} \end{bmatrix} \tag{4.5}$$

$$\mathbf{Q_0} = \mathbf{Q_N} \begin{bmatrix} \alpha_N \\ \rho_N \\ u_N \\ p_N \end{bmatrix} \tag{4.6}$$

$$\mathbf{Q_1} \Leftrightarrow \mathbf{Q_{N+1}} \begin{bmatrix} \alpha_{N+1} \\ \rho_{N+1} \\ u_{N+1} \\ p_{N+1} \end{bmatrix} \tag{4.7}$$

4.0.4 Inflow (Supersonic) and Outflow (Supersonic)

In Fig. 4.5, when considering inflow boundary conditions, the flow's state variables at the left boundary are determined based on the incoming free-stream values denoted as Q_0. These values are influenced by the Mach number, angle of attack, and side-slip angle, as explained in [20]. So, $Q_0 = Q_1$ (See Eq. 4.8). To emulate the flow's behavior as if there

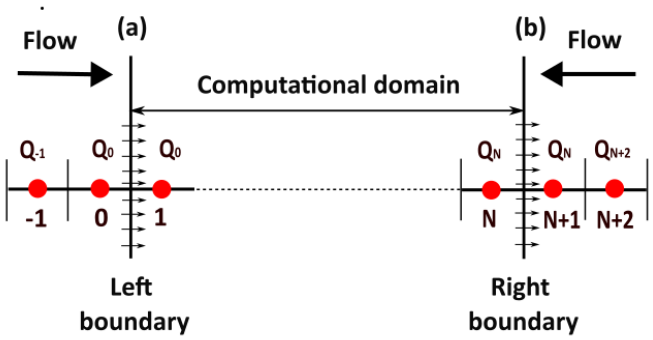

Figure 4.5: Schematic diagram showing inflow (a) and Outflow (b) boundary conditions.

were a seamless transition without abrupt termination at the right boundary when it exits the computational domain (as depicted in Fig. 4.5), the outflow boundary condition is set as follows: the state variables at the right boundary, where the flow exits the domain, are maintained as $Q_{N+1} = Q_N$ (See Eq. 4.9).

$$\mathbf{Q_{N+1}} = \mathbf{Q_N} \begin{pmatrix} \alpha_N \\ \rho_N \\ u_N \\ p_N \end{pmatrix} \tag{4.8}$$

$$\mathbf{Q_0} = \mathbf{Q_1} \begin{pmatrix} \alpha_1 \\ \rho_1 \\ u_1 \\ p_1 \end{pmatrix} \tag{4.9}$$

In the next Chapter, the specific test cases are discussed with the application of the outlined boundary conditions.

Chapter 5

Applications and Test Cases

This chapter focuses on presenting numerical simulations of compressible two-phase flows using diffuse interface models. The purpose is to evaluate the performance of the CWENO high-resolution interface capturing schemes in terms of accuracy, robustness, and computational efficiency. To validate and verify the methods, a set of two- and three-dimensional test cases has been selected, which includes reference to experimental and numerical data available in the literature. The aim is to ensure that the interface capturing CWENO high-order finite-volume methods are suitable for simulating compressible multiphase flows.

The convergence of the numerical scheme is considered first, to ensure it approaches an exact or reference solution as the spatial and temporal resolutions are refined, as well as the non-oscillatory features where the solution has shocks or other sharp features. This is to ensure that the numerical solution produced by the scheme is accurate and stable. The presence of spurious oscillations can lead to unphysical behavior and numerical instability in the computation. Two simple benchmark test cases are considered, which include the multi-species advection study and an isolated material interface. Based on the convergence order and non-oscillatory properties having a satisfactory result, other test cases are modelled to evaluate the performance of several other techniques for multi-component flow modeling. Test cases such as shock-bubble interactions and gas bubble

in water are considered. Other challenging test cases involving cavitation effects in compressible multiphase flow were carried out in the second part of the numerical simulations. In a series of underwater explosion (UNDEX) test cases at different boundaries, several parameters are investigated and also compared with the experimental and numerical results available.

5.1 Test Cases I

Using the high-order CWENO schemes of [177] in conjunction with the five-equation interface capturing schemes models [4, 79], the first two test problems were selected to study convergences and numerical stability, and last two were selected to study bubble dynamics and shock interaction of air-helium bubble and air-water bubble. The following are the test cases that will be considered for the first part of our numerical simulation:

1. Multi-species advection convergence study
2. Advection of contact discontinuity
3. Gas bubble collapse in water
4. Shock-Helium bubble interaction

5.1.1 Multi-species advection convergence study

This first test case is used to verify the spatial accuracy of the developed numerical schemes . The aim of this convergence testing is to ensure that the numerical solution is approaching the exact solution as the spatial resolution is increased. Other authors [187, 182] have also have also used this test case for same purpose. This numerical experiment involves the advection of a smooth initial profile of two gases' volume fractions in a periodic computational domain for a single period. Using the initial data of Wang et al. [182], the two-dimensional computational domain is a square domain $[0,1]^2$ and discretised using an unstructured mesh made up of arbitrary triangular elements with 10,

20, 40, and 80 edges per side resolution, as shown in Fig.5.3. The simulation's final time is set to $t_f = 1\text{s}$.

The initial physical parameters of each fluid:

$$(\rho_1, \rho_2, u, v, p, a_1) = (7, 1, 1, 0, 1/1.4, 0.5 + 0.25\sin(2\pi(x - 0.5))) . \tag{5.1}$$

To ensure that the time-step size is small enough for the schemes to achieve the designed order of spatial resolution, the simulations were ran with Courant number of 0.1. The wall-clock time for each simulation is normalised with respect to the fastest simulation time, which is provided by the CWENO3 method on the coarsest mesh in this setup. The e_{L^2} and $e_{L}\infty$ numerical errors are calculated as follows:

$$e_{L^2} = \sqrt{\frac{\sum_i \int_{\Omega_i} \left(\mathbf{Q}_e\left(x, t_f\right) - \mathbf{Q}_c\left(x, t_f\right)\right)^2 dV}{\sum_i |\Omega_i|}}, \tag{5.2}$$

$$e_{L^\infty} = \max \left| \left(\mathbf{Q}_e\left(x, t_f\right) - \mathbf{Q}_c\left(x, t_f\right)\right| \right|, \tag{5.3}$$

where $\mathbf{Q}_c(x, t_f)$ and $\mathbf{Q}_e(x, t_f)$ are the computed and exact solutions at $t_f = 1.0$ at the end of the simulation. The exact solution (x, t_f) is provided by the initial condition at $t = 0$. The result as shown in Table 5.1 indicates the schemes achieved their designed order of convergence for both $e_{L\infty}$ and e_{L^2}, based on the obtained convergence orders. The computational efficiency of the CWENO schemes are also shown in Fig. 5.1, the results indicates that for same computational conditions, the CWENO performs faster at a lower computational cost than the traditional WENO. For this test case, the CWENO requires $\approx$ 60-80 % computational time for same spatial order.

Also, the solution domain is discretised to a finer resolution for the CWENO's spatial resolution of $3^{rd} - 6^{th}$ order by increasing the edges per side (10, 20, 40, and 80 edges per side resolution). As one may expect, the accuracy increased with the grid resolution as the e_{L^2} error is observed declining in Fig. 5.1. The sixth-order CWENO's results were

the most accurate.

Table 5.1: Multi-species advection convergence study; The orders of convergence for the schemes are evaluated based on the volume fraction and normalized wall clock time at $t = 1.0$, along with the errors $e_{L\infty}$ and e_{L2}. All of the schemes achieve the desired accuracy, and the CWENO schemes only need about 60–80 percent of the time of an equivalent WENO scheme.

	CWENO					WENO				
Order/Edges per side	e_{L^∞}	O_{L^∞}	e_{L^2}	O_{L^∞}	*Time*	e_{L^∞}	O_{L^∞}	e_{L^2}	O_{L^∞}	*Time*
$3rd/10$	1.124E-02	-	6.897E-03	-	1.000	1.119E-02	-	6.880E-03	-	1.252
$3rd/20$	1.514E-03	2.89	9.535E-04	2.85	8.240	1.506E-03	2.89	9.492E-04	2.86	8.757
$3rd/40$	1.993E-04	2.93	1.244E-04	2.94	85.831	1.982E-04	2.93	1.236E-04	2.94	94.658
$3rd/80$	2.487E-05	3.00	1.581E-05	2.98	673.159	2.473E-05	3.00	1.571E-05	2.98	798.829
$4th/10$	1.879E-03	-	5.355E-04	-	1.530	1.867E-03	-	5.342E-04	-	1.821
$4th/20$	7.487E-05	4.65	2.762E-05	4.28	10.864	7.427E-05	4.65	2.739E-05	4.29	14.081
$4th/40$	4.962E-06	3.92	1.857E-06	3.89	115.068	4.912E-06	3.92	1.839E-06	3.90	144.007
$4th/80$	3.482E-07	3.83	1.200E-07	3.95	928.223	3.451E-07	3.83	1.188E-07	3.95	1128.293
$5th/10$	9.115E-04	-	4.777E-04	-	1.650	9.101E-04	-	4.775E-04	-	2.601
$5th/20$	2.994E-05	4.93	1.736E-05	4.78	13.055	2.997E-05	4.92	1.740E-05	4.78	19.929
$5th/40$	1.084E-06	4.79	5.816E-07	4.90	139.432	1.088E-06	4.78	5.833E-07	4.90	211.149
$5th/80$	3.327E-08	5.03	1.883E-08	4.95	1119.209	3.335E-08	5.03	1.889E-08	4.95	1738.832
$6th/10$	1.426E-04	-	4.309E-05	-	2.227	1.414E-04	-	4.321E-05	-	3.704
$6th/20$	2.447E-06	5.86	7.587E-07	5.83	16.729	2.467E-06	5.84	7.637E-07	5.82	30.602
$6th/40$	3.537E-08	6.11	1.207E-08	5.97	175.908	3.536E-08	6.12	1.212E-08	5.98	304.109
$6th/80$	6.493E-10	5.77	2.046E-10	5.88	1493.933	6.572E-10	5.75	2.055E-10	5.88	2417.527

5.1.2 Advection of material interface

To evaluate the non-oscillatory characteristics and convergence of their proposed numerical methods, authors commonly employ the advection test problem [187, 10, 59, 73, 2]. Given the frequent occurrence of sharp material interfaces in diverse multicomponent flows, the dependability of these proposed approaches is crucial for their effective deployment in such scenarios. The present multispecies test case involves the advection of an interface between two inert gases, nitrogen (Ni) and helium (He), with the domain divided into two regions representing different fluids. The temperature, pressure, and velocity of both components are constants across the material interface, and when maintained in equilibrium, the results are accurate. To assess the numerical framework's robustness for multiphase and multicomponent flows, traditional WENO and CWENO high-order schemes will be applied to Allaire et al.'s five-equation diffuse-interface multicomponent models [4] on unstructured meshes.

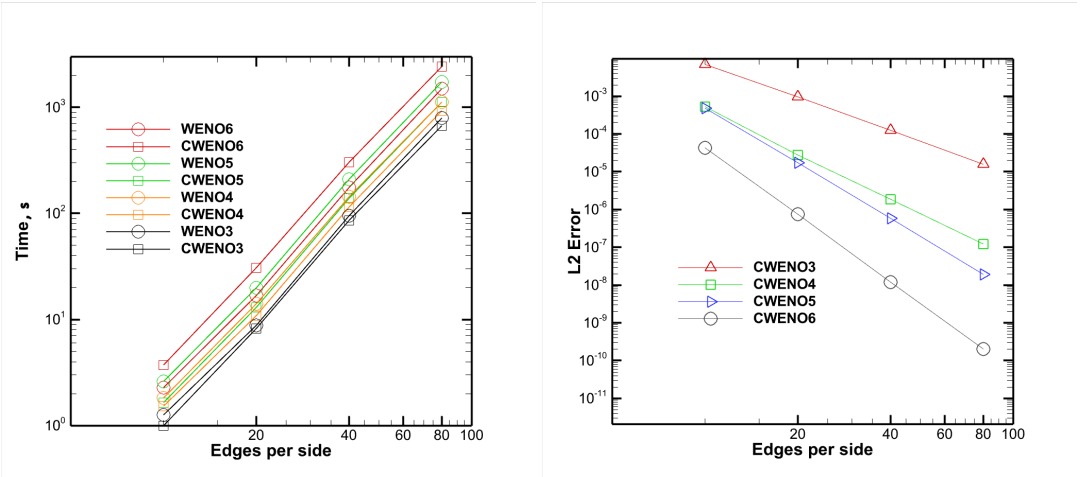

Figure 5.1: Multi-species advection convergence study; the plot of computational time against the grid resolution using the CWENO and WENO schemes of varying order of accuracy (on the left). It shows for a given order of accuracy, the CWENO has a lower computational cost than the WENO. The L_2 errors are plotted against the grid resolution to show a convergence (on the right). The CWENO6 as expected is the most accurate.

The computational domain is a square domain with dimensions of [1.0m x 1.0m] and is periodic in x and y direction. It is discretized using an unstructured hybrid mesh of triangular and quadrilateral mesh elements with a resolution of 80 edges per side, as depicted in Fig. 5.3. The simulation's final time is set to t_f =2 ms with a CFL number of 0.6, and a constant time step of $\Delta t = 0.005$ is employed. The initial flow state of Wong et al. [187] is utilized.

The initial physical parameters of each fluid:

$$(\rho, u, v, p, \gamma, a_1) = \begin{cases} (10.0, 0.5, 0, 1/1.4, 1.4, 1), & \text{if } x < 0.5 \\ (1.0, 0.5, 0, 1/1.4, 1.66, 0), & \text{otherwise.} \end{cases} \tag{5.4}$$

Both classical WENO and CWENO schemes employ primitive variables for reconstruction, using the HLLC Riemann solver outlined in section 3.5.1 to upwind the fluxes. The figures in 5.5 illustrate the results obtained for the gas-gas advection problem in terms of density, temperature, pressure, and velocity using the third-order WENO and CWENO schemes. The results demonstrate that CWENO3 oscillates much less near the material interface. The relatively coarse mesh was intentionally selected to emphasize one of the

key distinctions between the two schemes, namely the compactness of their directional stencils. In comparison to WENO schemes, CWENO's directional stencils correspond to lower-order polynomials, which results in significantly more compact stencils and reduced numerical oscillation in this test case.

Secondly, the influence of two types of reconstructions on the conserved and primitive variables is investigated. Figure 5.4 shows that the use of primitive variable reconstruction yields pressure and velocity solutions that are free from oscillations. Numerous studies [73, 74, 72, 75] have firmly established that in cases where γ is not constant, the reconstruction process using conservative or characteristic variables is prone to oscillations. As a result, reconstruction in primitive variables is necessary. Finally, when combined with primitive variables, the CWENO scheme (ranging from third to sixth order of accuracy) produces an accurate solution devoided of oscillations. The small oscillations in normalized pressure and velocity errors depicted in Fig. 5.5 are nearly equivalent to machine precision. The pressure profile error falls within the range of $[10^{-13}]$, whereas the velocity-u and v profiles error is within the range of $[10^{-}15]$.

Finally, with regard to computational resources, CWENO requires less computational power (as shown in Table 5.2) and is approximately four (4) times faster than the equivalent WENO schemes for a given grid size. This is consistent with the first test case, in which CWENO demonstrated the benefit of having a significantly lower computing cost. As a result, from now on, unless otherwise specified, the CWENO reconstruction with respect to primitive variables will be used for all other test cases in this thesis.

Table 5.2: Normalised wallclock time for the 2D advection of material interface at t = 2.0 [2].

	CWENO	WENO
Order	*Time*	*Time*
3*rd*	1.00	3.61
4*th*	1.41	4.95
5*th*	1.85	7.00
6*th*	2.28	9.39

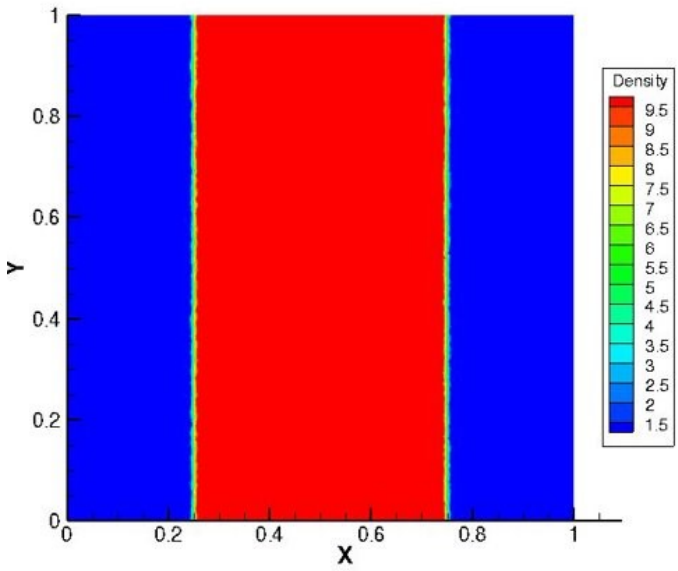

Figure 5.2: Advection of a material interface; density contour showing the interface of the two inert gases Ni and He.

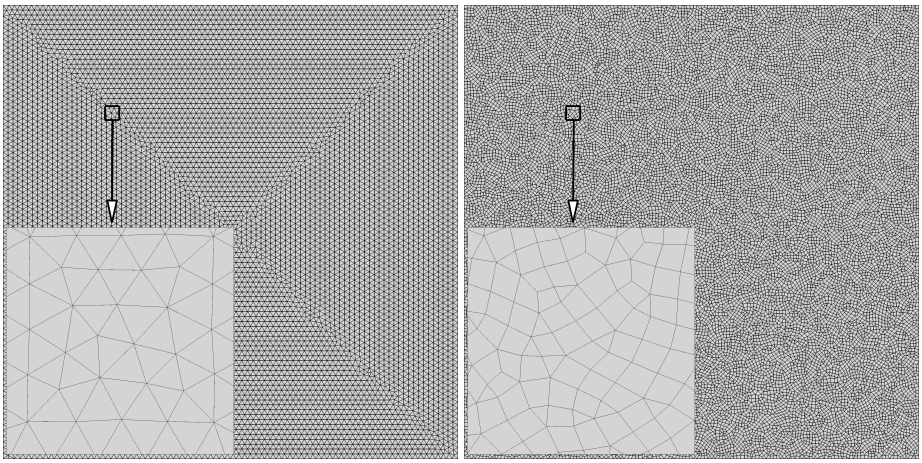

Figure 5.3: Advection of a material interface; here are illustrations of 2D unstructured meshes, comprising a triangular mesh (on the left) and a hybrid mesh (on the right). The zoomed-in area on the right provides a more detailed view of the mesh's structure.

5.1.3 Gas bubble collapse in water

This two-dimensional test case is used to study bubble collapse under a strong shock in water. It has also been numerically studied by [104, 55]. This test case has important applications in several areas, including the design of marine propellers in marine engineering, tissue ablation in biomedical research, and shock compression for studying the properties

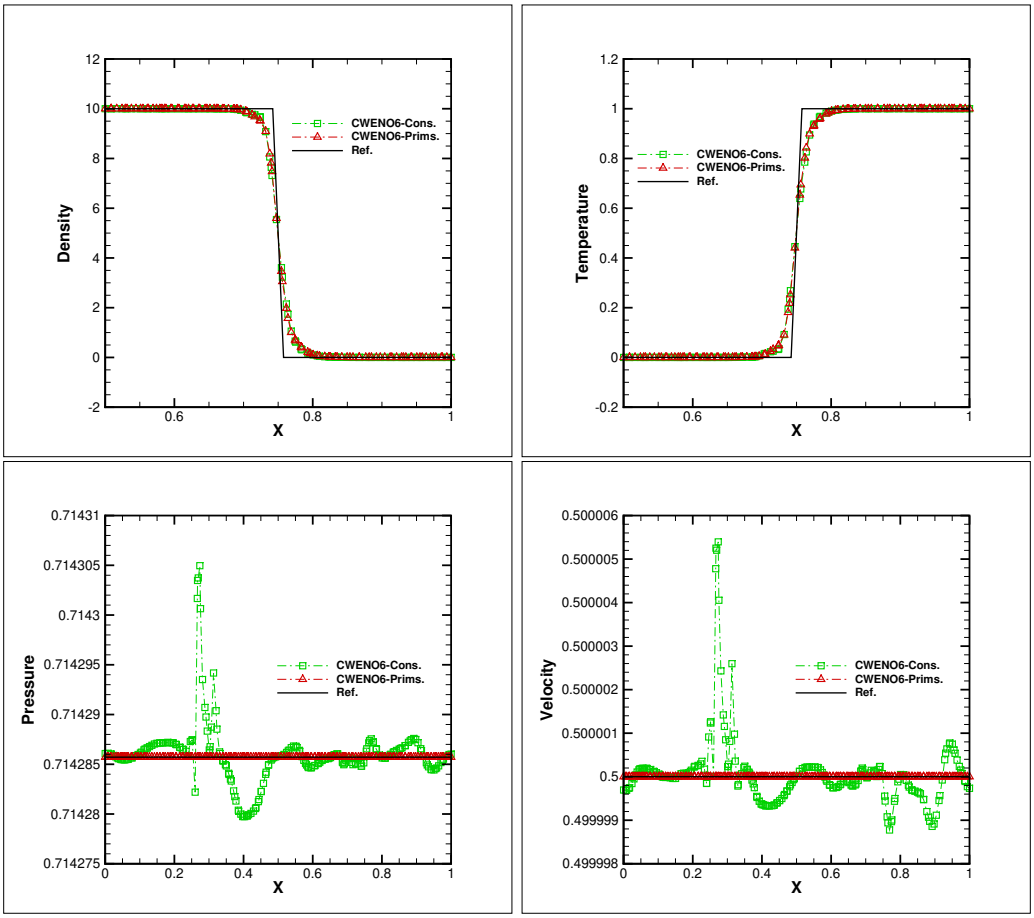

Figure 5.4: Advection of material interface; the exact solution is represented by the solid line. At time t=2, graphs illustrating the density, temperature, pressure, and velocity were generated using CWENO3 techniques with both conservative and primitive variable reconstructions. It is evident from the velocity and pressure plots that the CWENO conservative variable reconstruction results in artificial oscillations, which are not present in the CWENO primitive variable reconstruction.

of materials in materials science. The fluid's domain is a 2D square domain(Fig 5.7) with dimensions of $[0, 0.024]^2\ m^2$. A spherical gas bubble with a diameter of 6 mm is placed in water at the centre of the domain (0.012 m, 0.012 m). The shock is moving from left to right across the domain at M = 1.72 towards the air bubble; the shockwave's interaction with the air bubble gives rise to the peak pressure that will be of interest to this numerical study. The left and right surfaces' boundary conditions have been set as non-reflecting, and the domain's top and bottom surfaces are prescribed as Euler slip walls. Using a quadrilateral mesh with approximately 1.0 million cells and an average edge length of $e_c \approx D_b/250$ to discretise the domain, the final time of the simulation has been selected as $t = 6.2\mu s$.

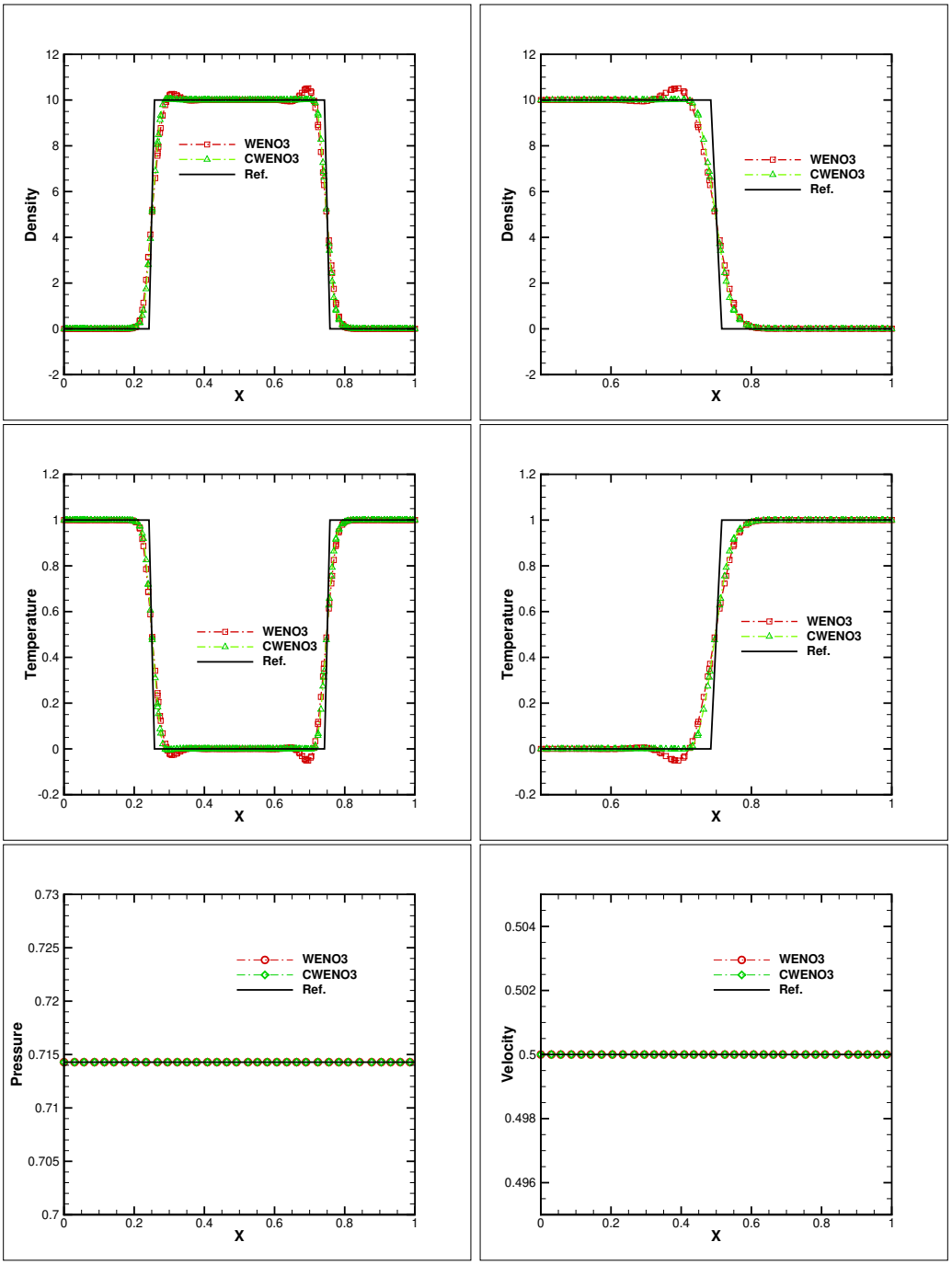

Figure 5.5: Advection of a material interface; the plot with a solid line represents the exact solution. The figures depict the density and temperature at time t = 2 using the CWENO3 and WENO3 methods, with reconstructions based on primitive variables. The results illustrate that the WENO3 schemes produces oscillations around the material interface, which are absent in the CWENO3.

The 4th-order CWENO scheme is employed for this test problem using the 5-equation diffuse interface model of Allaire et al.[4].

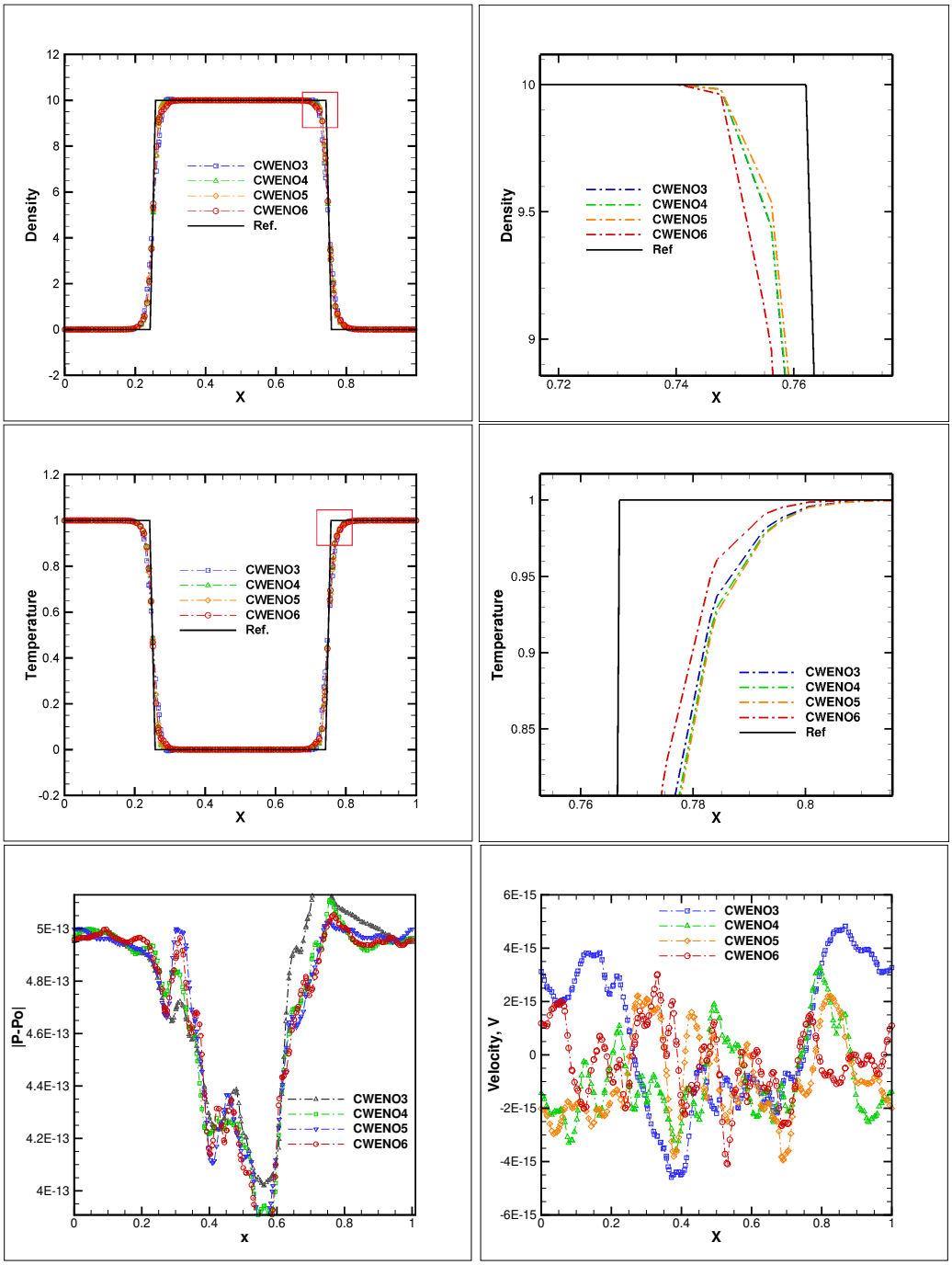

Figure 5.6: Advection of a material interface; using CWENO schemes of third to sixth order accuracy,the exact solution is represented by a solid line in the temperature and density profiles. The top two figures on the left highlights a zoomed-in view for the marked region. The errors in the pressure and velocity profiles at t = 2 s are presented in the bottom plot for each accuracy order, and it can be observed that the small oscillations are almost at the machine precision level.

The initial condition is given by:

$$(\rho,u,v,p,\gamma,\pi_\infty,\alpha_1) = \begin{cases} \left(1323.65, 681.058, 0, 1.9\cdot 10^9, 4.4, 6\cdot 10^8, 0\right), & \text{for Post-shock} \\ \left(1000, 0, 0, 10^5, 4.4, 6\cdot 10^8, 0\right), & \text{for Pre-shock} \\ \left(1, 0, 0, 10^5, 1.4, 0, 1\right), & \text{for Bubble} \end{cases} \tag{5.5}$$

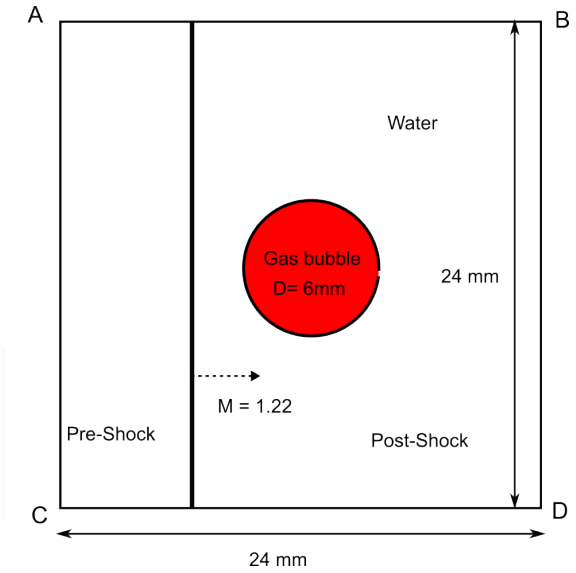

Figure 5.7: Computational domain setup for the gas bubble collapse in water test problem.

The figures presented in Fig. 5.8 and Fig. 5.9 demonstrate the bubble dynamics captured by the current schemes, depicting expected features such as the reflected rarefaction wave, water jet, blast wave, and secondary jets. The results are comparable to those obtained by other studies, including Nourgaliev et al. [104] and Goncalves et al. [55]. The highest pressure recorded in the computational domain is 7.7 GPa, which aligns with other research findings. For instance, Nourgaliev et al. [104] recorded $10.1GPa$ with a grid resolution of $e_c \approx D_b/800$, whereas Goncalves et al. [55] recorded a peak pressure of 7.8 GPa at a grid resolution of $e_c \approx D_b/300$. Moreover, the peak temperature at the time of minimum volume is approximately 15,670 K, which falls within the range observed in other studies [104, 55].

The changes in pressure along the centreline of the computational domain over time are shown in Fig. 5.9. It can be observed that the first peak, occurring at $t \approx= 3.9\mu s$, is caused by the blast wave, while the second peak at a later time ($t \approx= 4.9\mu s$) occurs when the blast wave collides with the bubble fragments, consistent with the findings of Goncalves et al. [55]. The diagram shown in Figure 5.10 demonstrates the changes in the volume of the gas bubble over time, using non-dimensional measurements. The findings are similar to those of Nourgaliev et al. [104], indicating the correct compression slope and rebound at later times. Nonetheless, the bubble's maximum compression is less

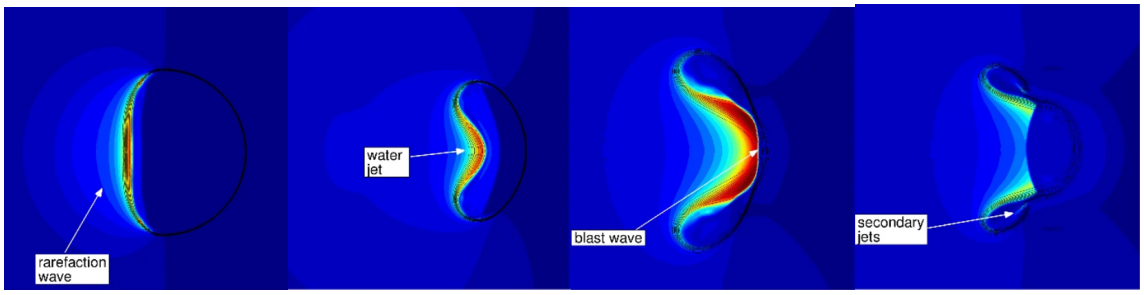

(a) $t = 0$ (b) $t = 57\ \mu s$ (c) $t = 205\ \mu s$ (d) $t = 403\ \mu s$

Figure 5.8: Gas bubble collapse test problem; Mach number (contours) and volume fraction (lines) plots at different duration are shown for the CWENO5 scheme. The figures demonstrate that the scheme successfully captures all the anticipated features of the problem.

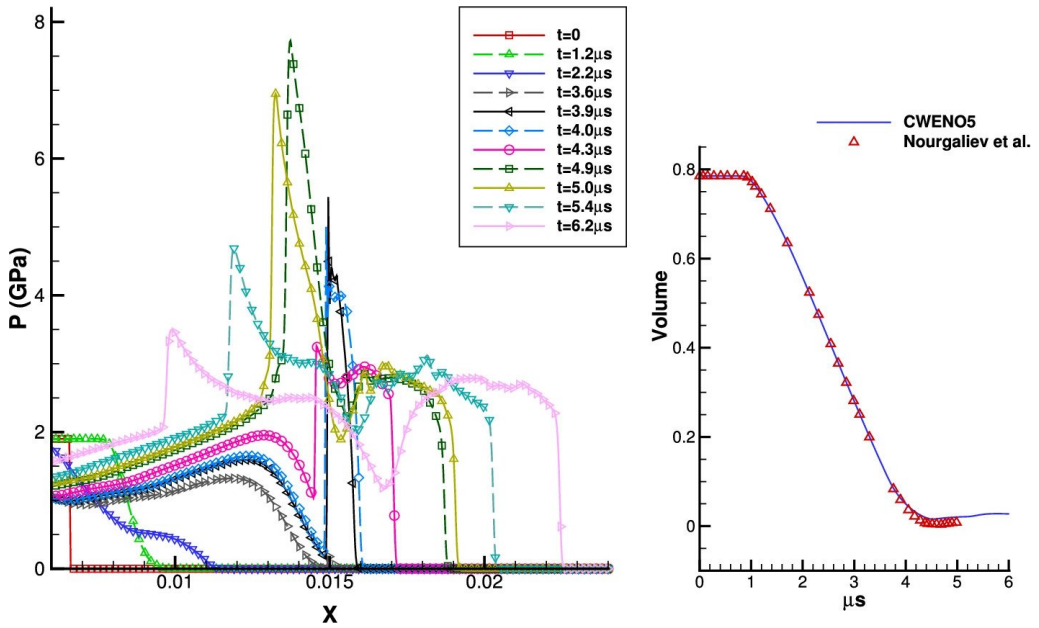

Figure 5.9: Gas bubble collapse test problem; plots on the left and right demonstrate the variations of pressure and non-dimensional volume, respectively, along the central axis of the simulated area .

pronounced in this study because of the less refined grid-resolution that was employed, in contrast to the results obtained by Nourgaliev et al. [104].

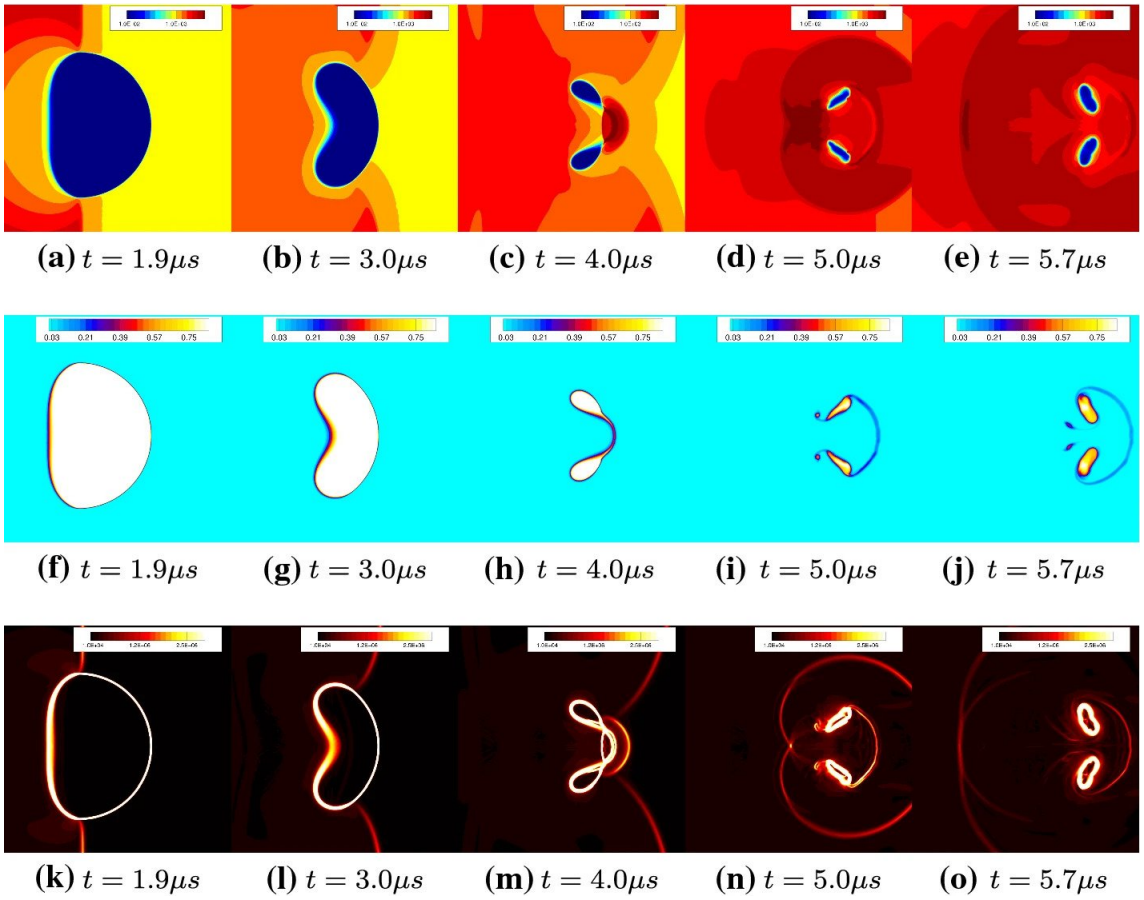

(a) $t = 1.9\mu s$ **(b)** $t = 3.0\mu s$ **(c)** $t = 4.0\mu s$ **(d)** $t = 5.0\mu s$ **(e)** $t = 5.7\mu s$

(f) $t = 1.9\mu s$ **(g)** $t = 3.0\mu s$ **(h)** $t = 4.0\mu s$ **(i)** $t = 5.0\mu s$ **(j)** $t = 5.7\mu s$

(k) $t = 1.9\mu s$ **(l)** $t = 3.0\mu s$ **(m)** $t = 4.0\mu s$ **(n)** $t = 5.0\mu s$ **(o)** $t = 5.7\mu s$

Figure 5.10: Gas bubble collapse test problem; plots depicting the density contours (uppermost), volume fraction(middle), and the magnitude of density gradient (bottom) for varying time frames of the gas bubble collapse experiment.

5.1.4 Shock-Helium bubble interaction

To investigate shock-bubble interaction, a more challenging test case that requires high resolution and robustness is considered in a two- and three-dimensional setup. This test case is based on the experiment of Haas and Sturtevant (1997) [58]. The experimental set-up of Haas and Sturtevant consists of a channel filled with water and a small helium bubble at atmospheric pressure located at the centre of the channel. A high-pressure shock wave, generated using a shock tube, is directed to hit the helium bubble. To set up the test case numerically, the computational domain is presented in Fig. 5.11. Several variations of this test problem have been studied by [182, 29, 73]. In a process similar to the experiment mentioned earlier, a spherical helium bubble that has a 28 % mass concentration of air in it and an initial diameter of D_0 = 5 cm is placed in water and struck

by a planar shockwave moving at Mach M = 1.22, as illustrated in Fig 5.11. Boundary conditions have been selected as reflecting for the top and bottom surfaces. Inflow and outflow are prescribed for the left and right surfaces of the domain. A coarse, medium, and fine hybrid unstructured mesh is used to discretize the 2D domain with an average element edge length in the shock bubble interaction zone of $e_c \approx D_b/35$, $e_m \approx D_b/120$, $e_f \approx D_b/400$ respectively, and arbitrary hexahedrals and prism elements with an edge length of $e_c \approx Db/50$ for the 3D domain . The final time of the simulation has been selected as $t = 1000\ \mu s$. The 5th-order CWENO scheme is employed for this test problem using the 5-equation Allaire et al. diffuse interface model. The initial conditions for this test case are given by:

$$(a_1\rho_1, a_2\rho_2, u, v, p, \alpha_1) = \begin{cases} (0.0, 1.204, 0, 0, 101325, 0), & \text{for Pre-shock} \\ (0.0, 1.658, -114.49, 0, 159060, 0), & \text{for Post-shock} \\ (0.158, 0.061, 0, 0, 101325, 0.95), & \text{for Bubble.} \end{cases} \tag{5.6}$$

From the results presented in Fig. 5.14, as the shock wave moves through the water medium, from the right side of the domain to the left, it interacts with the helium bubble. The bubble spherical shape changes, and it becomes more elongated in the direction normal to the shock front. As the bubble grows, three distinct interfaces emerge: the jet (ji), the upstream (ui), and the downstream (di), as illustrated in Fig. 5.12 It begins to deform the shock wave and create a bow shock in front of the bubble, causing the production of jets and vortices as the simulation nears its conclusion. The experimental shadowgraphs by Haas and Sturtevant [58], when compared with the current computational results at different instants in figure 5.13, show good qualitative agreement.

As can be seen in Fig. 5.15 and A.1, the high-order CWENO technique allows the Kelvin-Helmholtz instabilities that arise at the helium bubble interface to become more prominent as the 2D grid resolution is increased, whereas the 3D setup's resolution is insufficient to capture the instabilities.

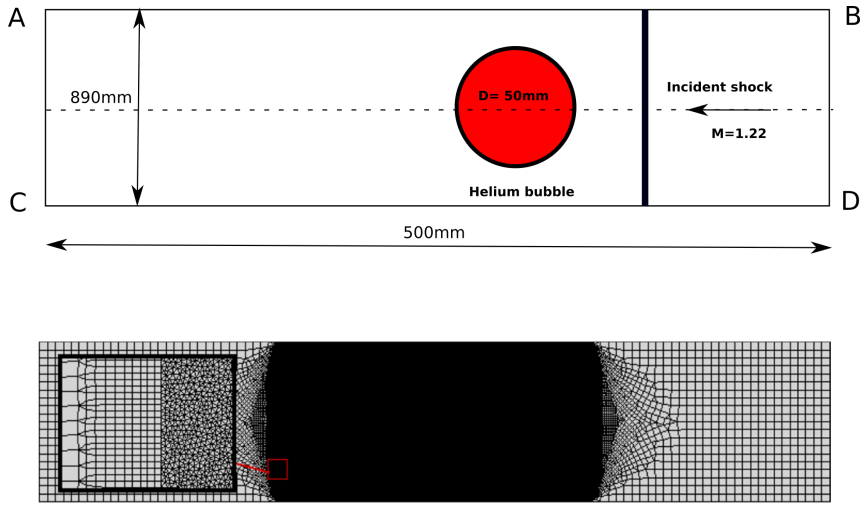

Figure 5.11: The computational domain setup for the helium bubble shock-wave test problem is depicted in the top image, while the corresponding fine mesh is shown in the bottom image.

Table 5.3: The simulation results were used to calculate the time-averaged velocities of various flow characteristics in the shock-bubble interaction problem. These values were then compared to the experimental findings of Haas and Sturtevant [58] and the computational results of Coralic and Colonius [29]. The velocities were averaged over time intervals of $[10,52]\mu s$ for the upstream interface, $[140,240]\mu s$ for the jet, and $[140,240]\mu s$ for the downstream interface. It was observed that all of the predicted values were within the range of experimental variations and were in good agreement with the computational results of Coralic and Colonius [29].

Grid size	$u_{ui}(m/s)$	$u_{ji}(m/s)$	$u_{di}(m/s)$
(2D) coarse	177.616	223.280	143.864
(2D) medium	179.514	234.960	144.999
(2D) fine	181.242	237.086	145.895
3D	178.402	228.375	144.197
Coralic & Colonius WENO5 [29]	173	230	145
Haas & Sturtevant exp. [58]	170 ± 17	230 ± 23	145 ± 15

The computed solution symmetry is lost at $t \geq 603\ \mu s$ for the medium and fine 2D meshes, which suggests that the framework used and the arbitrary unstructured elements in the refined shock-bubble interaction zone are multidimensional reconstructions.

Figures comparing the predicted positions with the reference results of Terashima and Tryggvason [160] and Quirk and Karni [121] based on the space-time diagram of these distinct interface positions and shows good agreement. It should be noted that the results are non-dimensional, using the bubble diameter at the time the shock hits it, as the reference length scale [160, 182, 121].

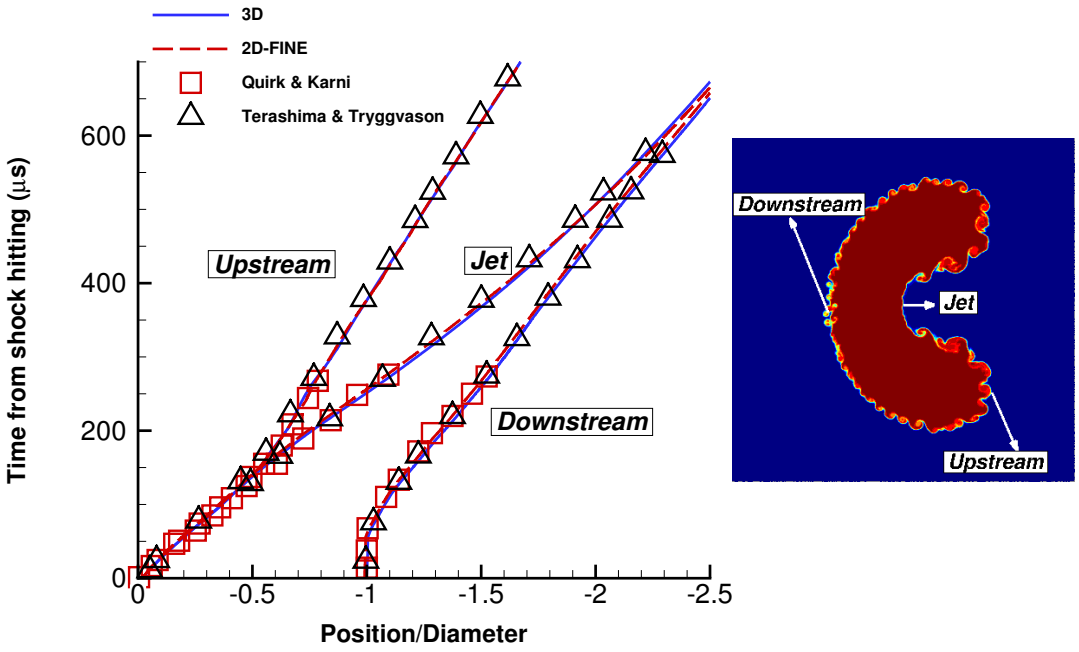

Figure 5.12: Shock-Helium bubble interaction; this figure shows the definition of interfaces and their position evolution during the interaction between a shock and a helium bubble. The CWENO5 scheme was used on both the finest 2D and 3D meshes, and the results are shown in the plot. The position evolution of the interfaces is consistent with the findings of previous studies by Terashima and Tryggvason [160] and Quirk and Karni [121].

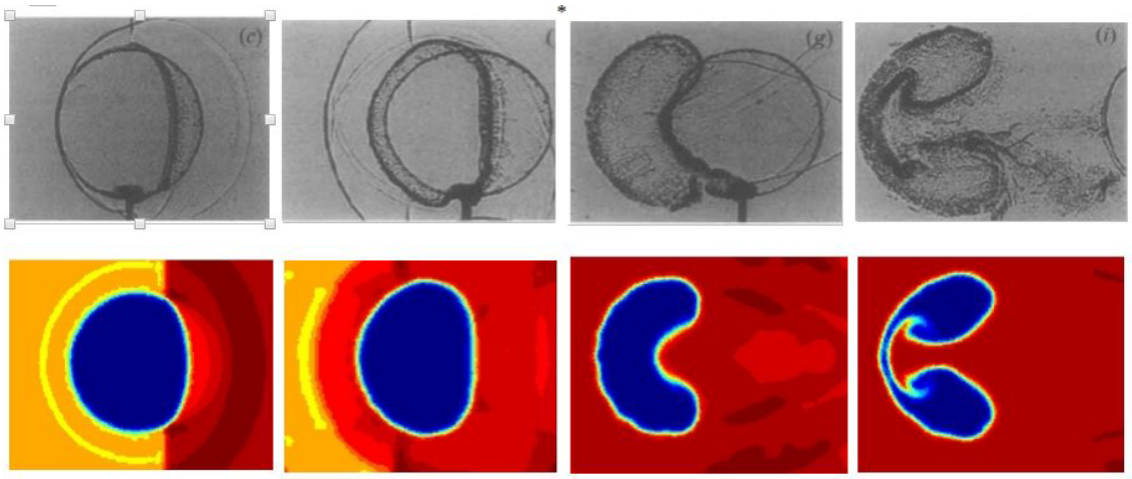

Figure 5.13: (i) Top shows experimental shadowgraphs of Haas and Sturtevant 1987 [58] experiment and and bottom shows computational result from UCNS3D at selected times of : (a) t= 37 ms, (b) t= 102 ms, (c) t= 427 ms, (d) t= 674 ms using a medium grid. [58] .

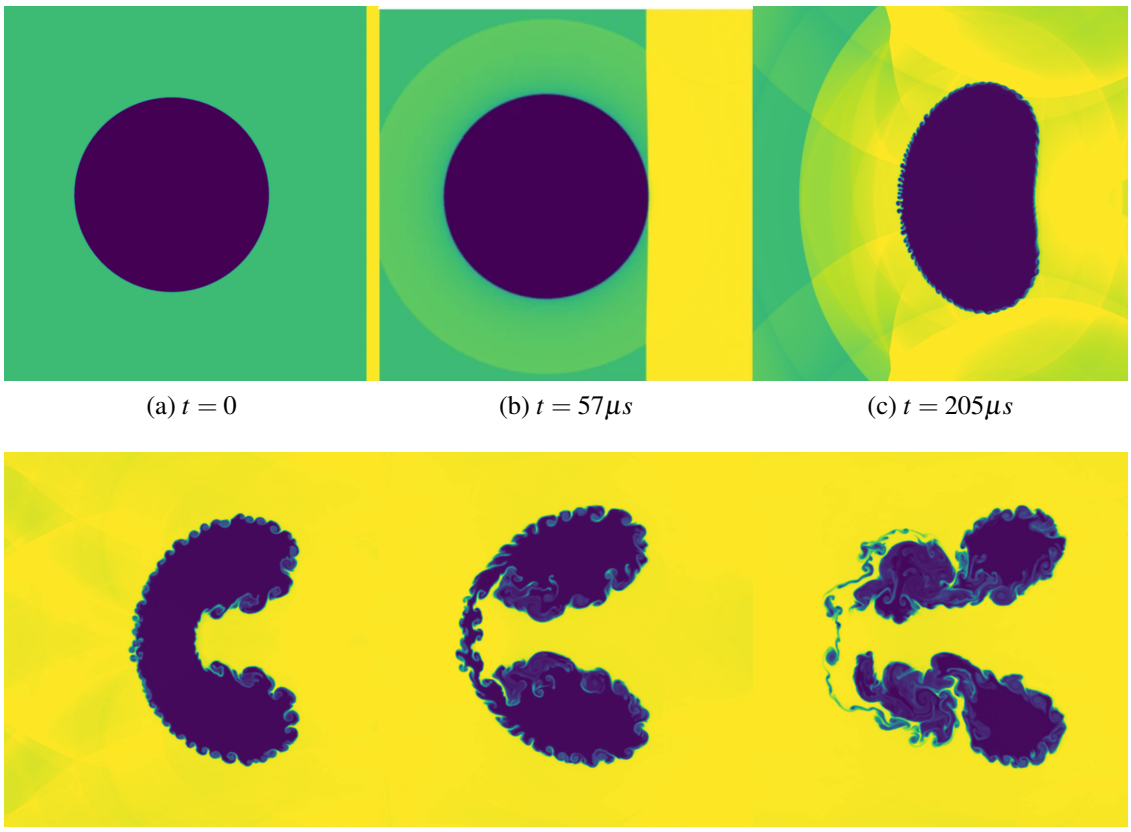

(a) $t = 0$ (b) $t = 57\mu s$ (c) $t = 205\mu s$

(d) $t = 403\mu s$ (e) $t = 603\mu s$ (f) $t = 983\mu s$

Figure 5.14: Shock-Helium bubble interaction; the density colour iso-levels showing the evolution of the bubble as it interacts with shock-wave-at different instants using the finest mesh structure. Kelvin-Helmholtz instabilities emerge at the interface between the materials at a later time of the bubble's evolution. As a result, asymmetric solution profiles are formed due to the breakdown of these instabilities.

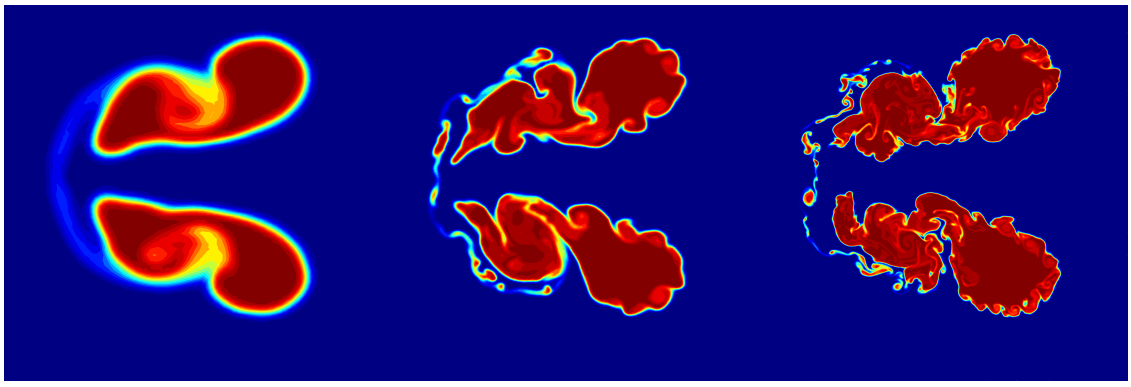

(a) coarse (b) medium (c) fine

Figure 5.15: Shockwave-Helium bubble interaction; colour iso-levels plots of the volume fraction at $t = 983\mu s$ using different mesh resolutions. At $t = 983\mu s$, the higher grid resolutions capture more vortical structures because physical viscosity is absent, and the solution is less diffused.

The velocities of the jet, upstream, and downstream interfaces obtained through averaging are consistent with the findings of Haas and Sturtevant's experiments [58] and Coralic and Colonius' computations [29], as presented in Table 5.3. In the 3D setup, the jet and downstream interface merge at a slower rate than in the two-dimensional setup due to the decreased spatial resolution.

5.2 Cavitation in Underwater Explosion (Test Cases II)

Cavitation, a zone of vapour bubbles within a liquid at low pressure due to high velocities and strong acceleration, is encountered in numerous scientific and engineering fields. Its useful applications can be found in marine design engineering, enabling high speed for submerged projectiles by reducing the skin friction drag, and in medicine for the destruction of kidney stones and the treatment of cancerous bodies. Its adverse effects cause material erosion, noise, and vibrations in marine propellers and turbomachinery. The practical impact of cavitation has high consequences and cannot be overemphasised. Several difficulties are encountered when investigating the cavitation dynamics numerically in compressible multiphase problems. The complex physics involved in the phase change of the mixture, the high gradients of the flow variables, the choice of numerical discretisation to capture these phenomena, and getting experimental results for validation are several factors to be considered.

Experiments related to underwater explosions, which are also referred to as UNDEX, gained popularity during World War II after a torpedo explosion near a naval vessel caused more structural damage than a direct hit (as shown in Fig. 5.16). In a study by [86, 95], the propagation of shock waves resulting from explosive detonation was examined in both air and water through a comparative analysis. The results showed that, given the same amount of explosive, an underwater explosion (UNDEX) could cause significantly more damage than an in-air explosion (INEX) [181]. Underwater explosions can generate high-pressure waves that can lead to the formation of cavitation bubbles in the surrounding water. This phenomenon, known as underwater cavitation, can have significant impacts on the surrounding environment and can cause damage to nearby structures.

As the gas explodes under water, it breaks the sound barrier. A shock-wave is then formed and transmitted at supersonic speed through the liquid, and the compression and rarefaction waves propagating in the liquid leave behind a cavitation region. The first damage to a nearby structure is from the high pressure from the high-speed moving shock-wave, this is regarded as the *primary loading*. The cavitation bubble created evolves in

Figure 5.16: Typical Underwater Explosion near U.S Navy Carrier [Source: US Navy, 2010] [82]

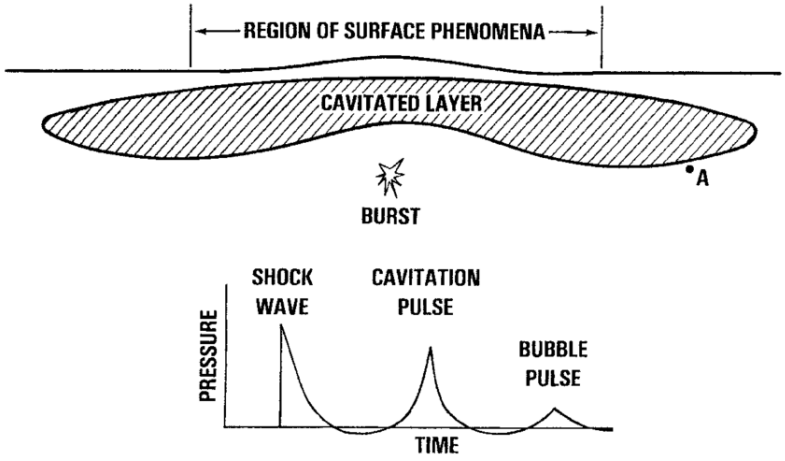

Figure 5.17: Bulk cavitation near a free surface [Source: Costanzo, 2010]] [30]

the fluid, and the pressures of the liquid change drastically [27, 21, 67, 80]. Due to inertia, the bubble over-expands and is subjected to a decreasing pressure, which may fall below the saturated vapour pressure of the water. Because the hydro-static pressure of the liquid surrounding the bubble is now greater than the pressure inside the bubble, the bubble collapses violently, generating high-speed jets and shock-waves that can cause a reloading on the structure; this is known as *secondary reloading*. Despite the fact that the maximum pressure generated by the reloading of cavitation collapse is lower compared to that produced by shock loading, it remains significant since the duration of cavitation collapse is often longer than that of the primary shock wave. This duration is enough to cause substantial damage to nearby structures.

Attached cavitations are the primary focus of most numerical studies in compressible

multiphase flow [115, 117, 85]. The cavitation created by an underwater explosion is classified as *bulk or hull cavitation*. In contrast to attached or sheet cavitation, where the cavitation boundary changes gradually and recurrently, the hull cavitation in an underwater explosion is fast and unsteady as it develops into varied dimensions before rapidly collapsing as a result of the surge in pressure. This creates more difficulty for numerical studies of such test cases. Our interest in this thesis is hull or bulk cavitation in compressible multiphase or multi-component flows such as those in underwater water explosions. The unsteady cavitation is so fast that there is no sufficient time for heat exchange.

Underwater explosions can occur near different boundaries or surroundings, such as a rigid boundary (a ship's hull), or a free surface. When an explosion occurs near a free surface, the high-intensity shock-wave created propagates rapidly and radially towards the free surface. It hits the free surface and reflects into the fluid as rarefaction waves caused by the tension created in the water. The surface deforms, and a low-pressure region of cavitation bubbles is formed underneath the free surface, leading to the cavitation known as *bulk cavitation*. The cavitation that forms subsequently collapses and generates high-energy shock-waves that can cause damage to a nearby object; this reloading effect is known as secondary reloading as mentioned previously . The cavitation reloading, or pulse, is created near the free surface and causes a peak pressure of quantity similar to that of the shock-wave and can be seen in Fig. 5.17. This indicates the significance of studying cavitation effects near free surfaces.

For nearby rigid boundaries such as a ship hull or submarine, the shock-wave from a detonated underwater explosive is transmitted at fast speed through the water, and depending on the proximity of the explosion centre to the structure, it travels until it hits the surrounding rigid boundary or wall and is then strongly reflected back into the fluid. There is fluid-structure interaction between the reflected shock and the air bubble, causing rarefaction towards the boundary and the formation of a low pressure region near the boundary, resulting in *hull cavitation* [57]. The centre point of such a boundary or wall is taken as the loading or pressure point for experimental and numerical study. In the

study of underwater explosions, it is very important to consider the effect of cavitation created by the pressure drop in certain regions of the fluid. This is very important because the damage caused by cavitation on a nearby rigid structure, as explained previously, is very substantial. This effect, whilst important, is frequently difficult to investigate experimentally. Therefore, studying it numerically complements the inadequacy of the experimental studies. For cavitation such as super-cavitation and incipient cavitation, researchers [134, 116] have successfully demonstrated that the DIM coupled with EoS is appropriate. But for hull or bulk cavitation often experienced in an underwater explosion where cavitation occurs fast, unsteadily, and rapidly evolves, the cavitating regions experience very steep and large variations in pressure, leading to non-physical pressure values below zero (negative pressures) which is not physically realistic, and sometimes can cause the failure of the numerical code. In simulating UNDEX using the diffuse interface models, circumventing the cavitation pressure from assuming negative values is commonly done using two different approaches. The first and most common way is to incorporate a *single-fluid model* to handle the non-physical pressure values occurring in the cavitation process. This approach has been used by several authors who have carried out similar UNDEX numerical simulations [185, 31, 191, 135, 52, 147]. Some methods in this category used by authors to circumvent this problem are the **cut-off model**, the **vacuum model** [159] , the **isentropic model** [94], the **Schmidt model** [140] and the **modified Schmidt model**. For details of these models, see [185, 190, 94]. The cut-off model is based on the assumption that cavitation bubbles are not formed until the pressure drops below a certain critical value, known as the 'cut-off pressure'. The cut-off model correctly predicts the peak pressure at the cavitation boundary during cavitation collapse in most cases, but it fails to predict accurate cavitation collapse periods [185]. If the void fraction, i.e. the ratio of the density of vapour bubbles to the total density of the fluid (ρ_g/ρ_l) is less than 10^{-5}, the Schmidt model is sufficiently accurate, but its limitations are in the mathematical inconsistencies in the calculation of the speed of sound, which makes it specifically applicable for high speed cavitating nozzle flows [185]. The modified

Schmidt model, which is an extension of the original Schmidt model, addresses the drawbacks or weaknesses of the Schmidt model and can be used for higher vapour to liquid density ratio 10^{-4} to 10^{-3} [185]. The vacuum cavitation model assumes a zero mass inside the cavitation bubble based on the fact that the amount of liquid or water in the vapour bubble is small and can be neglected. However, the vacuum and the modified Schmidt cavitation models are still limited in their ability to capture the complex shapes and dynamics of cavitation bubbles in multi-dimensional flow conditions. Of all the models, the isentropic model, which has been used for UNDEX in the five-equations DIM [31] is the most robust as it considers the mixture as consisting of isentropic vapour and liquid phases [196, 195]. But this process requires more computational resources as iteration is required to find the pressure, coupled with the fact that a model parameter k has to be predetermined before iteration [185]. Based on the advantages and drawbacks of these models, this study has adopted the cut-off model. That is considered herein, relatively simple to implement and do not alter the peak pressure accuracy at the cavitation boundary during cavitation collapse. This is very useful in the UNDEX test cases we will be considering in our studies. The one-fluid cavitation model is a pure phase model with no phase exchange taken into consideration, which is consistent with the no-phase transition of our five-equation interface capturing models (DIM) of Allaire et al. [4] and, that of Kapila et al. [79].

The one-fluid model will not be able to predict the mechanism or thermodynamic details of the cavitation process during cavitation formation and collapse, given that mass and heat transfer occur in the liquid-gas phase change between liquid and vapour for compressible two-phase flows. To address this shortcoming, the simplified five- or six-equation diffuse interface models are extended to include source terms in the energy and mass conservation equations that accommodate mass and heat transfer [198, 112]. This method is another way to prevent the non-physical pressure occurrence in the region of cavitation and is referred to as the *two-fluid cavitation models* [195]. The source terms are expressed implicitly by a simple algebraic relaxation solver for phase transition modelling

as proposed by Pelanti and Shyue [112, 113]. This method is much more complicated and computationally expensive for the non-equilibrium seven-equations model of Baer-Nunziato or Saurel. For simplicity, authors that have numerically studied UNDEX have used the reduced DIMs, such as the four-equations and five-equations interface capturing models, where mechanical equilibrium, thermal equilibrium, or both are enforced. In Jun's et al. study [195], they extended the phase transition model used by Chiapolino et al. [3, 25] for the five-equations, to study cavitation in underwater explosion test cases similar to the ones in this thesis. Existing DIMs with phase transitions include those by Pelanti and Shyue's six-equations [112, 147], Saurel et al.'s five-equations [137], Martelot et al.'s five-equations [88] , Zein et al.'s six and seven-equations [197], and others. Using the Kapila variant of the five-equation two-phase flow model in the presence of thermo-chemical relaxation terms during phase transition, Ma et al. [99] studied the liquid-vapour phase transition in cavitating flows for UNDEX test cases. In this thesis, the five-equations interface capturing models (DIM) of Allaire et al. and, Kapila et al. in the CWENO high-order framework is used to investigate the cavitation phenomenon in the underwater explosion near different boundaries; a planar solid wall, a closed cylindrical container, and a free surface. The parameters of interest includes the effect of shock loading and cavitation collapse reloading on nearby structure such as a ship's hull and in an enclosed structure like a closed tank, the bubble dynamics of cavitating flow induced by underwater explosions near a free surface, the impact of charge quality and detonation depth on cavitation. This will be assessed using four (4) UNDEX test cases in different surroundings; all these will be done in the open-source community UCNS3D solver [14].

5.2.1 Cut-off cavitation model

Any classical equation of state (EoS) for fluids can be used to define or describe the thermodynamics of the fluid under consideration. The stiffened-gas equation of state (SG-EoS) introduced by Harlow, and Amsden [61] is commonly used [133, 121, 132, 73] to achieve thermodynamic closure for multiphase compressible flow. However, in cases of cavitation, the EoS alone is only sufficient for pressure above a certain fixed saturation pressure referred to as $P_{\text{cut-off}}$. Once the pressure in the cavitation region drops below $P_{\text{cut-off}}$, the non-physical pressure computed assumes a new value, which is the value pre-defined for the cut-off pressure. Most authors [10, 31, 185, 199] have set $P_{\text{cut-off}}$ values in the range of $2000 - 5000$ Pa. In the cut-off method, the phase transition between the two interacting fluids is not considered. The relative ease of the cut-off model is the fact that it allows the simulation to proceed without the need to resolve the complex physics of bubble formation and collapse by simply preventing the formation of cavitation bubbles in regions where the pressure is above the cut-off pressure. However, the cut-off model's accuracy might be constrained in situations where the critical pressure differs greatly from other factors or when the dynamics of the flow are significantly influenced by the formation and collapse of cavitation bubbles.

In conclusion, the cut-off model is useful for simulating cavitation in compressible multiphase flows and is frequently employed in practical applications when a balance between accuracy and computational cost is required. Nonetheless, it is important to carefully consider the model's implementation in the context of the underlying physics and the desired level of accuracy. In the case of this thesis, the cut-off cavitation model suits the desired outcome for the test cases is considered.

The cut-off method is presented below:

$$P_{i,j,k} = \begin{cases} EoS, & \text{if } P_{i,j,k} > p_{\text{sat}} \\ p_{\text{sat}}\,, & \text{if } P_{i,j,k} < P_{\text{sat}} \end{cases}$$

The mixture's internal energy can be expressed as :

$$\rho_i e^{\mathrm{I}}_{i\,\mathrm{sat}} = \left(\frac{P_{\mathrm{sat}} + \gamma_i . P_{\mathrm{c,i}}}{\gamma_i - 1}\right) \tag{5.7}$$

The total energy is now:

$$\sum_{i=1}^{N} \rho e^{\mathrm{T}} = \sum_{i=1}^{N} \alpha_i \left(\frac{P_{\mathrm{sat}} + \gamma_i . P_{\mathrm{c,i}}}{\gamma_i - 1} + \frac{\rho_i . U^2}{2}\right) \tag{5.8}$$

Using the high-order CWENO schemes of [172] in conjunction with the five-equations interface capturing schemes models [4, 79], four underwater test problems were selected to study the cavitation effect of underwater shock near different boundaries.

1. Underwater explosion near a planar wall
2. Underwater explosion near a free surface
3. Underwater explosions in a rigid cylinder
4. Underwater of two bubbles near a free surface
5. Underwater of two bubbles placed vertically in an enclosed region.

5.2.2 2D underwater explosion near a free surface

To investigate the bubble dynamics at the material interface of the air-water medium of an underwater explosion, a two-dimensional underwater explosion near a free surface is considered. This work has been studied numerically by [118, 31, 59, 192, 143, 142, 202, 143, 78], as well as experimentally [202, 81]. The experimental set-up of Kleine et al.[81] consists of a spherical charge of 10 mg silver azide with an initial energy of 25.5 J/m placed in an open cylinder filled with water and exploded into the air-water medium. The overall process of the experiment involves: charge detonation, bubble pulsation, and jet formation [202].

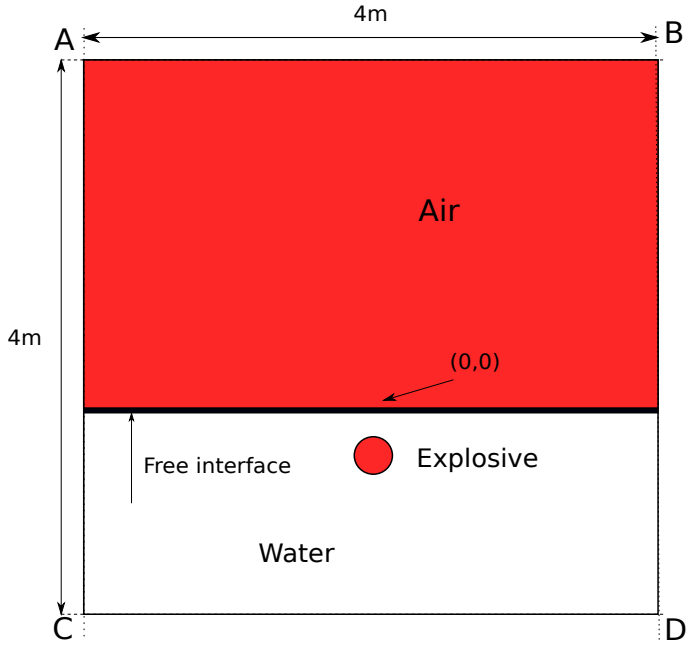

Figure 5.18: Computational domain setup for two-dimensional underwater explosion near a free surface.

Numerically, in an underwater explosion, cylindrical bubbles with high pressure are used as a substitution for the explosive. A 0.24-m-diameter pressurised gas bubble is placed in the two-phase medium at $[0, -0.3]m$.

Our computational domain, which has the same dimensions as Shukla's (2014) [142], is a square area with $x \times y$: [-2m , 2m] × [-1.5m , 2.5m] , as shown in Fig. 5.18. The air-water interface is positioned at the centre [0, 0] of the computational domain. The boundary conditions of the top, left and right surfaces are set up as non-reflecting

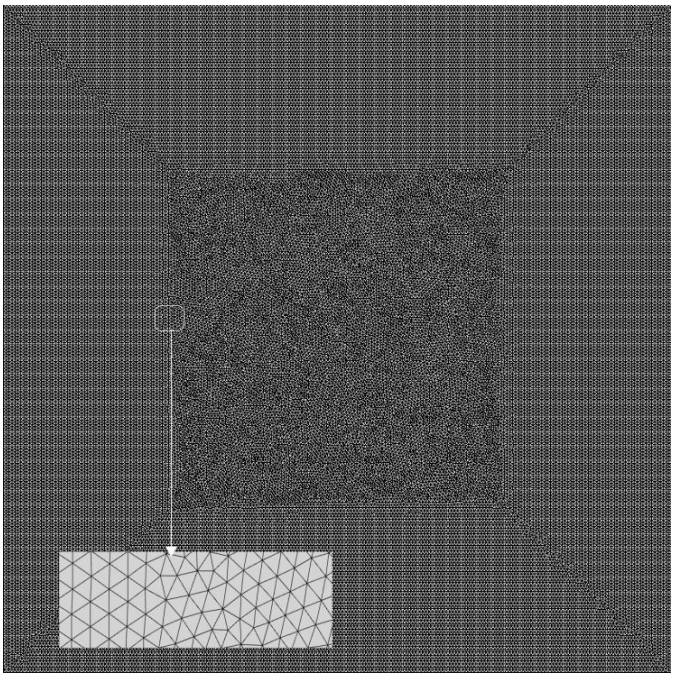

Figure 5.19: Underwater explosion near a free surface; 2D unstructured finest mesh with triangular elements used for this test case. The density of mesh elements in specific areas of the domain is increased to better capture the physical phenomena occurring in those regions.The zoomed-in area on the right provides a more detailed view of the mesh's structure.

boundary conditions, while the bottom is set to reflect. The final time of the simulation is selected as t = 1.2 ms, and each fluid's initial physical parameters (density, velocities, pressure, specific ratio, and volume fraction) are presented below.

$$(\rho, u, v, p, \gamma\alpha) = \begin{cases} \left(1.225, 0, 0, 10^5, 2.0, 0\right), & \text{Air} \\ \left(1250, 0, 0, 10^9, 2.0, 1\right), & \text{Explosive} \\ \left(1000, 0, 0, 10^5, 7.15, 0\right), & \text{Water.} \end{cases} \tag{5.9}$$

The high-order finite-volume method based on the CWENO4 schemes of Tsoutsanis et al. [177, 172] with three different grid resolutions (coarse, medium, finest) to investigate

the material interface between the bubbly gas and the free surface of the air-water medium. Numerical Schlieren visualisations for density and pressure gradients are presented in Fig. 5.20 and Fig. 5.21 at different instants. The high-pressure air bubble explodes, and the shock-wave spreads outwardly towards the interface until it hits the air-water interface and reflects into the water. This results in cavitation bubbles, which can be seen in the pressure gradients shown in Fig. 5.21. The volume fraction contour in Fig. 5.22 shows that the bubble has evolved from its spherical formation to an oval shape at this point.

Using different grid resolutions, the CWENO4 is used to capture the interfacial region between the bubble and the air-water medium. On a sequence of refined grids (coarse, medium, finest), the smearing or numerical diffusion between the free surface and the expanding air bubble becomes less. On the finest grid, the CWENO gives a sharp description without the need to use interface sharpening or anti-diffusion techniques used by most authors [99, 10, 142] on high-order schemes such as WENO to improve their results. The CWENO4 is used for quantitative studies on a medium grid, and a density and pressure profile along the horizontal axis (x = 0) is plotted against published results where the sharpening technique [34], and also anti-diffusive [82] technique are used on high order schemes. The results shown in Fig. 5.23 and 5.24 are consistent with the published results of [99, 10, 147]. In addition, results from both Allaire et al. and Kapila et al. are compared to investigate the compressibility effect of the $K\nabla \cdot \mathbf{u}$ term in the Kapila et al.five-equation models in the fluid's mixture region. It can be noticed from the obtained density and pressure plots shown in Fig. 5.25 that both diffuse-interface multi-component models of Allaire et al. and Kapila et al. have very similar results and are both in good agreement with the published works of [34], [82]. In Fig. 5.26, the maximum peak pressure for the finest mesh is approximately 8.5 MPa at approximately x = -1.0 m, which is where the shock-wave is reflected hitting the expanding cavity from below. As described in [34], traditional WENO schemes, which are computationally more expensive than CWENO, are also not able to prevent the air-water interfaces from smearing. This result shows the CWENO can resolve the material interfaces with less numerical smearing

while maintaining their essentially non-oscillatory character. This is in agreement with [172] and leaves the CWENO schemes a better choice at a lower computational cost for compressible multiphase or multicomponent flows with cavitation.

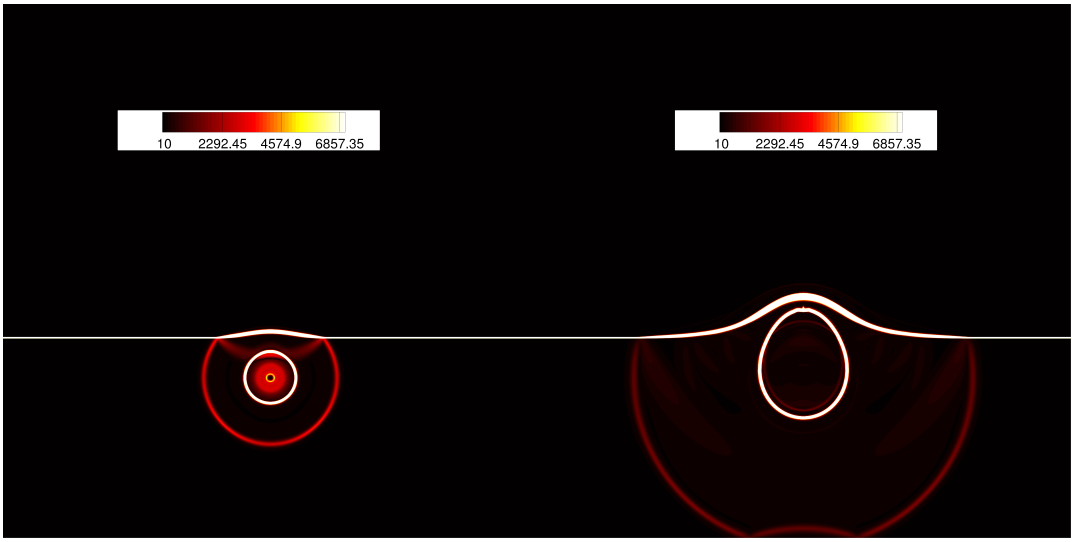

(a) $t = 0.2$ ms (b) $t = 0.4$ ms

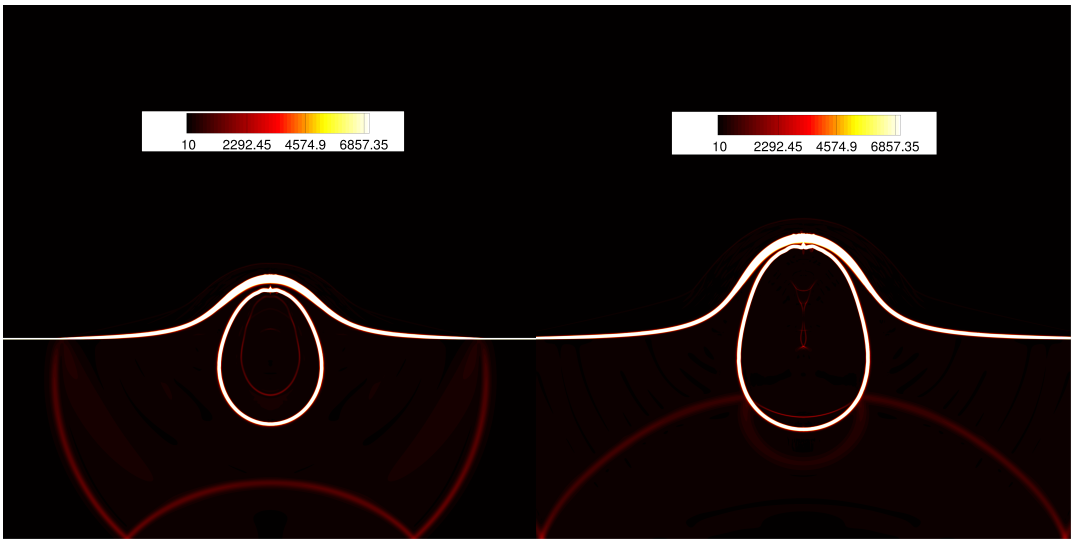

(c) $t = 0.8$ ms (d) $t = 1.2$ ms

Figure 5.20: Underwater explosion near a free surface; Schileren visualization of density gradient using a CWENO4 scheme on a resolution of 1600×1600 cells (finest mesh) at $t = (0.2, 0.4, 0.8, 1.2)$ ms.

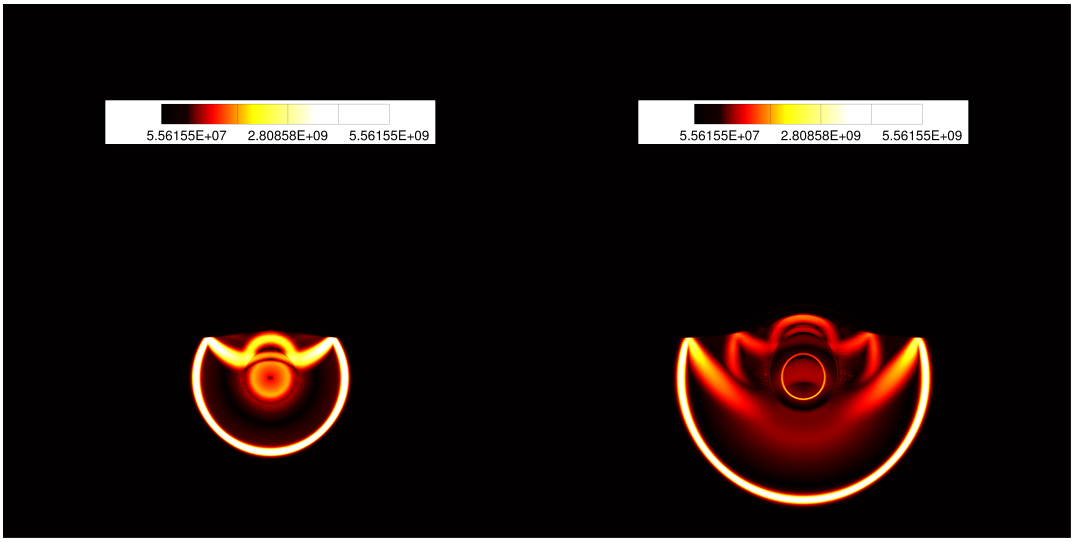

(a) $t = 0.2$ ms (b) $t = 0.4$ ms

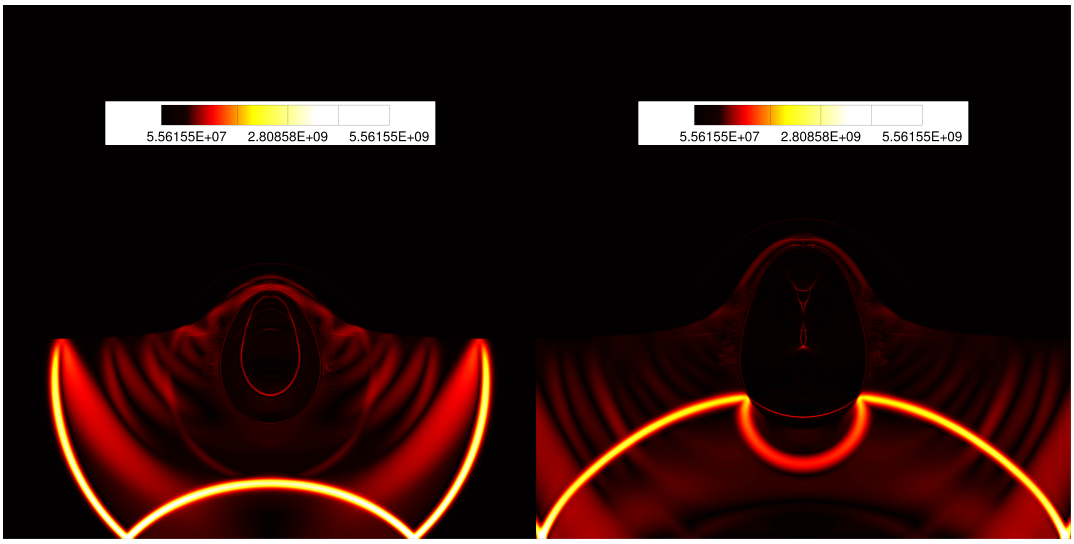

(c) $t = 0.8$ ms (d) $t = 1.2$ ms

Figure 5.21: UNDEX near a free surface; Schileren visualization of pressure gradient using a CWENO4 scheme on the finest mesh at t = (0.2, 0.4, 0.8 and 1.2)ms.

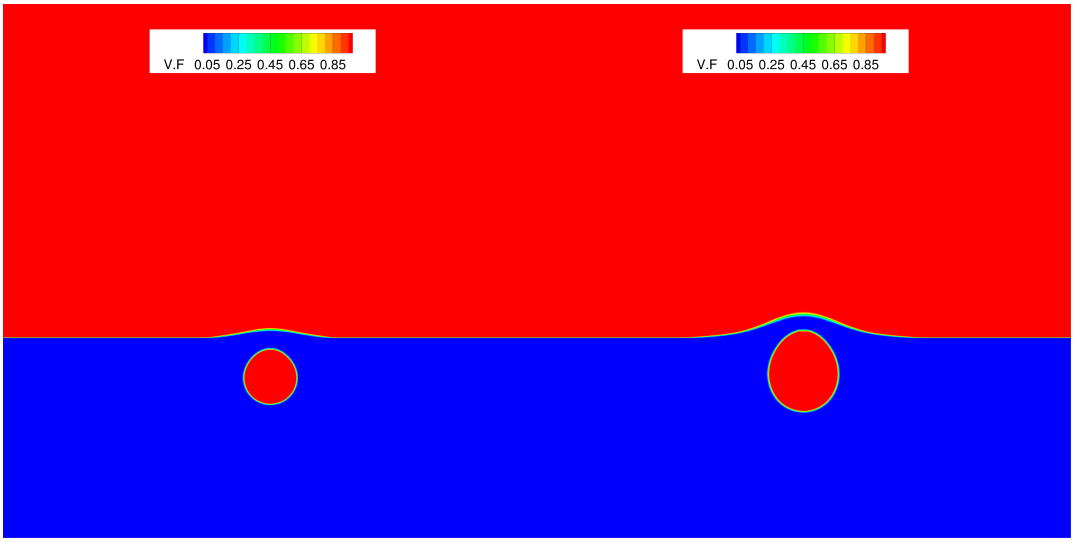

(a) $t = 0.2$ ms (b) $t = 0.4$ ms

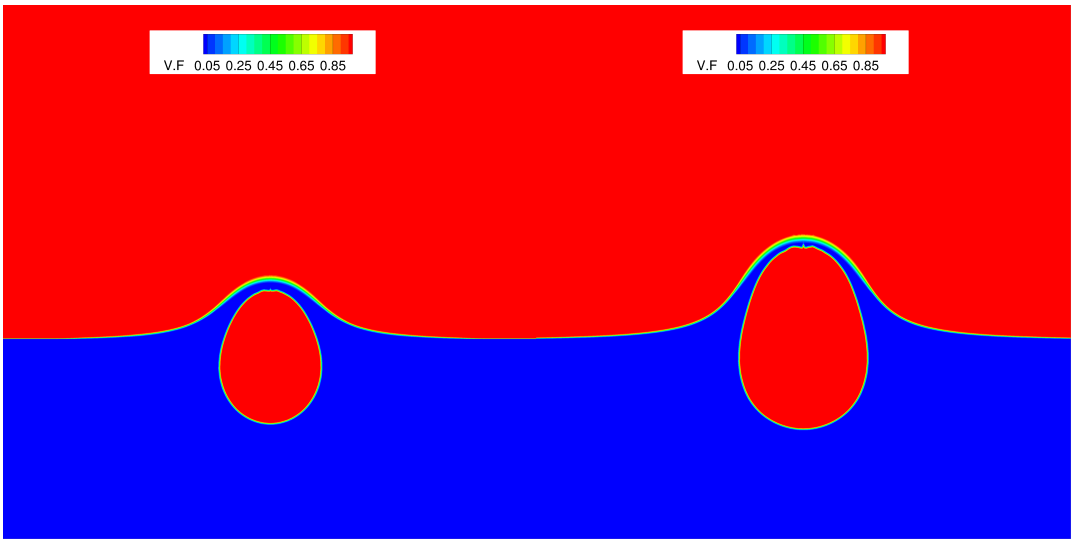

(c) $t = 0.8$ ms (d) $t = 1.2$ ms

Figure 5.22: UNDEX near a free surface; contours of volume fraction for underwater explosion near a free surface using a CWENO4 scheme on finest grid at t = (0.2, 0.4, 0.8 and 1.2)ms.

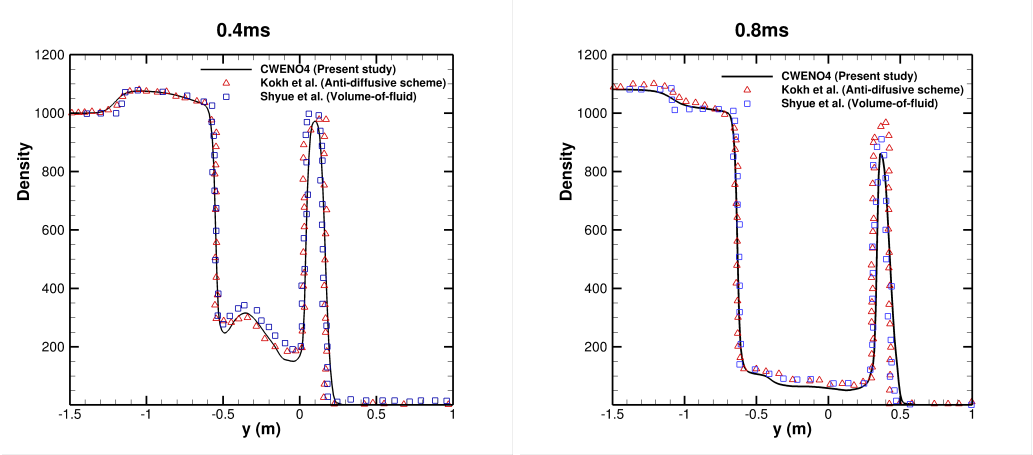

Figure 5.23: UNDEX near a free surface; cross-sectional plot of the density distribution along x = 0 at two instants, specifically t = 0.4 ms and t = 0.8 ms. The obtained results are compared to those reported in previous studies of Kokh (2010) [82] and Shyue (2006)[146].

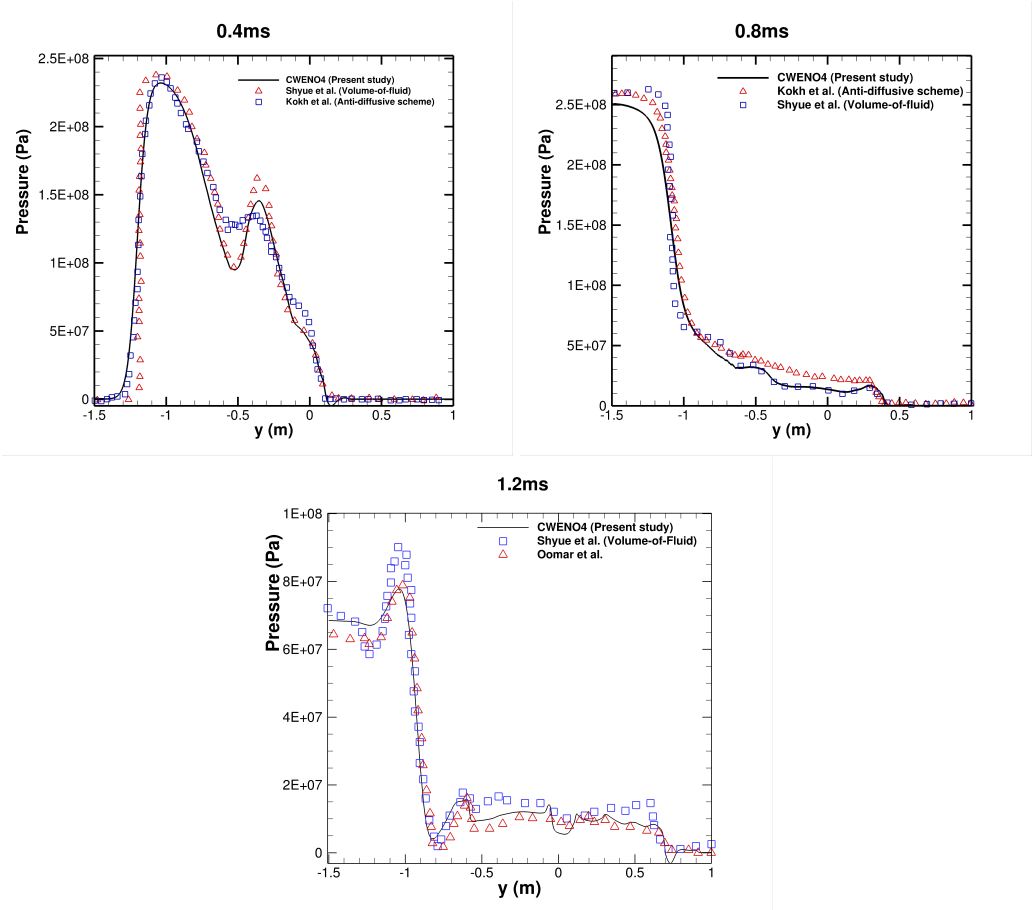

Figure 5.24: UNDEX near a free surface; cross-sectional plot of pressure along x = 0 at t = 0.2ms. Comparison are made with the results of [82], [146] and [108]

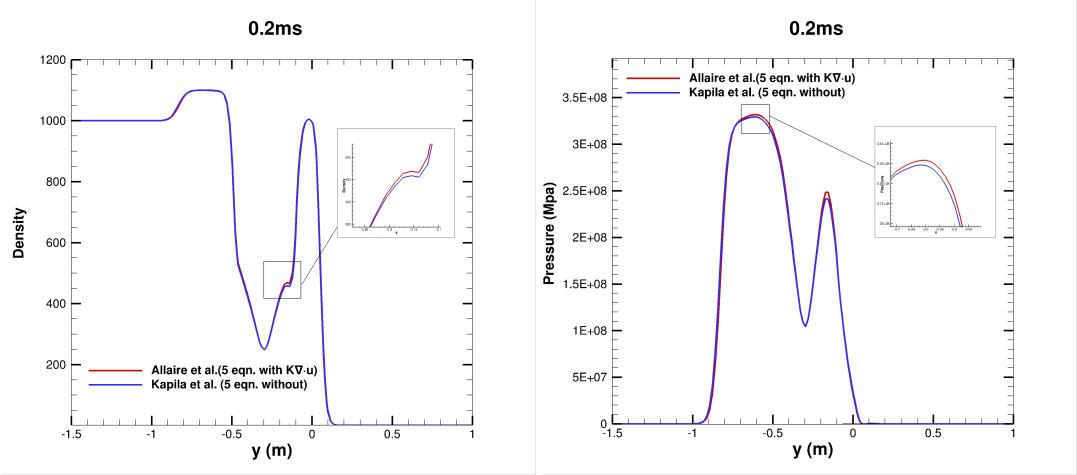

Figure 5.25: UNDEX near a free surface; cross-sectional plot of density and pressure along x = 0 at instants t = (0.4; 0.8)ms using Allaire et al. [4] and Kapila et al. [79] models.

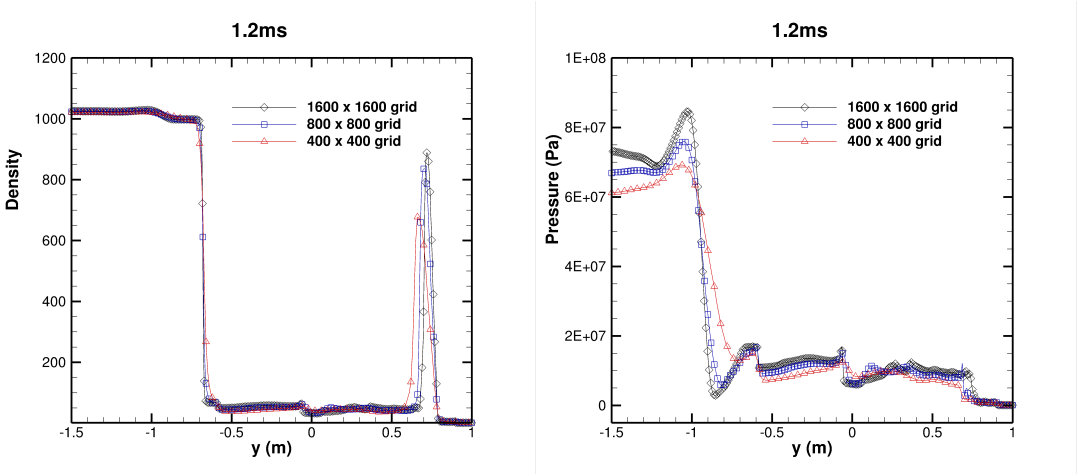

Figure 5.26: UNDEX near a free surface; cross-sectional plot of density and pressure along x = 0 at instants t = 1.2 ms using different grid resolutions.

5.2.3 2D cylindrical underwater explosion near a planar rigid wall.

This is a two-dimensional test case used to investigate the effect of shock loading and cavitation loading or reloading created by an underwater explosion on a nearby rigid structure, such as a ship's hull. This test case has been studied numerically by [94, 190, 99, 59] and also experimentally [202] in which an explosive placed in water is set off under a submerged plate. The physical properties (density, velocities, pressure, specific

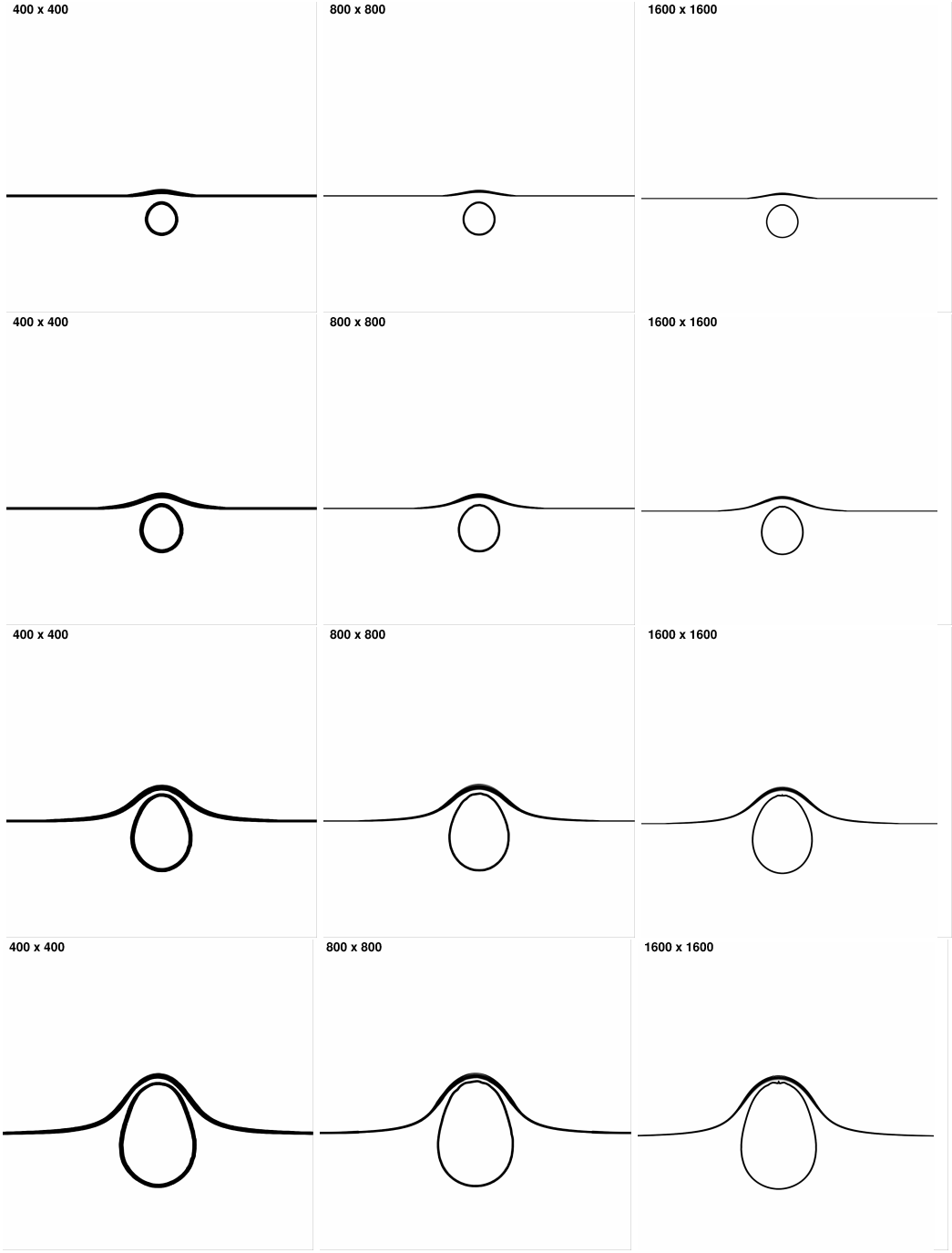

Figure 5.27: UNDEX near a free surface; density gradient contours at t = (0.2, 0.4, 0.8, 1.2)ms. Captured using CWENO4 schemes with different grids resolution. More inter-facial structures are sharper as the grid resolution increases.

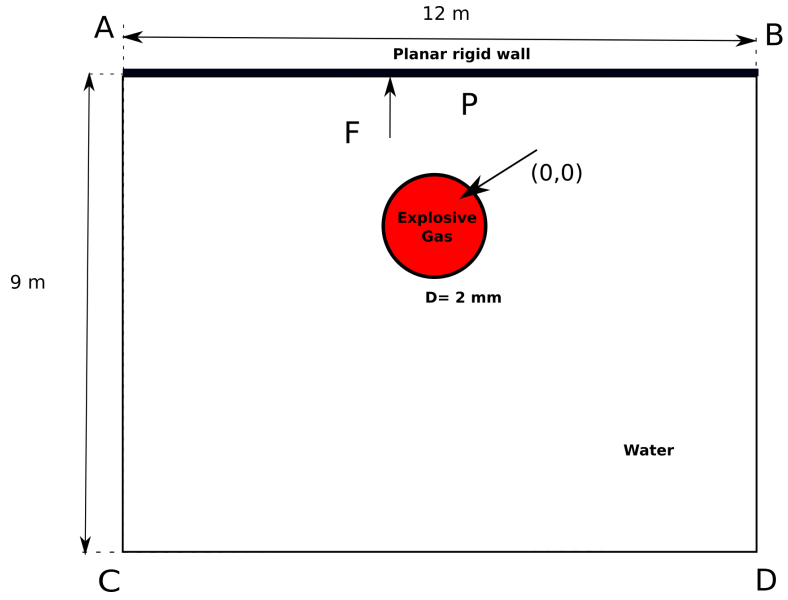

Figure 5.28: Computational domain setup for a two-dimensional underwater explosion near a planar rigid wall.

ratio, and volume fraction) of each fluid involved in these test cases are presented below:

$$(\rho, u, v, p, \gamma, \alpha) = \begin{cases} \left(1270, 0, 0, 8.29 \times 10^8, 2, 1\right), & \text{Explosive} \\ \left(1000, 0, 0, 10^5, 7.15, 0\right), & \text{Water} \end{cases} \tag{5.10}$$

The 2D computational domain (Fig. 5.28) is a rectangular area [-6, 6] x [-6, 3] m^2. Similarly to the previous test case, the explosive is modelled as a high-pressure air bubble. A spherical gas bubble of a diameter of 1 m is placed in water at the origin [0,0]. A rigid wall is fixed at y = 3 m above the bubble, and P is the centre point of the planar wall, where a numerical sensor is placed to identify the load on the wall. The rigid wall boundary conditions has been configured as reflecting, as defined in section 4.0.1. The domain's left, right, and bottom surfaces are prescribed as non-reflecting, as defined in section 4.0.2. Using a coarse grid to discretize the domain, the final time of the simulation has been selected as t = 100 ms.

The 4th-order CWENO scheme is also employed for this test problem using the 5-equation diffuse interface model. To circumvent the non-physical pressure values (i.e.,

$p < 0$) obtained at cavitation regions during the explosion as described by authors [147, 201, 31, 59] who have studied the same test case, the cut-off model detailed previously in Section 5.2.1 is used to keep the pressure at 5000 Pa. Contour plots of pressure obtained using the 4th-order CWENO scheme at different instants of the explosion are presented in Fig. 5.29. From the contour plots, primary loading occurs as the pressurised air bubble explodes, shockwaves formed, hit the wall above it at time t = 1.5 ms, and immediately reflect into the water. The density falls dramatically. Rarefaction can be seen in Fig. 5.29 at t = 2 ms, when the pressure drops around the wall, forming a low-pressure region (t = 3 ms). This pressure drops rapidly, making a cavitation region around the wall at t = 4 ms and t = 5.3 ms, respectively. The cavitation collapses and creates a load on the wall, this is known as cavitation collapse reloading (secondary reloading). As seen in the plot of the pressure history of the wall along the horizontal axis in Fig. 5.30, the first instance of peak pressure created by the shockwaves is 6200 MPa for the Allaire et al. and 6400 MPa for the Kapila et al. diffuse interface models. This demonstrates that the Allaire et al. and Kapila et al. models have a satisfactory agreement with the results of other authors [190, 99, 59]. As the bubbles expand further, the cavitation mentioned previously collapses, creating a reloading impact on the wall with a second peak pressure of 720 MPa for Allaire's et al.'s model and 760 MPa for Kapila et al.'s model. It should be noted that although the impact of the shock loading is much higher than that of the cavitation reloading, the duration of the cavitation reloading is much longer, thereby making the loading substantial.

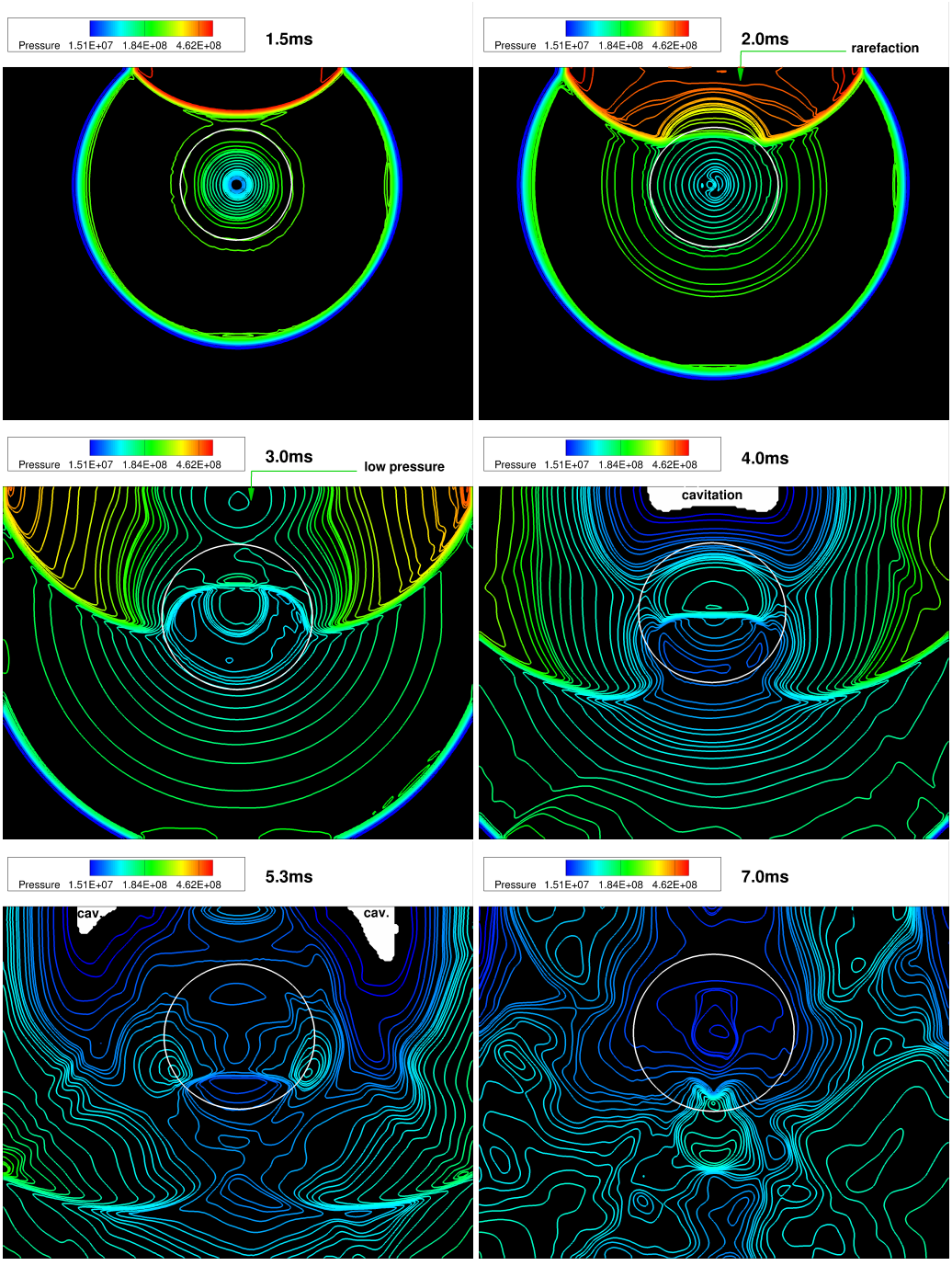

Figure 5.29: UNDEX near a rigid wall; the pressure contours at different instants. Captured using CWENO3 scheme with medium grid resolution. At very low pressure, cavitation can be noticed at time t = 4 ms and 5.3 ms near the rigid walls

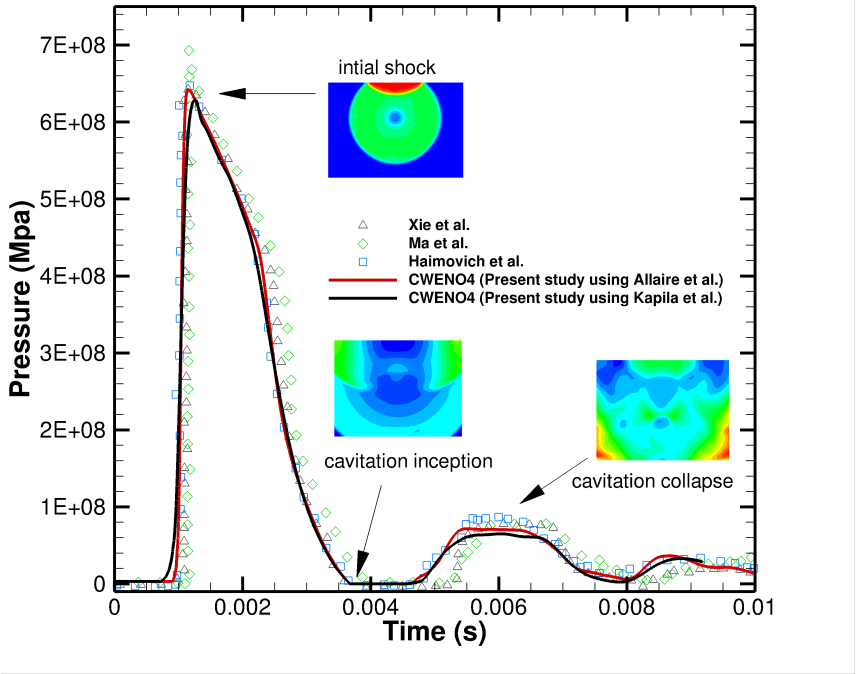

Figure 5.30: UNDEX near a rigid wall; plots of pressure history for the underwater explosion near a planar rigid wall at the center location of the upper wall obtained with CWENO4 schemes, and compared with other published results [59, 99, 189].

5.2.4 3D underwater explosion in an enclosed, rigid cylindrical wall.

In an experiment by Wardlaw et al. [184], an explosive is placed and exploded in the middle of an enclosed cylindrical tank half-filled with water at atmospheric pressure. This test case is used to study the effect of explosion damage in an enclosed space like a closed tank . The explosive is modelled as a pressurised gas bubble to investigate this numerically, just like in the previous test cases above. This test case has been investigated numerically by various researchers [99, 190, 94, 201, 68, 147, 71]. It is an ideal test problem for shock and cavitation responses in enclosed structures. The initial conditions for this problem follow Xie et al. [185] and are presented below.

$$(\rho,u,v,p,\gamma,\alpha) = \begin{cases} (1770,0,0,2\times 10^9,2,1), & \text{Explosive} \\ (1000,0,0,10^5,7.15,0), & \text{Water.} \end{cases} \tag{5.11}$$

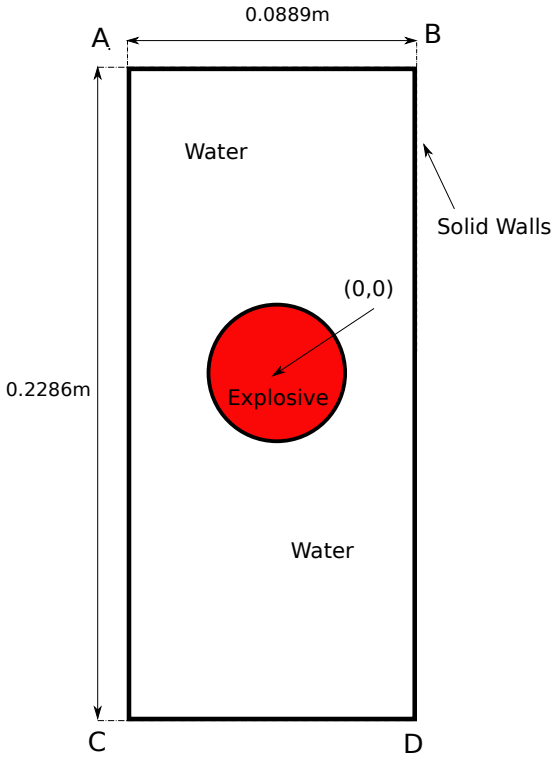

Figure 5.31: Computational domain setup for the three-dimensional underwater explosion in a rigid cylinder.

The initial geometry of this test case is shown in Fig. (5.31) which follows that of Xie et al.[190, 185].

The explosive/gas bubble diameter is 0.1 m, and it is placed in a cylindrical container with a height of 0.2286 m and a width of 0.0889 m. The water is partially contaminated with 15 % air. This test case can be modelled in two-dimensional axisymmetric form, i.e., in the cylindrical coordinate system, or in three-dimensional form. In our case, the test is carried out on a three dimensions.

Reflecting boundary conditions are prescribed for all the surfaces, and a quadrilateral mesh discretizes the domain with approximately 0.5 million cells. A CWENO4 scheme is employed, and the simulation is run until t = 120μs. From the pressure contour in Fig. (5.35) showing the time evolution of the bubble, it can be noticed that as the bubble explodes and expands, it creates shock-waves that hit the cylinder's side walls at t = 15 μs. The waves are immediately reflected into the water, striking the expanding bubble at t = 30 s. The density rapidly changes, and rarefaction occurs. At t = 45 μs, the bubble

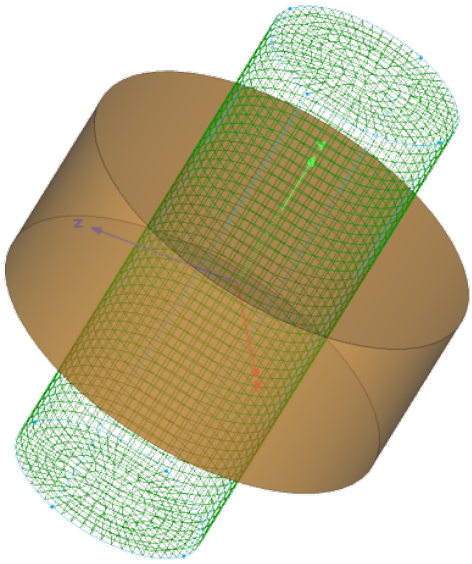

Figure 5.32: Mesh strategy of the fluid domain for three-dimensional cylindrical underwater explosions zone

transforms into an oval shape. As time evolves, a very low-pressure region around the bubble and close to the centre of the lateral walls is observed at t = 30 µs leading to cavitation at t = (45, 60, and 70)µs as seen in Fig. (5.35).

The cavitation collapses violently, creating reloading pressure on the walls of the cylinder. As seen in Fig. (5.34), cavitation as a secondary source of loading or reloading can significantly impact an enclosed structure, with effects even closer to those obtained by the primary shock-wave loading.

According to the pressure history plot in Fig. 5.34, the initial peak pressure from the simulation that uses the Allaire et al. diffuse interface methods is 6600 MPa. The value is much closer to Wardlaw et al.'s [184] experimental result, where p = 6300 MPa. Shyue et al. [147] and Ying et al. [193] used the Allaire et al. diffuse interface methods in conjunction with the cut-off cavitation models and obtained numerical values in the range of 7000–7200 MPa, respectively.The cavitation collapse produces the second impact at a time of 90 µs, which is significant and has a value of P = 2100 MPa, which is lower than the numerical results of Shyue et al. [147] and Ying et al. [193] but closer to the experimental value than the latter. The result of Chen [23] where Smoothed Particle

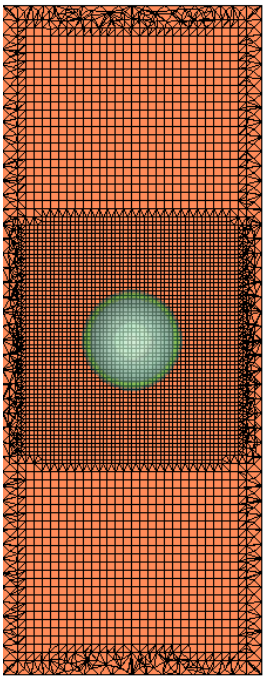

Figure 5.33: Corresponding mesh refinement for simulation. zone.

Hydrodynamics SPH models were employed has a delay in the cavitation collapse and reload because THE Schmidt model [189, 140, 185] was used and not the cut-off model as in our study.

Numerical results showing a 3D bubble-wall interaction in Fig. A.2 show the bubble's isosurface changing from a spherical to an oval shape with the density and pressure fields on the central cross-sections representing the moving interface. This study has further demonstrated and agreed with other authors [185, 189, 99] that cavitation collapse reloading also has a comparable damaging effect on an enclosed structure as that of shock loading, despite the fact that shock loading is frequently regarded as the primary damage source.

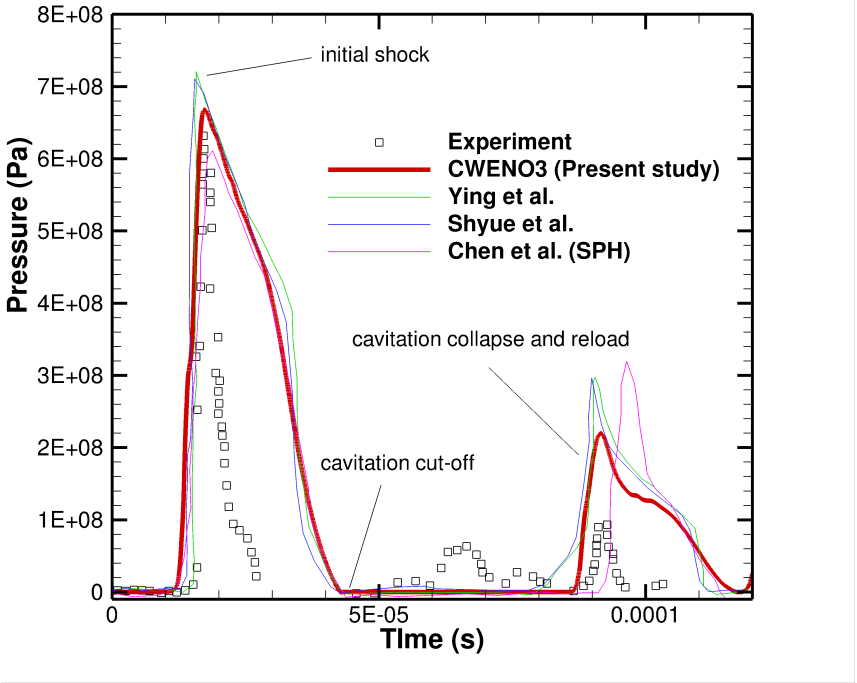

Figure 5.34: Underwater explosion in an enclosed cylindrical container; plots of pressure history (at the centre location of the left wall) for the underwater explosion in an enclosed cylindrical wall with CWENO4 schemes, and compared with other published results. [24, 147, 193]

5.2.5 2D underwater explosion of two bubbles placed horizontally near a free surface

To investigate the effect of charge separation distance on cavitation, two charges are positioned horizontally adjacent to one another near a free surface in a two-dimensional setup. Two identical bubbles ($d = 0.24$ m) are located at $H_o = 0.3$ m below the free surface, separated by L_o. The numerical setup is similar to that of Jun Yu et al.'s in [196]. The selected L_o distances between the two bubbles are $(0.3, 0.5, 0.7, 0.9)$ m, respectively. For comparative purposes, a single charge similar to that employed in Test case 5.2.2 is also simulated using the same computational parameters and dimension. All of the surfaces have outflow boundary conditions as defined in section 4.0.4, and the domain is discretized using a quadrilateral mesh with about 0.04 million cells. For this test example, a medium mesh is employed to save computing costs. The simulation is carried out using

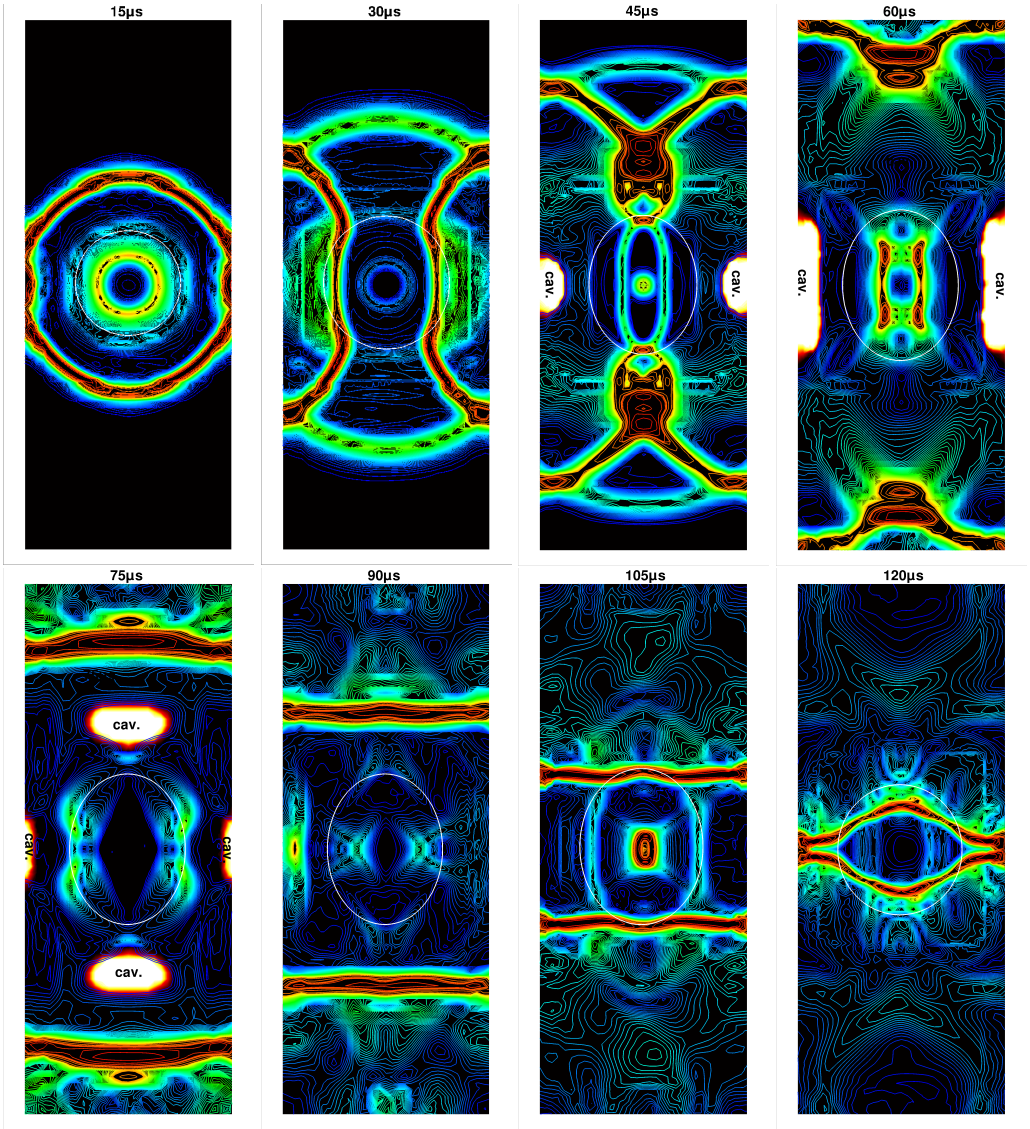

Figure 5.35: UNDEX in an enclosed cylindrical container; pressure gradient contours for the 3D underwater explosion in an enclosed, rigid cylindrical wall. Captured using CWENO3.

a CWENO4 scheme and the time for the simulation is $t = 12$ ms.

The physical characteristics of each fluid used in these test cases, including density, velocity, pressure, specific ratio, and volume fraction, are outlined below:

$$(\rho, u, v, p, \gamma, \alpha) = \begin{cases} (1270, 0, 0, 8.29 \times 10^8, 2, 1), & \text{Explosive} \\ (1000, 0, 0, 10^5, 7.15, 0), & \text{Water.} \end{cases} \tag{5.12}$$

For inter-bubble lengths ranging from (0.3-0.9) m, the volume fraction contours shown

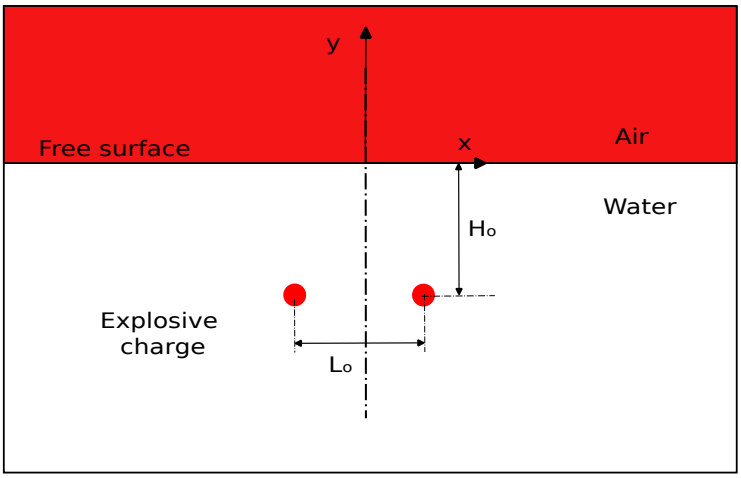

Figure 5.36: Computational domain setup for the two-dimensional underwater explosion of two bubbles placed horizontally near a free surface.

in Fig. 5.38 is utilised to efficiently illustrate the evolution of the free surface's centre at various instants. The height of the centre of the free surface continuously decreases for the same instant as separation distances increases from $L_o = (0.3 - 0.9)$ m. In same Fig. 5.38, the bubble expands and coalesces or merges for smaller inter-bubble distances $L_o = (0.3, 0.4)$ m, increasing the energy intensity on the free surface.

The two bubbles explode, just as in earlier UNDEX test cases, creating a shock wave that travels through the water and interacts with the bubbles. The size and the distance between the bubbles in a two-bubble explosion are two factors that can affect the cavitation that forms under the free surface. In the plot of pressure-time history at the centre of the explosion at location (0.0, -0.03)m in Fig. 5.37, the peak pressure caused

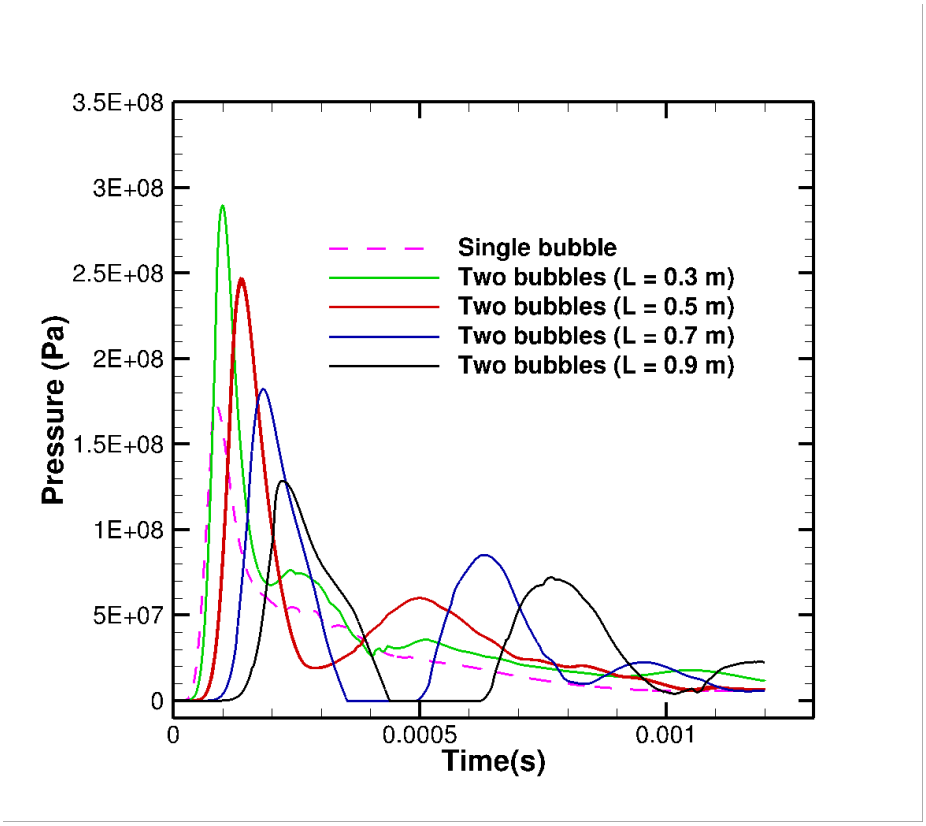

Figure 5.37: Underwater explosion two bubbles placed horizontally near a free surface; plots of pressure history (at the centre location of the left wall) for the underwater explosion in an enclosed cylindrical wall with CWENO4 schemes, and compared with other published results. [24, 147, 193]

by the primary loading for a single bubble is shown as 170 MPa and 290 MPa for the two-bubble case with the largest inter-bubble distance of $L_o = 0.9ms$, 1.7 times more that of the single bubble. Additionally as seen in Fig. 5.37, the peak pressure increases as the inter-bubble distance decreases from the largest ($L_o = 0.9$) m to the smallest ($L_o = 0.3$ m) i.e the largest loading is with the smallest inter-bubble distance. The cavitation collapse of the two charges or bubbles creates a secondary reloading which gets delayed as the inter-bubble distance increases. The peak pressure created by the cavitation reloading is more noticeable for the two bubbles than for the single bubble. This goes to further explain that more structural damage due to cavitation can be caused by two bubbles than by a single bubble. For very small inter-bubble distances between two charges, such as $L_o = 0.3$ m , the cavitation reloading is very small, which is due to the fact that the bubbles coalesce and merge easily into a larger bubble, reducing the number of potential cavitation bubbles

and potentially decreasing the overall cavitation damage.

Fig. 5.39 presents the pressure gradient contour for the single bubble and two-bubble cases. The pressure gradients varies depending on the inter-bubble distance, a high-pressure zone near the bubble(s) can be seen in the contour and a lower pressure zone further away.

5.2.6 3D Underwater of two bubbles placed vertically in an enclosed region.

To investigate the effect of vertical separation distance on bubble interaction during underwater explosion within a confined region, two identical bubbles, each with a diameter of 0.24 m, are placed vertically one above the other at 0.3 m below the free surface of the water, with a separation distance denoted as H_o.

The computational set up is similar to that employed in test case 5.2.4. The H_o distances between the two bubbles are chosen to be $(0.3, 0.5, 0.7, 0.9)$m. For the sake of comparison, we also conducted simulations involving a single bubble of same diameter, utilizing the same computational set up. The reflective boundary conditions, as described in Section 4.0.1, is applied to all surfaces. The computational domain is discretized using a quadrilateral mesh containing approxi-mately 0.4 million cells, with a medium mesh resolution chosen to reduce computational cost. The simulations is carried out using a CWENO4 scheme, and the total simulation duration was set to $t = 12ms$.

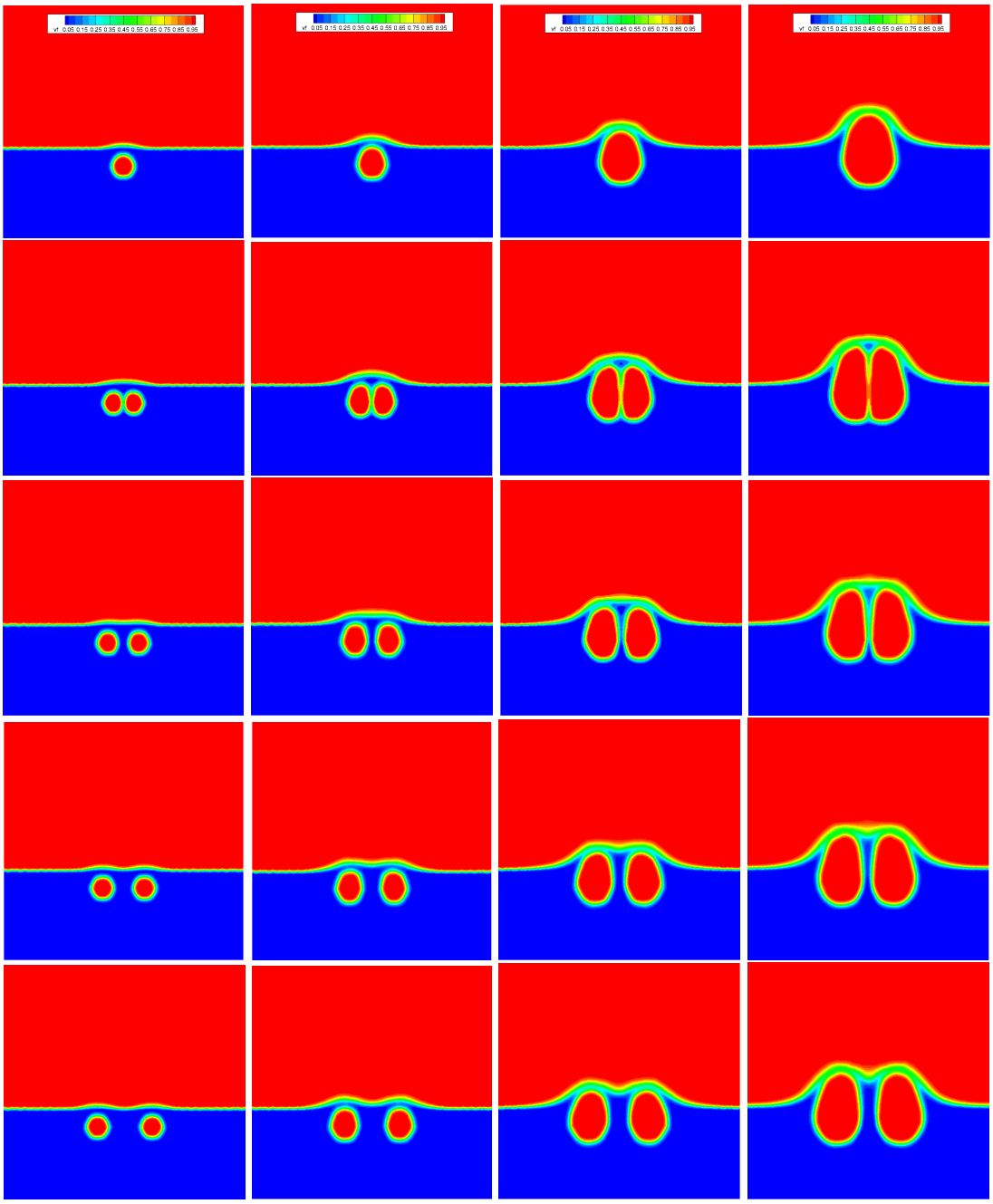

Figure 5.38: UNDEX of two bubbles placed horizontally near a free surface; contour of volume fraction using a CWENO4 scheme on a medium mesh at t=(0.2, 0.4, 0.8 and 1.2)ms for inter-bubble lengths of (0.3, 0.5, 0.7 and 0.9) m respectively.

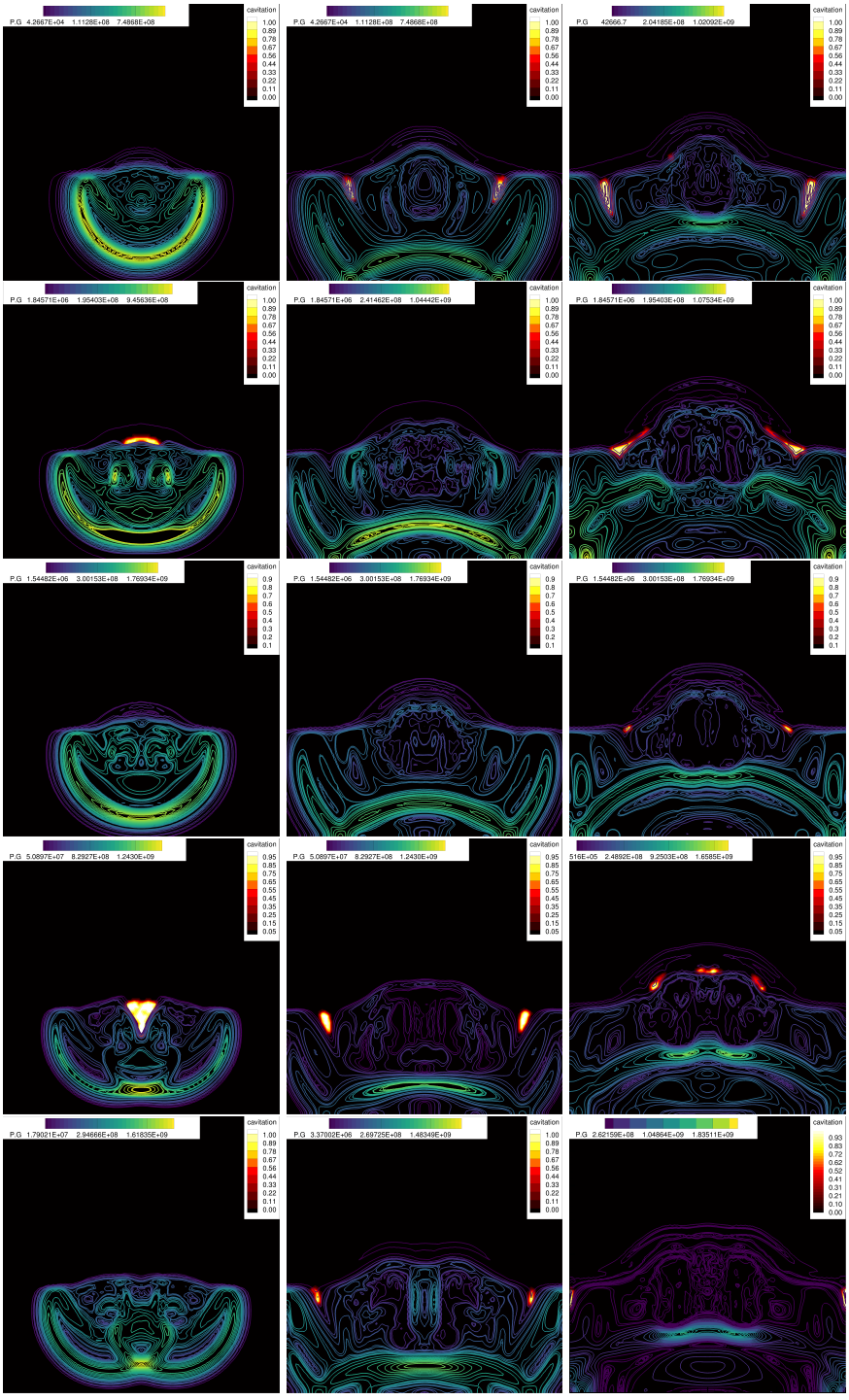

Figure 5.39: UNDEX of two bubbles placed horizontally near a free surface; contour of pressure gradient for the single bubble (Top) and the two-bubbles cases subsequently below for inter-bubble lengths of (0.3, 0.5, 0.7 and 0.9) m respectively using a CWENO4 scheme on a medium mesh at t=(0.4, 0.8 and 1.06)ms. The red-yellow areas are cavitation zones.

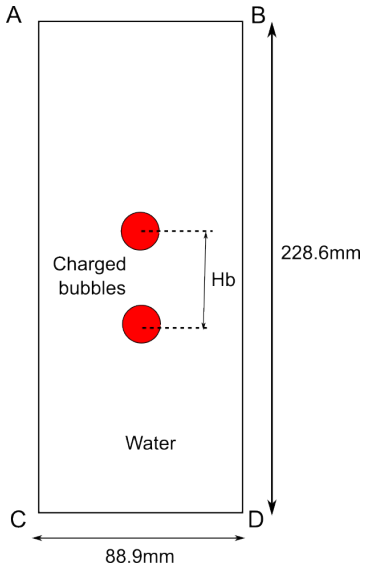

Figure 5.40: Computational domain setup for the three-dimensional underwater of two bubbles placed vertically in an enclosed region

$$(\rho, u, v, p, \gamma, \alpha) = \begin{cases} (1.225, 0, 0, 1.57 \times 10^7, 2.0), & \text{Air bubble} \\ (998.2, 0, 0, 10^5, 7.15, 0), & \text{Water.} \end{cases} \tag{5.13}$$

The volume fraction contour depicted in Fig. 5.42 is for the the shortest distance between the bubbles, which is H_b, =15 mm. From the contour, as the explosion progresses over time, the water film separating the two interacting gaseous bubbles gradually thins out. The presence of surface tension forces draws the bubbles closer together until the thin film ruptures, leading to the merger of the two bubbles into a single, larger bubble.

In Fig. 5.41, a pressure history plot is depicted showing the pressure at the center of the left wall for the three inter-bubble distances (H_b = 15, 30, and 60 mm). A closer look at the pressure gradient contours in Fig. 5.43, shows that cavitation regions are most pronounced when the inter-bubble distance is shortest, at $H_b = 15$ mm, across varying time intervals (t = 1.54, 6, 30, 60, and 90 µs). These cavitation zones, as depicted in the same Fig. 5.43, are primarily concentrated along the cylinder's walls and in the vicinity of the bubbles.

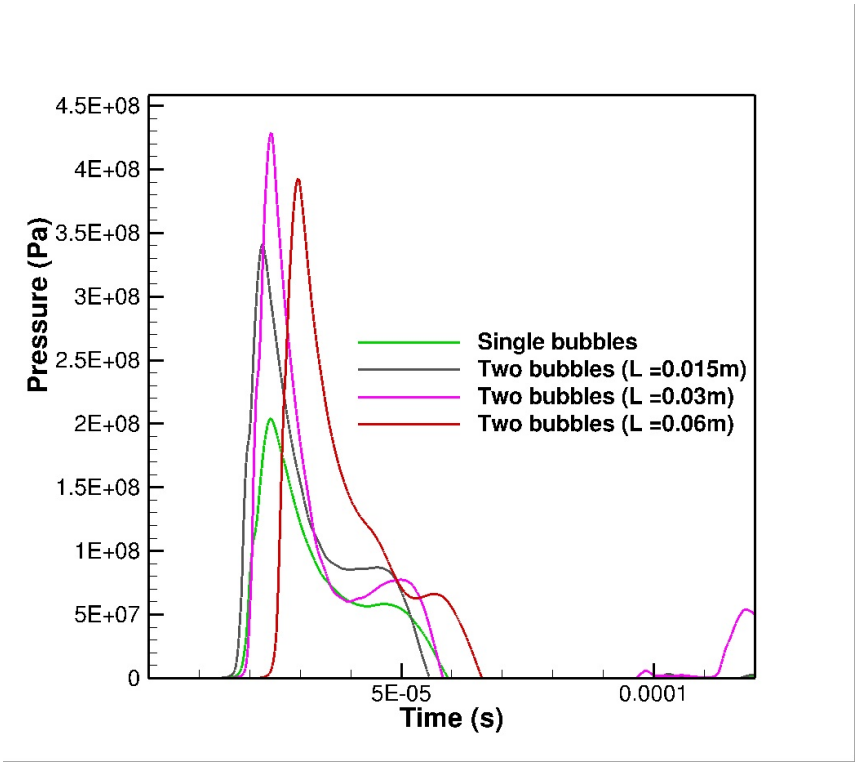

Figure 5.41: Underwater explosion of two bubbles vertically placed in an enclosed region; plots of pressure history (at the centre location of the left wall) for the underwater explosion in an enclosed cylindrical wall with CWENO4 schemes for inter-bubble lengths of (15, 30, and 60) mm

.

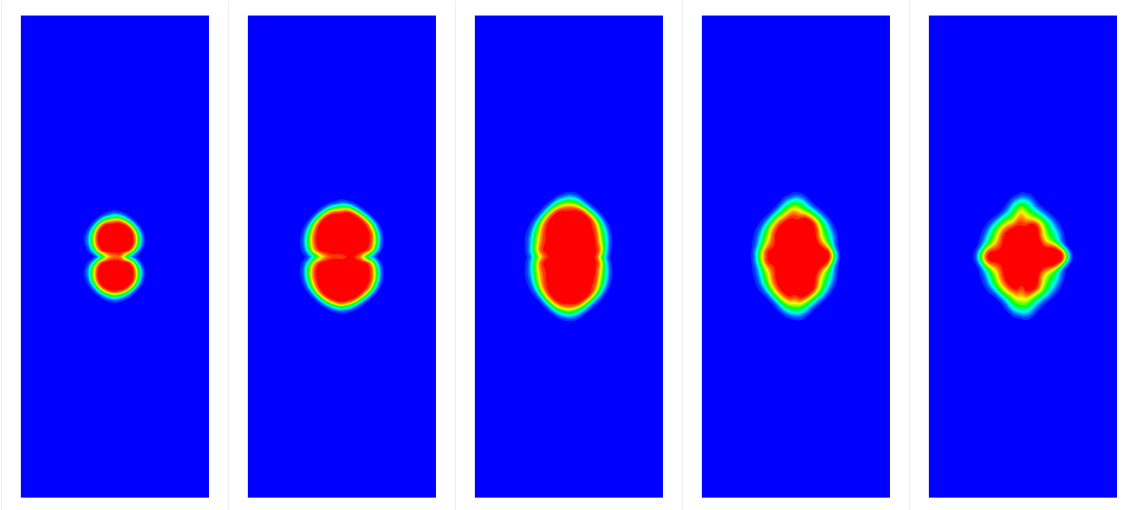

(a) $t = 10\mu s$ (b) $t = 30\mu s$ (c) $t = 60\mu s$ (d) $t = 90\mu s$ (e) $t = 120\mu s$

Figure 5.42: Underwater explosion of two bubbles vertically placed in an enclosed region; volume fraction contours for the 3D underwater explosion in an enclosed for $H_b = 30$ mm, rigid cylindrical wall.Captured using CWENO4. The green-yellow areas shows the interface between water and explosive. The two bubbles eventually merge into a single larger bubble.

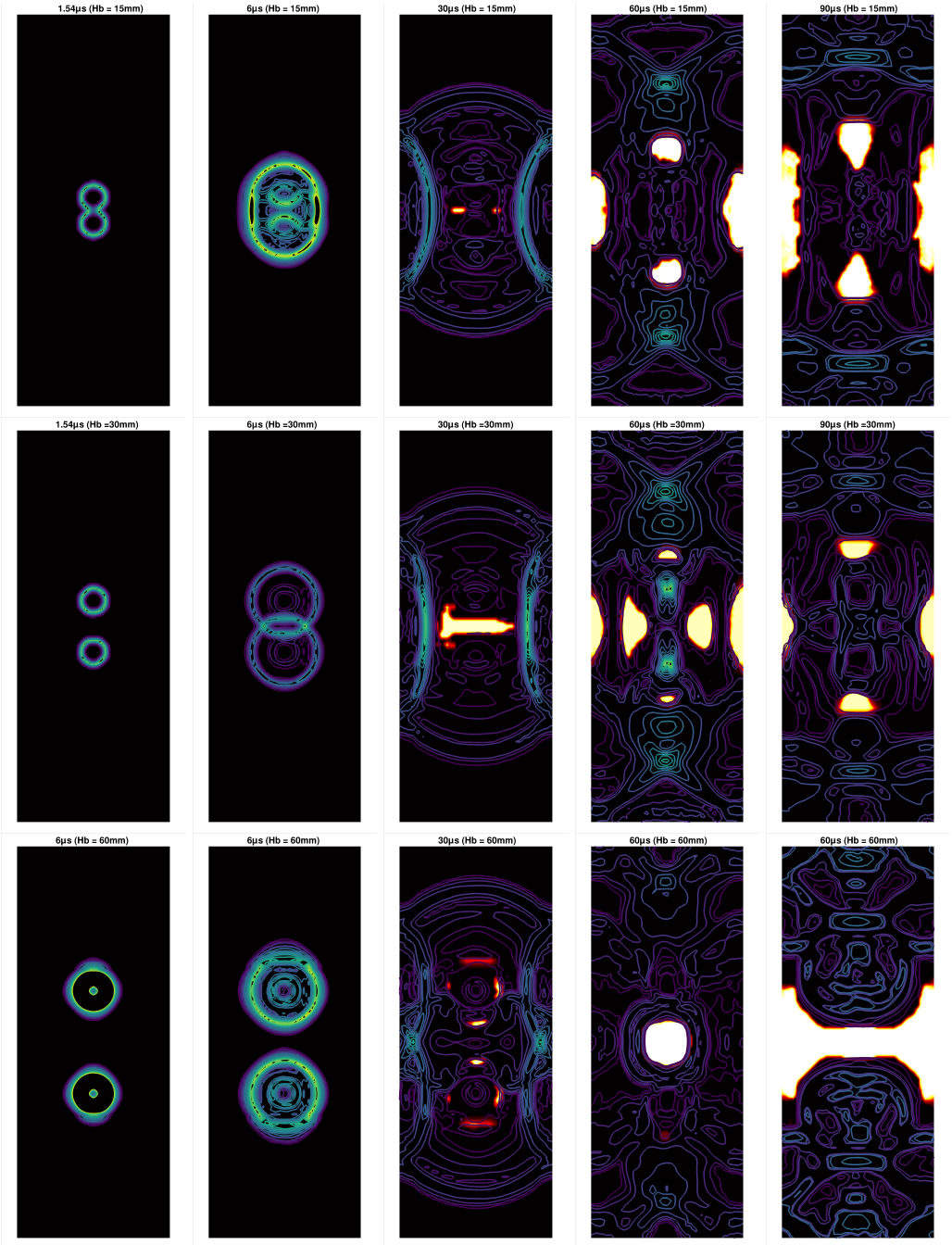

Figure 5.43: Underwater explosion of two bubbles vertically placed in an enclosed region; pressure gradient contours for the 3D underwater explosion in an enclosed rigid cylindrical wall with three different inter - bubble distances: H_b= 15 mm(Top), 30 mm(Middle), 60 mm(Bottom) for varying time frames t = (1.54, 6, 30, 60 and 90) µs. Captured using CWENO4. The white-red-yellow areas are cavitation zones, the red regions are indicative of potential high cavitation activity.

Table 5.4: Summarised overview of the test cases, their purposes for this research and the key findings.

Application in first series of test cases (Test Cases I)		
Test cases	**Use**	**Key findings**
1. Multi-species advection convergence study.	To verify the intended spatial accuracy of the computational methods.	The schemes achieved their designed order of convergence.
2. Advection of contact discontinuity.	To test the convergence and non-oscillatory characteristics of our numerical scheme.	The CWENO scheme with primitive variables provides the correct solution with no oscillations.
3. Gas bubble in water.	To assess the performance of various numerical methods.	Results gotten are within the range obtained from the other studies [104, 55].
4.Shock-Helium bubble interaction .	-For evaluating the performance of various methods used for multicomponent flow.	Results and experimental findings by Haas and Sturtevant are in good agreement [58].

Table 5.5: Summarised overview of the test cases involving cavitation, their use and key findings from this research

Application in Cavitation cases (Test Cases II)		
Test cases	**Use**	**Key findings**
1. Underwater explosion near a planar wall.	For studying how nearby rigid structures are affected by shock loading, cavitation loading, or reloading.	The cut-off single fluid model is efficient for UNDEX. Results are in agreement with other authors [147, 201, 31, 59].
2. Underwater explosion near a free surface.	To investigate the bubble dynamics at the material interface	The results are consistent with the published results of [99, 10, 147].
3. Underwater explosions in a rigid cylinder.	This test case is used to study the effect of explosion damage in an enclosed space like a closed tank.	Results are similar to that obtained in the experimental works of [184] , and numerical results of [189, 193, 147, 185].
4. Underwater of two bubbles near a free surface.	To investigate the effect of charge separation distance on cavitation.	Results shows more structural damage due to cavitation can be caused by two charged bubbles than by a single bubble.
5. Underwater of two bubbles placed vertically in an enclosed region.	To investigate the effect of vertical separation distance on cavitation during underwater explosion within a confined region.	Results shows hows that cavitation regions are most pronounced when the inter-bubble distance is shortest.

Chapter 6

Conclusions and Recommendations

6.1 Conclusions

In summary, this thesis research has developed a novel and efficient high-order approach for simulating multi-material/phase and multiphysics flow. This new method extends the use of unstructured high-order finite-volume central weighted essentially non-oscillatory (CWENO) schemes to simulate multicomponent flows within the interface-captu-ring framework. The key contributions of this research can be summarised as follows: The developed CWENO interface capturing high-order scheme offers high-order accuracy in smooth regions while maintaining stability and oscillation-free solutions in regions with sharp material interfaces and discontinuities. This enables the accurate representation of discontinuities in multiphase or multi-component flows without the spurious oscillations typically observed at material boundaries. This capability **substantially improves the accuracy and reliability of simulating multiphase/ multi-component flows**.

A better representation of the physical phenomena of multiphase flow is also made possible by the CWENO interface capturing high-order scheme's capacity to offer a **sharp and high-resolution description of moving material interfaces** by minimising the artificial smearing frequently found in other numerical methods used for two-phase compressible flow simulations. It achieves this without the need for additional interface sharpening,

compression techniques, or anti-diffusive schemes, which are commonly employed to counteract numerical diffusion and maintain interface sharpness during simulations. By eliminating the need for additional interface sharpening, compression techniques, or anti-diffusive schemes, it streamlines simulation process leading to faster and more efficient computational workflows. This offers a **simplicity, and a significant efficiency by the reduction in computational cost.**

The contributions presented in this thesis lay a strong foundation for future research in this field, opening new possibilities and innovative approaches. The versatility of the CWENO high-order diffuse interface models on unstructured meshes makes them applicable to a wide range of compressible multiphase flows, including applications in aerospace engineering, combustion, and medical science.

6.2 Recommendation

Although the project's objectives have been fulfilled, there are still some aspects that need to be further researched in order to advance the use of high-order interface capturing numerical methods for compressible multiphase flow simulations using unstructured meshes. The following list of potential extensions can serve as a foundation for future research in this field.

- At present, the UCNS3D, an open-source high-order unstructured compressible flow solver employed in this research, lacks a dynamic overset body-fitted grid technique. This limitation significantly hinders its adaptability, especially when conducting compressible multiphase simulations involving fluids' interaction with moving objects. Notably, cases involving arbitrary motions of objects in fluid, such as those of oblique water entry of high-speed projectiles; ricochet and penetration during water entry of bodies which significantly impact the underwater ballistic trajectory, are examples of cases that could not be explored due to this limitation. These test cases held substantial potential to contribute valuable insights to our

research.

- This research can be extended and applicable to micro-structured complex fluids, including non-Newtonian fluids and elastic-plastic materials. While the focus of the method used in the thesis is on Newtonian fluids, the numerical method developed in this study has the potential to be utilized in investigations involving the complex behavior of non-Newtonian flows and elastic-plastic materials, such as polymer flows. For instance, in the context of 3-D manufacturing, where it is crucial to accurately predict the melt flow front and cavity pressure in order to reduce residual stress during the injection-compression molding process of compressible polymers, a highly precise numerical algorithm is essential. The complexity of the melt flow process within a closed cavity makes it challenging to observe directly through experiments, which is why experimental setups are often avoided. Typically, the volume-of-fluid method with a fixed mesh is a common numerical approach used for such simulations [200]. However, a research aimed at leveraging the advantages of CWENO high-order diffuse interface models on unstructured meshes, particularly the simplicity it offers in extending to three dimensions can be used to address the limitations associated with the volume-of-fluid method, as discussed in the literature review chapter of this thesis.

- Additional research avenues may involve the integration of more intricate physics into the CWENO high-order diffuse interface models. Currently, the scope of this thesis work is confined to fundamental physics, primarily focusing on diffusion and advection. By expanding the incorporation of complex physics phenomena, such as reactive fluid mixtures, electrostatics, and magnetohydrodynamics, we can broaden the applicability of diffuse interface models to encompass a wider array of physical systems. This expansion will allow for a more comprehensive exploration of the numerical method's capabilities, pushing it to its full potential.

References

[1] U. J. F. Aarsnes, T. Flåtten, and O. M. Aamo. Review of two-phase flow models for control and estimation. *Annual Reviews in Control*, 42:50–62, 2016.

[2] E. Adebayo, P. Tsoutsanis, and K. Jenkins. Implementation of cweno schemes for compressible multicomponent/multiphase flow using interface capturing models. *8th European Congress on Computational Methods in Applied Sciences and Engineering*, 2022.

[3] C. Alexandre, B. Pierre, and S. Richard. A simple and fast phase transition relaxation solver for compressible multicomponent two-phase flows. *Computers & Fluids*, 150:31–45, 2017.

[4] G. Allaire, S. Clerc, and S. Kokh. A five-equation model for the simulation of interfaces between compressible fluids. *Journal of Computational Physics*, 181(2):577–616, 2002.

[5] A. Ambroso, C. Chalons, and P. A. Raviart. A Godunov-type method for the seven-equation model of compressible two-phase flow. *Computers and Fluids*, 54(1):67–91, 2012.

[6] D. M. Anderson, G. B. McFadden, and A. A. Wheeler. Diffuse-interface methods in fluid mechanics. *Annual Review of Fluid Mechanics*, 30(1):139–165, 1998.

[7] N. Andrianov. *Analytical and numerical investigation of two-phase flows*. PhD thesis, Otto-von-Guericke-Universität Magdeburg, 2003.

[8] N. Andrianov, R. Saurel, and G. Warnecke. A simple method for compressible multiphase mixtures and interfaces. *International Journal for Numerical Methods in Fluids*, 41:109 – 131, 2003.

[9] N. Andrianov and G. Warnecke. The Riemann problem for the Baer-Nuziato two-phase flow model. *Journal of Computational Physics*, 195(2):434–464, 2004.

[10] M. Ansari and A. Daramizadeh. Numerical simulation of compressible two-phase flow using a diffuse interface method. *International Journal of Heat and Fluid Flow*, 42:209–223, 2013.

[11] A. Antoniadis, P. Tsoutsanis, and D. Drikakis. High-order schemes on mixed-element unstructured grids for aerodynamic flows. *42nd AIAA Fluid Dynamics Conference and Exhibit*, 2012.

[12] A. Antoniadis, P. Tsoutsanis, and D. Drikakis. Numerical accuracy in rans computations of high-lift multi-element airfoil and aircraft configurations. *53rd AIAA Aerospace Sciences Meeting*, 2015.

[13] A. Antoniadis, P. Tsoutsanis, Z. Rana, I. Kokkinakis, and D. Drikakis. Azure: An advanced cfd software suite based on high-resolution and high-order methods. *53rd AIAA Aerospace Sciences Meeting*, 2015.

[14] A. F. Antoniadis, D. Drikakis, P. S. Farmakis, L. Fu, I. Kokkinakis, X. Nogueira, P. A. Silva, M. Skote, V. Titarev, and P. Tsoutsanis. Ucns3d: An open-source high-order finite-volume unstructured cfd solver. *Computer Physics Communications*, 279:108453, 2022.

[15] S. Arabi, J.-Y. Trépanier, and R. Camarero. A simple extension of roe's scheme for multi-component real gas flows. *Journal of Computational Physics*, 388:178–194, 2019.

[16] P. A.S.F. Silva, P. Tsoutsanis, and A. Antoniadis. Numerical investigation of full helicopter with and without the ground effect. *Aerospace Science and Technology*, 122, 2022.

[17] M. Baer and J. Nunziato. A two-phase mixture theory for the deflagration-to-detonation transition (ddt) in reactive granular materials. *International Journal of Multiphase Flow*, 12(6):861–889, 1986.

[18] A. Bayliss and E. Turkel. Radiation boundary condition for wave-like equations. *Communications on Pure and Applied Mathematics*, 33:707 – 725, 11 1980.

[19] R. Berry, R. Saurel, F. Petitpas, E. Daniel, O. Métayer, S. Gavrilyuk, and N. Dovetta. Progress in the development of compressible, multiphase flow modeling capability for nuclear reactor flow applications. *Idaho National Laboratory*, pages 1–215, 2008.

[20] J. Blazek. *Computational Fluid Dynamics: Principles and Applications (Third Edition)*. Butterworth-Heinemann, Oxford, third edition, 2015.

[21] C. Brennen. *Cavitation and Bubble Dynamics*, volume 44. Cambridge University Press, 01 2013.

[22] J. W. Cahn and J. E. Hilliard. Free energy of a nonuniform system. iii. nucleation in a two-component incompressible fluid. *The Journal of Chemical Physics*, 31(3):688–699, 1959.

[23] L. Cheng, X. Deng, B. Xie, Y. Jiang, and F. Xiao. Low-dissipation bvd schemes for single and multi-phase compressible flows on unstructured grids. *Journal of Computational Physics*, 428:110088, 2021.

[24] S. C.-W. Cheng Juan. High order schemes for cfd: A review. *Chinese Journal of Computational Physics*, 26(5):633–655, 2009.

[25] A. Chiapolino, R. Saurel, and B. Nkonga. Sharpening diffuse interfaces with compressible fluids on unstructured meshes. *Journal of Computational Physics*, 340:389–417, 2017.

[26] S. Chiocchetti, I. Peshkov, S. Gavrilyuk, and M. Dumbser. High order ader schemes and glm curl cleaning for a first order hyperbolic formulation of compressible flow with surface tension. *Journal of Computational Physics*, 426:109898, 2021.

[27] R. H. Cole. *Underwater Explosions*, volume 1. Dover Publications, 1965.

[28] F. Coquel, T. Gallouët, J.-M. Hérard, and N. Seguin. Closure laws for a two-fluid two-pressure model. *Comptes Rendus Mathematique*, 334(10):927–932, 2002.

[29] V. Coralic and T. Colonius. Finite-volume WENO scheme for viscous compressible multicomponent flows. *Journal of Computational Physics*, 274:95–121, 2014.

[30] F. A. Costanzo. Underwater explosion phenomena and shock physics. In T. Proulx, editor, *Structural Dynamics, Volume 3*, pages 917–938. Springer New York, 2011.

[31] A. Daramizadeh and M. R. Ansari. Numerical simulation of underwater explosion near air-water free surface using a five-equation reduced model. *Ocean Engineering*, 110:25–35, 2015.

[32] V. Deledicque and M. V. Papalexandris. An exact Riemann solver for compressible two-phase flow models containing non-conservative products. *Journal of Computational Physics*, 222(1):217–245, 2007.

[33] A. D. Demou, N. Scapin, M. Pelanti, and L. Brandt. A pressure-based diffuse interface method for low-Mach multiphase flows with mass transfer. *Journal of Computational Physics*, 448:110730, 2022.

[34] X. Deng, S. Inaba, B. Xie, K. M. Shyue, and F. Xiao. High fidelity discontinuity-resolving reconstruction for compressible multiphase flows with moving interfaces. *Journal of Computational Physics*, 371(March):945–966, 2018.

[35] S. Diot, S. Clain, and R. Loubère. Improved detection criteria for the multi-dimensional optimal order detection (mood) on unstructured meshes with very high-order polynomials. *Computers & Fluids*, 64:43–63, 2012.

[36] F. Dobran. *Theory of Structured Multiphase Mixtures*. Springer Berlin, Heidelberg, 2005.

[37] C. Domb, M. Green, and J. Lebowitz. *Phase Transitions and Critical Phenomena*. Phase Transitions and Critical Phenomena. Academic Press, 1972.

[38] S. L. Drew, Donald A.and Passman. Ensemble averaging. in: Theory of multicomponent fluids. *Applied Mathematical Sciences*, pages 92–104, 1999.

[39] M. Dumbser. Arbitrary high order non-oscillatory finite volume schemes on unstructured meshes for linear hyperbolic systems. *Journal of Computational Physics*, 221:693–723, 02 2007.

[40] M. Dumbser. Recent advances in high-order WENO finite volume methods for compressible multiphase flows. *AIP Conference Proceedings*, 1558:18–22, 2013.

[41] M. Dumbser, W. Boscheri, M. Semplice, and G. Russo. Central Weighted ENO Schemes for Hyperbolic Conservation Laws on Fixed and Moving Unstructured Meshes. *SIAM J. Sci. Comput.*, 39(6):A2564–A2591, 2017.

[42] M. Dumbser, M. Käser, V. A. Titarev, and E. F. Toro. Quadrature-free non-oscillatory finite volume schemes on unstructured meshes for nonlinear hyperbolic systems. *Journal of Computational Physics*, 226(1):204–243, 2007.

[43] R. E. Multiphase flow modeling based on the hyperbolic thermodynamically compatible systems theory. *AIP Conference Proceedings*, 1648, 2015.

[44] B. Einfeldt. On godunov-type methods for gas dynamics. *SIAM Journal of Numerical Analysis.*, 15:294–318, 09 1988.

[45] B. Einfeldt, P. L. Roe, C. D. Munz, and B. Sjogreen. On godunov-type methods near low densities. *Journal of Computational Physics*, 92(2):273–295, 02 1991.

[46] G. K. Elin Olsson and S. Zahedi. A conservative level set method for two phase flow. *Journal of Computational Physics*, 210(1):225–246, 2005.

[47] P. Farmakis, P. Tsoutsanis, and X. Nogueira. Weno schemes on unstructured meshes using a relaxed a posteriori mood limiting approach. *Computer Methods in Applied Mechanics and Engineering*, 363, 2020.

[48] V. Faucher, M. Bulik, and P. Galon. Updated VOFIRE Algorithm For Fast Fluid–structure Transient Dynamics with Multi-component Stiffened Gas Flows Implementing Anti-dissipation on Unstructured grids. *Journal of Fluids and Structures*, 74:64–89, 2017.

[49] T. FLåtten and H. Lund. Relaxation two-phase flow models and the subcharacteristic condition. *Mathematical Models and Methods in Applied Sciences*, 21(12):2379–2407, 2011.

[50] E. Franquet and V. Perrier. Runge-Kutta discontinuous Galerkin method for the approximation of Baer and Nunziato type multiphase models. *Journal of Computational Physics*, 231(11):4096–4141, 2012.

[51] D. Furfaro and R. Saurel. A simple hllc-type riemann solver for compressible non-equilibrium two-phase flows. *Computers & Fluids*, 111:159–178, 2015.

[52] J.-M. Ghidaglia and A. A. Mrabet. A regularized stiffened-gas equation of state. *Journal of Applied Analysis & Computation*, 8(3):675–689, 2018.

[53] J. W. Gibbs. On the equilibrium of heterogeneous substances. *American Journal of Science*, s3-16(96):441–458, 1878.

[54] M. B. Giles. Nonreflecting boundary conditions for euler equation calculations. *AIAA Journal*, 28:2050–2058, 1990.

[55] E. Goncalves, Y. Hoarau, and D. Zeidan. Simulation of shock-induced bubble collapse using a four-equation model. *Shock Waves*, 29(1):221–234, 2019.

[56] S. Gottlieb and C. Shu. Total variation diminishing Runge-Kutta schemes. *Mathematics of Computation*, 67(221):73–85, 1998.

[57] P. Gregorčič, R. Petkovšek, and J. Mozina. Investigation of a cavitation bubble between a rigid boundary and a free surface. *Journal of Applied Physics*, 102, 11 2007.

[58] J. F. Haas and B. Sturtevant. Interaction of weak shock waves with cylindrical and spherical gas inhomogeneities. *Journal of Fluid Mechanics*, 181:41–76, 1987.

[59] O. Haimovich and S. H. Frankel. Numerical simulations of compressible multicomponent and multiphase flow using a high-order targeted ENO (TENO) finite-volume method. *Computers and Fluids*, 146:105–116, 2017.

[60] F. H. Harlow and A. A. Amsden. Numerical calculation of almost incompressible flow. *Journal of Computational Physics*, 3(1):80–93, 1968.

[61] F. H. Harlow and A. A. Amsden. A numerical fluid dynamics calculation method for all flow speeds. *Journal of Computational Physics*, 8(2):197–213, 1971.

[62] A. Harten. High Resolution Schemes for Hyperbolic Conservation Laws. *Journal for Computational Physics*, 49(4):357–393, 1982.

[63] M. Hennessey, A. Kapila, and D. Schwendeman. An hllc-type riemann solver and high-resolution godunov method for a two-phase model of reactive flow with general equations of state. *Journal of Computational Physics*, 405:109180, 2020.

[64] M. T. Henry de Frahan, S. Varadan, and E. Johnsen. A new limiting procedure for discontinuous Galerkin methods applied to compressible multiphase flows with shocks and interfaces. *Journal of Computational Physics*, 280:489–509, 2015.

[65] C. W. Hirt and B. D. Nichols. Volume of fluid (VOF) method for the dynamics of free boundaries. *Journal of Computational Physics*, 39(1):201–225, 1981.

[66] P. C. Hohenberg and B. I. Halperin. Theory of dynamic critical phenomena. *Reviews of Modern Physics*, 49(3):435–479, 1977.

[67] M. Holt and N. J. Schwartz. Cavitation bubble collapse in water with finite density behind the interface. *The Physics of Fluids*, 6(4):521–525, 1963.

[68] Y. Hong, B. Wang, and H. Liu. Numerical simulation of compressible multiphase hydrodynamic problems using reduced five-equation model on body-fitted grids. *Computers and Fluids*, 233:105243, 2022.

[69] M. Ishii. A theory of nucleation for solid metallic solutions. *D.Se. thesis, Massachusetts Institute of Technology Cambridge*, pages 1–136, 1956.

[70] M. Ishii and K. Mishima. Two-fluid model and hydrodynamic constitutive relations. *Nuclear Engineering and Design*, 82(2):107–126, 1984.

[71] A. Jafarian and A. Pishevar. An exact multiphase Riemann solver for compressible cavitating flows. *International Journal of Multiphase Flow*, 88:152–166, 2017.

[72] E. Johnsen. On the treatment of contact discontinuities using WENO schemes. *Journal of Computational Physics*, 230(24):8665–8668, 2011.

[73] E. Johnsen and T. Colonius. Implementation of weno schemes in compressible multicomponent flow problems. *Journal of Computational Physics*, 219(2):715–732, 2006.

[74] E. Johnsen and F. Ham. Preventing numerical errors generated by interface-capturing schemes in compressible multi-material flows. *Journal of Computational Physics*, 231(17):5705–5717, 2012.

[75] E. Johnsen, J. Larsson, A. V. Bhagatwala, W. H. Cabot, P. Moin, B. J. Olson, P. S. Rawat, S. K. Shankar, B. Sjogreen, H. C. Yee, X. Zhong, and S. K. Lele.

Assessment of high-resolution methods for numerical simulations of compressible turbulence with shock waves. *Journal of Computational Physics*, 229(4):1213–1237, 2010.

[76] S. Jolgam, A. Ballil, A. Nowakowski, and F. Nicolleau. On equations of state for simulations of multiphase flows. In *Proceedings of the World Congress on Engineering*, volume 3, pages 1–6, 2012.

[77] M. Juan, R. Carlos, R. Gonzalo, F. Esteban, and R. Ángel. A discontinuous galerkin approximation for a wall–bounded consistent three–component cahn–hilliard flow model. *Computers & Fluids*, 225:104971, 2021.

[78] Y. Jun, P. Jian-qiang, W. Hai-kun, and M. Hai-bin. Application of compressible multi-component flow in underwater explosion problems. *Procedia Engineering*, 126:339–343, 2015.

[79] A. K. Kapila, R. Menikoff, J. B. Bdzil, S. F. Son, and D. S. Stewart. Two-phase modeling of deflagration-to-detonation transition in granular materials: Reduced equations. *Physics of Fluids*, 13(10):3002–3024, 2001.

[80] V. Kedrinskii. Negative pressure profile in cavitation zone at underwater explosion near free surface. *Acta Astronautica*, 3(7):623–632, 1976.

[81] H. Kleine, S. Tepper, K. Takehara, T. Etoh, and K. Hiraki. Cavitation induced by low-speed underwater impact. *Shockwaves*, 2:895–900, 2009.

[82] S. Kokh and F. Lagoutière. An anti-diffusive numerical scheme for the simulation of interfaces between compressible fluids by means of a five-equation model. *Journal of Computational Physics*, 229(8):2773–2809, 2010.

[83] I. Kokkinakis, A. Antoniadis, D. Drikakis, P. Tsoutsanis, and Z. Rana. High-order methods for hypersonic shock wave turbulent boundary layer interaction.

20th AIAA International Space Planes and Hypersonic Systems and Technologies Conference, 2015, 2015.

[84] C. Kong. *Comparison of Approximate Riemann Solvers*. PhD thesis, University of Reading, 2011.

[85] Y. K. Kwack and S. H. Ko. Numerical analysis for supercavitating flows around axisymmetric cavitators. *International Journal of Naval Architecture and Ocean Engineering*, 5(3):325–332, 2013.

[86] H.-Y. Kwak, K.-M. Kang, I. Ko, and J.-H. Kang. Fire-ball expansion and subsequent shock wave propagation from explosives detonation. *International Journal of Thermal Sciences*, 59:9–16, 2012.

[87] A. G. Lamorgese, D. Molin, and R. Mauri. Phase Field Approach to Multiphase Flow Modeling. *Milan Journal of Mathematics*, 79(2):597–642, 2011.

[88] S. Le Martelot, R. Saurel, and B. Nkonga. Towards the direct numerical simulation of nucleate boiling flows. *International Journal of Multiphase Flow*, 66:62–78, 2014.

[89] O. Le Métayer and R. Saurel. The noble-abel stiffened-gas equation of state. *Physics of Fluids*, 28(4):046102, 2016.

[90] D. Levy, G. Puppo, and G. Russo. Compact central WENO schemes for multidimensional conservation laws. *SIAM Journal of Scientific Computing*, 22:656–672, 2000.

[91] Q. Li, K. H. Luo, Q. J. Kang, Y. L. He, Q. Chen, and Q. Liu. Lattice Boltzmann methods for multiphase flow and phase-change heat transfer. *Progress in Energy and Combustion Science*, 52(March 2018):62–105, 2016.

[92] G. Linga and T. Flåtten. A hierarchy of non-equilibrium two-phase flow models. *ESAIM: Proceedings and Surveys*, 66(c):109–143, 2019.

[93] L. Lingquan, L. Rainald, K. P. Aditya, and H. L. A vertex-centered finite volume method with interface sharpening technique for compressible two-phase flows. *Journal of Computational Physics*, 460:111194, 2022.

[94] T. Liu, B. Khoo, and W. Xie. Isentropic one-fluid modelling of unsteady cavitating flow. *Journal of Computational Physics*, 201(1):80–108, 2004.

[95] L. Liviu, O. Sang-Yong, and H. Joerg. Dynamic response of anisotropic sandwich flat panels to underwater and in-air explosions. *International Journal of Solids and Structures*, 43(13):3794–3816, 2006.

[96] H. Lochon, F. Daude, P. Galon, and J. Hérard. HLLC-type Riemann solver with approximated two-phase contact for the computation of the Baer-Nunziato two-fluid model. *Journal of Computational Physics*, pages 733–762, 2016.

[97] H. Lund. A hierarchy of relaxation models for two-phase flow. *SIAM Journal on Applied Mathematics*, 72(6):1713–1741, 2012.

[98] H. Lund and P. Aursand. Two-phase flow of CO2 with phase transfer. *Energy Procedia*, 23:246–255, 2012.

[99] Z. H. Ma, D. M. Causon, L. Qian, H. B. Gu, C. G. Mingham, and P. Martínez Ferrer. A GPU based compressible multiphase hydrocode for modelling violent hydrodynamic impact problems. *Computers and Fluids*, 120:1–23, 2015.

[100] S. Majidi and A. Afshari. An adaptive interface sharpening methodology for compressible multiphase flows. *Computers and Mathematics with Applications*, 72(10):2660–2684, 2016.

[101] V. Maltsev, M. Skote, and P. Tsoutsanis. High-order methods for diffuse-interface models in compressible multi-medium flows: A review. *Physics of Fluids*, 34(2), 2022.

[102] A. Murrone and H. Guillard. A five equation reduced model for compressible two phase flow problems. *Journal of Computational Physics*, 202(2):664–698, 2005.

[103] V.-T. Nguyen, T.-H. Phan, and W.-G. Park. Numerical modeling of multiphase compressible flows with the presence of shock waves using an interface-sharpening five-equation model. *International Journal of Multiphase Flow*, 135:103542, 2021.

[104] R. R. Nourgaliev, T. N. Dinh, and T. G. Theofanous. Adaptive characteristics-based matching for compressible multifluid dynamics. *Journal of Computational Physics*, 213(2):500–529, 2006.

[105] C. Ollivier-Gooch and A. Jalali. Higher-order finite volume solution reconstruction on highly anisotropic meshes. *21st AIAA Computational Fluid Dynamics Conference*, pages 1–20, 06 2013.

[106] E. Olsson and G. Kreiss. A conservative level set method for two phase flow ii. *Journal of Computational Physics*, 225(1):785–807, 2007.

[107] A. Onuki. Dynamic van der waals theory. *Physical review. E, Statistical, nonlinear, and soft matter physics*, 75:036304, 04 2007.

[108] M. Oomar, A. Malan, B. Jones, R. Horwitz, and G. Langdon. An all-mach number hllc based scheme for multi-phase flow with surface tension. *Applied Sciences*, 11, 2021.

[109] P. L. Roe. Approximate Riemann Solvers, Parameter Vectors, and Difference Schemes. *Journal of Computational Physics*, 43:357–372, 1981.

[110] A. Pandare, H. Luo, and J. Bakosi. An enhanced ausm+-up scheme for high-speed compressible two-phase flows on hybrid grids. *Shock Waves*, 09 2018.

[111] A. K. Pandare, J. Waltz, and J. Bakosi. Multi-material hydrodynamics with algebraic sharp interface capturing. *Computers & Fluids*, 215:104804, 2021.

[112] M. Pelanti and K.-M. Shyue. A mixture-energy-consistent six-equation two-phase numerical model for fluids with interfaces, cavitation and evaporation waves. *Journal of Computational Physics*, 259:331–357, 2014.

[113] M. Pelanti and K.-M. Shyue. A numerical model for multiphase liquid–vapor–gas flows with interfaces and cavitation. *International Journal of Multiphase Flow*, 113:208–230, 2019.

[114] G. Perigaud and R. Saurel. A compressible flow model with capillary effects. *Journal of Computational Physics*, 209(1):139–178, 2005.

[115] F. Petitpas, J. Massoni, R. Saurel, E. Lapebie, and L. Munier. Diffuse interface model for high speed cavitating underwater systems. *International Journal of Multiphase Flow*, 35(8):747–759, 2009.

[116] F. Petitpas, J. Massoni, R. Saurel, E. Lapébie, and L. Munier. Diffuse interface model for high speed cavitating underwater systems. *International Journal of Multiphase Flow*, 35:747–759, 08 2009.

[117] F. Petitpas, R. Saurel, B.-K. Ahn, and S. Ko. Modelling cavitating flow around underwater missiles. *International Journal of Naval Architecture and Ocean Engineering*, 3(4):263–273, 2011.

[118] N. V. Petrov and A. A. Schmidt. Multiphase phenomena in underwater explosion. *Experimental Thermal and Fluid Science*, 60(May):367–373, 2015.

[119] M. A. Price, V.-T. Nguyen, O. Hassan, and K. Morgan. A method for compressible multimaterial flows with condensed phase explosive detonation and airblast on unstructured grids. *Computers and Fluids*, 111:76–90, 2015.

[120] B. Punsly, D. Balsara, J. Kim, and S. Garain. Riemann solvers and alfven waves in black hole magnetospheres. *Computational Astrophysics and Cosmology*, 3:1–12, 09 2016.

[121] J. J. Quirk and S. Karni. On the dynamics of a shock-bubble interaction. *Journal of Fluid Mechanics*, 318:129–163, 1996.

[122] M. I. Radulescu. On the noble-abel stiffened-gas equation of state. *Physics of Fluids*, 31(11):111702, 2019.

[123] S. M. Rahman and O. San. A relaxation filtering approach for two-dimensional rayleigh–taylor instability-induced flows. *Fluids*, 4(2), 2019.

[124] L. Rayleigh. On the theory of surface forces.-II Compressible fluids. *Phil. Mag.*, 33:209–220, 1892.

[125] S. Rhebergen, O. Bokhove, and J. J. van der Vegt. Discontinuous Galerkin finite element methods for hyperbolic nonconservative partial differential equations. *Journal of Computational Physics*, 227(3):1887–1922, 2008.

[126] S. Richard, F. Petitpas, and R. A. Berry. Simple and efficient relaxation methods for interfaces separating compressible fluids, cavitating flows and shocks in multiphase mixtures. *Journal of Computational Physics*, 228(5):1678–1712, 2009.

[127] M. G. Rodio and R. Abgrall. An innovative phase transition modeling for reproducing cavitation through a five-equation model and theoretical generalization to six and seven-equation models. *International Journal of Heat and Mass Transfer*, 89:1386–1401, 2015.

[128] E. Romenski, G. Reshetova, and I. Peshkov. Thermodynamically compatible hyperbolic model of a compressible multiphase flow in a deformable porous medium and its application to wavefields modeling. *AIP Conference Proceedings*, 2448:2–19, 2021.

[129] E. Romenski and E. Toro. Compressible two-phase flows: two-pressure models and numerical methods. *Comput. Fluid Dyn. J.*, 13:1–31, 2004.

[130] J. Rowlinson. Translation of J. D. van der Waals' "The thermodynamik theory of capillarity under the hypothesis of a continuous variation of density. *Journal of Statistical Physics*, 20:197–200, 1979.

[131] A. Rémi, B. Paola, and R. Barbara. On the simulation of multicomponent and multiphase compressible flows. *Computers and Fluids*, 64:43–63, 2020.

[132] P. S. Kevin, D. Eric, F. Nicolas, and G. Sergey. A model and numerical method for compressible flows with capillary effects. *Journal of Computational Physics*, 334:468–496, 2017.

[133] R. Saurel and R. Abgrall. Simple method for compressible multifluid flows. *SIAM Journal of Scientific Computing*, 21(3):1115–1145, 1999.

[134] R. Saurel, J. P. Cocchi, and P. B. Butler. Numerical study of cavitation in the wake of a hypervelocity underwater projectile. *Journal of Propulsion and Power*, 15(4):513–522, 1999.

[135] R. Saurel and O. Lemetayer. A multiphase model for compressible flows with interfaces, shocks, detonation waves and cavitation. *Journal of Fluid Mechanics*, 431:239–271, 2001.

[136] R. Saurel and C. Pantano. Diffuse-interface capturing methods for compressible two-phase flows. *Annual Review of Fluid Mechanics*, 50(1):105–130, 2018.

[137] R. Saurel, F. Petitpas, and R. Abgrall. Modelling phase transition in metastable liquids: application to cavitating and flashing flows. *Journal of Fluid Mechanics*, 607:313–350, 2008.

[138] K. Schmidmayer, S. H. Bryngelson, and T. Colonius. An assessment of multicomponent flow models and interface capturing schemes for spherical bubble dynamics. *Journal of Computational Physics*, 402:109080, 2020.

[139] K. Schmidmayer, F. Petitpas, S. Le Martelot, and E. Daniel. ECOGEN: An open-source tool for multiphase, compressible, multiphysics flows. *Computer Physics Communications*, 251:107093, 2019.

[140] D. Schmidt, C. Rutland, and M. Corradini. A fully compressible, two-dimensional model of small, high-speed, cavitating nozzles. *Atomization and Sprays*, 9:255–276, 05 1999.

[141] S.D.Poisson. Nouvelle the´orie de l'action capillaire. *Bachelier P´ere et Fils, Paris*, pages 1–306, 1831.

[142] R. K. Shukla. Nonlinear preconditioning for efficient and accurate interface capturing in simulation of multicomponent compressible flows. *Journal of Computational Physics*, 276:508–540, 2014.

[143] R. K. Shukla, C. Pantano, and J. B. Freund. An interface capturing method for the simulation of multi-phase compressible flows. *Journal of Computational Physics*, 229(19):7411–7439, 2010.

[144] K.-M. Shyue. A fluid-mixture type algorithm for compressible multicomponent flow with van der waals equation of state. *Journal of Computational Physics*, 156(1):43–88, 1999.

[145] K.-M. Shyue. A fluid-mixture type algorithm for compressible multicomponent flow with mie–grüneisen equation of state. *Journal of Computational Physics*, 171(2):678–707, 2001.

[146] K. M. Shyue. A wave-propagation based volume tracking method for compressible multicomponent flow in two space dimensions. *Journal of Computational Physics*, 215(1):219–244, 2006.

[147] K.-M. Shyue. An Anti-Diffusion based Eulerian Interface-Sharpening Algorithm

for Compressible Two-Phase Flow with Cavitation. *Proceedings of the 8th International Symposium on Cavitation*, 268(May):7–12, 2012.

[148] K. M. Shyue and F. Xiao. An Eulerian Interface Sharpening Algorithm for Compressible Two-phase Flow: The Algebraic THINC Approach. *Journal of Computational Physics*, 268:326–354, 2014.

[149] E. D. Siggia. Late stages of spinodal decomposition in binary mixtures. *Phys. Rev. A*, 20:595–605, 1979.

[150] P. Silva, P. Tsoutsanis, and A. Antoniadis. Simple multiple reference frame for high-order solution of hovering rotors with and without ground effect. *Aerospace Science and Technology*, 111, 2021.

[151] N. Simmonds, P. Tsoutsanis, A. Antoniadis, K. Jenkins, and A. Gaylard. Low-mach number treatment for finite-volume schemes on unstructured meshes. *Applied Mathematics and Computation*, 336:368–393, 2018.

[152] N. Simmonds, P. Tsoutsanis, and A. Gaylard. Implementation ofa low-mach number modification for high-order finite-volume schemes for arbitrary hybrid unstructured meshes. *ECCOMAS Congress 2016 - Proceedings of the 7th European Congress on Computational Methods in Applied Sciences and Engineering*, 2:2900–2915, 2016.

[153] K. So, X. Hu, and N. Adams. Anti-diffusion interface sharpening technique for two-phase compressible flow simulations. *Journal of Computational Physics*, 231(11):4304–4323, 2012.

[154] M. Sommerfeld. *Numerical Methods for Dispersed Multiphase Flows*, pages 327–396. Springer, Cham, 07 2017.

[155] S.Richard, B.Pierre, and L. Olivier. A general formulation for cavitating, boiling and evaporating flows. *Computers & Fluids*, 128:53–64, 2016.

[156] H. Srinivasan and P. Tsoutsanis. Adaptive mesh refinement techniques for high-order finite-volume weno schemes. *ECCOMAS Congress 2016 - Proceedings of the 7th European Congress on Computational Methods in Applied Sciences and Engineering*, 2:2883–2899, 2016.

[157] S. Suhas, M. Ali, and M. Parviz. A conservative diffuse-interface method for compressible two-phase flows. *Journal of Computational Physics*, 418:109606, 2020.

[158] N. Taku, K. Keiichi, and F. Kozo. A simple interface sharpening technique with a hyperbolic tangent function applied to compressible two-fluid modeling. *Journal of Computational Physics*, 258:95–117, 2014.

[159] H. Tang and D. Huang. A second-order accurate capturing scheme for 1d inviscid flows of gas and water with vacuum zones. *Journal of Computational Physics*, 128(2):301–318, 1996.

[160] H. Terashima and G. Tryggvason. A front-tracking/ghost-fluid method for fluid interfaces in compressible flows. *Journal of Computational Physics*, 228(11):4012–4037, 2009.

[161] F. Thein, E. Romenski, and M. Dumbser. Exact and Numerical Solutions of the Riemann Problem for a Conservative Model of Compressible Two-Phase Flows. *Journal of Scientific Computing*, 93(3):1–60, 2022.

[162] B. Tian, E. Toro, and C. Castro. A path-conservative method for a five-equation model of two-phase flow with an hllc-type riemann solver. *Computers Fluids*, 46:122–132, 07 2011.

[163] V. A. Titarev, P. Tsoutsanis, and D. Drikakis. {W}{E}{N}{O} Schemes for Mixed-element Unstructured Meshes. *Communications in Computational Physics*, 8(3):585–609, 2010.

[164] A. Tiwari, J. B. Freund, and C. Pantano. A diffuse interface model with immiscibility preservation. *Journal of Computational Physics*, 252:290–309, 2013.

[165] S. A. Tokareva and E. F. Toro. A flux splitting method for the Baer–Nunziato equations of compressible two-phase flow. *Journal of Computational Physics*, 323:45–74, 2016.

[166] E. F. Toro. Riemann Solvers and Numerical Methods for Fluid Dynamics—A Practical Introduction. *Springer-Verlag, Berlin Heidelberg*, 2nd Edition:624, 1999.

[167] G. Tryggvason, B. Bunner, A. Esmaeeli, D. Juric, N. Al-Rawahi, W. Tauber, J. Han, S. Nas, and Y.-J. Jan. A Front-Tracking Method for the Computations of Multiphase Flow. *Journal of Computational Physics*, 169(2):708–759, 2001.

[168] P. Tsoutsanis. *Very High-order Methods for 3D Arbitrary Unstructured Grid*. PhD thesis, Cranfield University, United Kingdom, 2009.

[169] P. Tsoutsanis. KNL Performance Comparison UCNS3D. *ARCHER performance report*, pages 157–170, 2017.

[170] P. Tsoutsanis. Extended bounds limiter for high-order finite-volume schemes on unstructured meshes. *Journal of Computational Physics*, 362:69–94, 2018.

[171] P. Tsoutsanis. Stencil selection algorithms for weno schemes on unstructured meshes. *Journal of Computational Physics*, 475, 2023.

[172] P. Tsoutsanis, E. Adebayo, A. Merino, A. Arjona, and M. Skote. Cweno finite-volume interface capturing schemes for multicomponent flows using unstructured meshes. *Journal of Scientific Computing*, 89(3), 2021.

[173] P. Tsoutsanis, A. Antoniadis, and D. Drikakis. Weno schemes on arbitrary unstructured meshes for laminar, transitional and turbulent flows. *Journal of Computational Physics*, 256:254–276, 2014.

[174] P. Tsoutsanis, A. Antoniadis, and K. Jenkins. Improvement of the computational performance of a parallel unstructured weno finite volume cfd code for implicit large eddy simulation. *Computers and Fluids*, 173:157–170, 2018.

[175] P. Tsoutsanis and D. Drikakis. A high-order finite-volume method for atmospheric flows on unstructured grids. *Journal of Coupled Systems and Multiscale Dynamics*, 4:170–186, 2016.

[176] P. Tsoutsanis and D. Drikakis. Addressing the challenges of implementation of high-order finite-volume schemes for atmospheric dynamics on unstructured meshes. *ECCOMAS Congress 2016 - Proceedings of the 7th European Congress on Computational Methods in Applied Sciences and Engineering*, 1:684–708, 2016.

[177] P. Tsoutsanis and M. Dumbser. Arbitrary high order central non-oscillatory schemes on mixed-element unstructured meshes. *Computers and Fluids*, 225, 2021.

[178] P. Tsoutsanis, I. W. Kokkinakis, L. Konozsy, D. Drikakis, R. J. R. Williams, and D. L. Youngs. Comparison of structured- and unstructured-grid, compressible and incompressible methods using the vortex pairing problem. *Computer Methods in Applied Mechanics and Engineering*, 293:207–231, 2015.

[179] P. Tsoutsanis, M. Pavan Kumar, and P. Farmakis. A relaxed a posteriori mood algorithm for multicomponent compressible flows using high-order finite-volume methods on unstructured meshes. *Applied Mathematics and Computation*, 437, 2023.

[180] P. Tsoutsanis, V. Titarev, and D. Drikakis. Weno schemes on arbitrary mixed-element unstructured meshes in three space dimensions. *Journal of Computational Physics*, 230(4):1585–1601, 2011.

[181] G. Wang, S. Zhang, M. Yu, H. Li, and Y. Kong. Investigation of the shock wave

propagation characteristics and cavitation effects of underwater explosion near boundaries. *Applied Ocean Research*, 46:40–53, 2014.

[182] Q. Wang, R. Deiterding, J. Pan, and Y.-X. Ren. Consistent high resolution interface-capturing finite volume method for compressible multi-material flows. *Computers & Fluids*, 202:104518, 2020.

[183] Z. Wang, K. Fidkowski, R. Abgrall, F. Bassi, D. Caraeni, A. Cary, H. Deconinck, R. Hartmann, K. Hillewaert, H. Huynh, N. Kroll, G. May, P.-O. Persson, B. van Leer, and M. Visbal. High-order cfd methods: Current status and perspective. *International Journal for Numerical Methods in Fluids*, 72:811–845, 2013.

[184] A. B. Wardlaw and J. A. Luton. Fluid-structure interaction mechanisms for close-in explosions. *Shock and Vibration*, 7(5):265–275, 2000.

[185] X. Wenfeng. A numerical simulation of underwater shock-cavitation-structure interaction. *PhD Thesis*, 53(March 2005):1–207, 2005.

[186] S. Whitaker. *The Method of Volume Averaging*. Kluwer Academic, 01 1999.

[187] M. L. Wong and S. K. Lele. High-order localized dissipation weighted compact nonlinear scheme for shock- and interface-capturing in compressible flows. *Journal of Computational Physics*, 339:179–209, 2017.

[188] Z. Wu, Z. Zong, and L. Sun. A mie-grüneisen mixture eulerian model for underwater explosion. *Engineering Computations*, 31:425–452, 2014.

[189] W. Xie, T. Liu, and B. Khoo. Application of a one-fluid model for large scale homogeneous unsteady cavitation: The modified schmidt model. *Computers & Fluids*, 35:1177–1192, 12 2006.

[190] W. Xie, Y. Young, T. Liu, and B. Khoo. Dynamic response of deformable structures subjected to shock load and cavitation reload. *Computational Mechanics*, 40(4):667–681, 2007.

[191] W. F. Xie, T. G. Liu, and B. C. Khoo. The simulation of cavitating flows induced by underwater shock and free surface interaction. *Applied Numerical Mathematics*, 57(5):734–745, 2007.

[192] G. S. Yeom and K. S. Chang. A modified HLLC-type Riemann solver for the compressible six-equation two-fluid model. *Computers and Fluids*, 76:86–104, 2013.

[193] D. Yingtang, Z. Lanhao, M. Jia, and A. Eldad. A resolved CFD-DEM-IBM algorithm for water entry problems. *Ocean Engineering*, 240(June):110014, 2021.

[194] Y.-L. Yoo, J.-C. Kim, and H.-G. Sung. Homogeneous mixture model simulation of compressible multi-phase flows at all mach number. *International Journal of Multiphase Flow*, 143:103745, 2021.

[195] J. Yu, H. Li, Z. Sheng, Y. Hao, and J. Liu. Numerical research on the cavitation effect induced by underwater multi-point explosion near free surface. *AIP Advances*, 13(1):015021, 2023.

[196] J. Yu, J. Liu, H. Wang, J. Wang, Z.-t. Zhou, and H. Mao. Application of two-phase transition model in underwater explosion cavitation based on compressible multiphase flows. *AIP Advances*, 12(2), 02 2022.

[197] A. Zein. *Numerical methods for multiphase mixture conservation laws with phase transition*. PhD thesis, Otto-von-Guericke-Universit¨at Magdeburg, 2010.

[198] A. Zein, M. Hantke, and G. Warnecke. Modeling phase transition for compressible two-phase flows applied to metastable liquids. *Journal of Computational Physics*, 229(8):2964–2998, 2010.

[199] J. Zhang. A simple and effective five-equation two-phase numerical model for liquid-vapor phase transition in cavitating flows. *International Journal of Multiphase Flow*, 132:1–47, 2020.

[200] Y. Zhang, W. YU, J. Liang, J. Lang, and D. Li. Three-dimensional numerical simulation for plastic injection-compression molding. *Frontiers of Mechanical Engineering*, 13(1):74, 2018.

[201] Z. F. Zhang, C. Wang, L. K. Wang, A. M. Zhang, and V. V. Silberschmidt. Underwater explosion of cylindrical charge near plates: Analysis of pressure characteristics and cavitation effects. *International Journal of Impact Engineering*, 121:91–105, 2018.

[202] Z. F. Zhang, C. Wang, A. M. Zhang, V. V. Silberschmidt, and L. K. Wang. SPH-BEM simulation of underwater explosion and bubble dynamics near rigid wall. *Science China Technological Sciences*, 62(7):1082–1093, 2019.

[203] Z. Zhao, J. Rong, and S. Zhang. An interface sharpening technique for the simulation of underwater explosions. *Ocean Engineering*, 266:112922, 2022.

[204] H. Zhu, J. Qiu, and J. Zhu. A simple, high-order and compact WENO limiter for RKDG method. *Computers & Mathematics with Applications*, 79(2):317–336, 2020.

Appendix A

Additional contours for 3D test cases

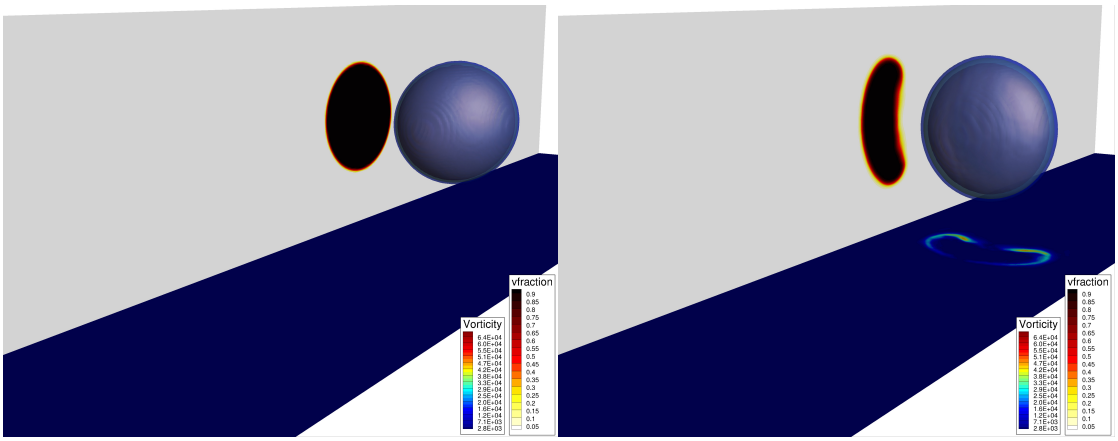

(a) $t = 00\mu s$ (b) $t = 220\mu s$

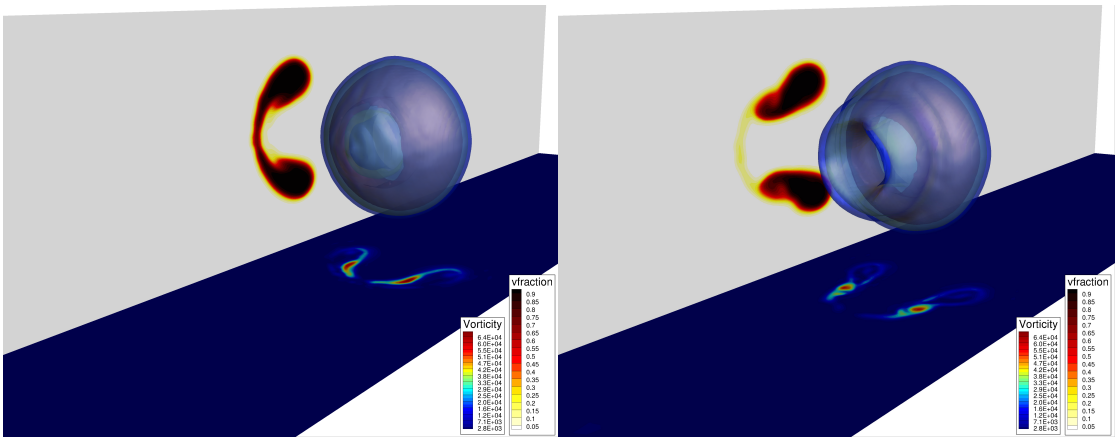

(c) $t = 400\mu s$ (d) $t = 600\mu s$

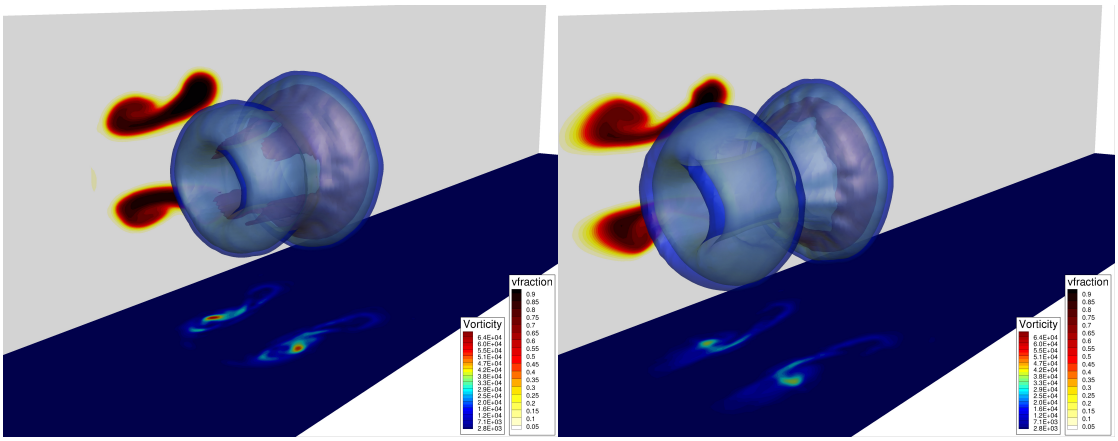

(e) $t = 810\mu s$ (f) $t = 980\mu s$

Figure A.1: Contour plots of volume fraction, vorticity magnitude at the centre of the computational domain and isosurfaces of three levels of volume fraction (0.25, 0.5, 0.9) of the computed solution of the shockwave 3D helium bubble interaction test problem at different instants.

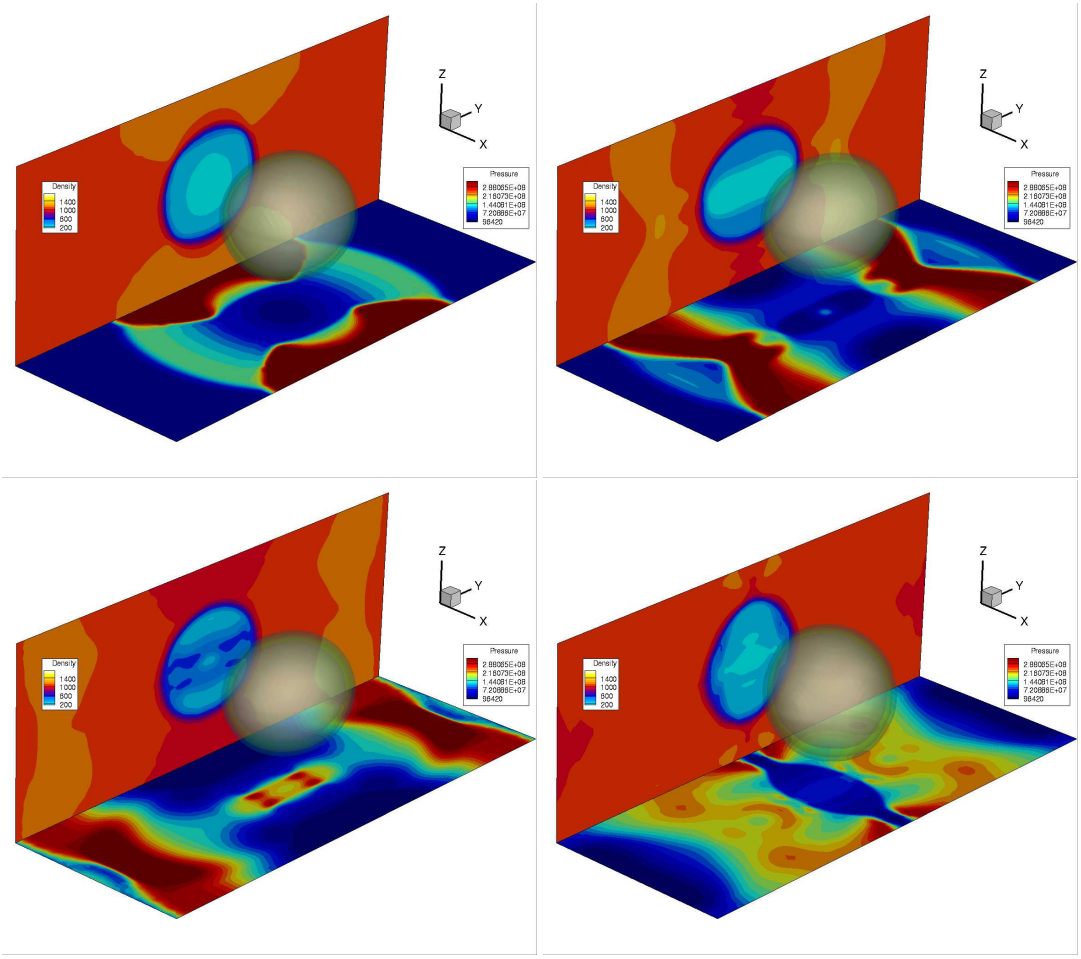

Figure A.2: Contour plots for 3D underwater explosion in an enclosed cylinder. Displayed are the colour maps of density and pressure fields on the central cross-sections and the iso-surface of the volume fraction of 0.5 that represents the moving interface at different instants.

Appendix B

FORTRAN code of the initial conditions

B.1 Multi-species advection convergence study

```
IF (INITCOND.EQ.403)THEN
!TEST CASE 4.1 OF WANG, DEITERDING, PAN and REN


MP_R(1)=7.0D0
MP_R(2)=1.0D0
MP_A(1)=0.5D0+0.25d0*(SIN(PI*((pox(1)-1.0d0)+0.5d0)))
MP_A(2)=1.0D0-MP_A(1)
U1=1.0D0
V1=0.0D0
P1=1.0D0/1.4D0



R1=(MP_R(1)*MP_A(1))+(MP_R(2)*MP_A(2))
MP_IE(1)=((P1+(GAMMA_IN(1)*MP_PINF(1)))/((GAMMA_IN(1)-1.0D0)))
MP_IE(2)=((P1+(GAMMA_IN(2)*MP_PINF(2)))/((GAMMA_IN(2)-1.0D0)))
IE1=(MP_IE(1)*MP_A(1))+(MP_IE(2)*MP_A(2))
```

```
SKIN1=(OO2)*((U1**2)+(V1**2))

E1=(R1*SKIN1)+IE1

!VECTOR OF CONSERVED VARIABLES NOW


VECCOS(1)=R1

VECCOS(2)=R1*U1

VECCOS(3)=R1*V1

VECCOS(4)=E1

VECCOS(5)=MP_R(1)*MP_A(1)

VECCOS(6)=MP_R(2)*MP_A(2)

VECCOS(7)=MP_A(1)



END IF
```

B.2 Advection of contact discontinuity

```
IF (INITCOND.EQ.402)THEN


if ((pox(1).ge.0.25).and.(pox(1).lt.0.75))then

MP_R(1)=10.0D0

MP_R(2)=1.0D0

MP_A(1)=1.0D0

MP_A(2)=0.0D0

U1=0.5D0

V1=0.0D0

P1=1.0D0/1.4D0
```

```
else
MP_R(1)=10.0D0
MP_R(2)=1.0D0
MP_A(1)=0.0D0
MP_A(2)=1.0D0
U1=0.5D0
V1=0.0D0
P1=1.0D0/1.4D0

end if

R1=(MP_R(1)*MP_A(1))+(MP_R(2)*MP_A(2))
MP_IE(1)=((P1+(GAMMA_IN(1)*MP_PINF(1)))/((GAMMA_IN(1)-1.0D0)))
MP_IE(2)=((P1+(GAMMA_IN(2)*MP_PINF(2)))/((GAMMA_IN(2)-1.0D0)))
IE1=(MP_IE(1)*MP_A(1))+(MP_IE(2)*MP_A(2))
SKIN1=(OO2)*((U1**2)+(V1**2))
E1=(R1*SKIN1)+IE1
!VECTOR OF CONSERVED VARIABLES NOW

VECCOS(1)=R1
VECCOS(2)=R1*U1
VECCOS(3)=R1*V1
VECCOS(4)=E1
VECCOS(5)=MP_R(1)*MP_A(1)
VECCOS(6)=MP_R(2)*MP_A(2)
VECCOS(7)=MP_A(1)

END IF
```

B.3 Gas bubble collapse in water

```
IF (INITCOND.EQ.411)THEN
!air_abubble_case

!GAMMA_IN(1) = 4.4 ! Water
!GAMMA_IN(2) = 1.4  ! Air
!MP_PINF(1) = 6e8 !Water from Coralic and Colonius or 2.218e8(abgrall203)
!MP_PINF(2) = 0 ! Air

IF (POX(1).LE.0.0066D0)THEN
MP_R(2)=1323.65d0  ! Water density
MP_R(1)=1d0  ! Air density
MP_A(2)=1.0D0  ! Water volume fraction (everything is water here)
MP_A(1)=0.0D0  ! Air volume fraction
U1=681.058D0    ! m/s
V1= 0.0D0
P1=1.9e9       ! Pa


R1=(MP_R(1)*MP_A(1))+(MP_R(2)*MP_A(2))
MP_IE(1)=((P1+(GAMMA_IN(1)*MP_PINF(1)))/((GAMMA_IN(1)-1.0D0)))
MP_IE(2)=((P1+(GAMMA_IN(2)*MP_PINF(2)))/((GAMMA_IN(2)-1.0D0)))
IE1=(MP_IE(1)*MP_A(1))+(MP_IE(2)*MP_A(2))
SKIN1=(OO2)*((U1**2)+(V1**2))
E1=(R1*SKIN1)+IE1
```

```
!VECTOR OF CONSERVED VARIABLES NOW

ELSE

!FIRST WITHIN BUBBLE REGION

if (sqrt(((pox(1)-0.012)**2)+((poy(1)-0.012)**2)).LE.0.003d0)then
MP_R(2)=1000.00d0  ! Water density
MP_R(1)=1d0  ! Air density
MP_A(2)=0.0D0  ! Water volume fraction (everything is water here)
MP_A(1)=1.0D0  ! Air volume fraction
U1= 0.0D0    ! m/s
V1= 0.0D0
P1= 100000     ! Pa

R1=(MP_R(1)*MP_A(1))+(MP_R(2)*MP_A(2))
MP_IE(1)=((P1+(GAMMA_IN(1)*MP_PINF(1)))/((GAMMA_IN(1)-1.0D0)))
MP_IE(2)=((P1+(GAMMA_IN(2)*MP_PINF(2)))/((GAMMA_IN(2)-1.0D0)))
IE1=(MP_IE(1)*MP_A(1))+(MP_IE(2)*MP_A(2))
SKIN1=(OO2)*((U1**2)+(V1**2))
E1=(R1*SKIN1)+IE1
!VECTOR OF CONSERVED VARIABLES NOW


else

MP_R(2)=1000.0d0  ! Water density
MP_R(1)=1d0  ! Air density
```

```
MP_A(2)=1.0D0  ! Water volume fraction (everything is water here)
MP_A(1)=0.0D0  ! Air volume fraction
U1= 0.0D0    ! m/s
V1= 0.0D0
P1= 100000     ! Pa


R1=(MP_R(1)*MP_A(1))+(MP_R(2)*MP_A(2))
MP_IE(1)=((P1+(GAMMA_IN(1)*MP_PINF(1)))/((GAMMA_IN(1)-1.0D0)))
MP_IE(2)=((P1+(GAMMA_IN(2)*MP_PINF(2)))/((GAMMA_IN(2)-1.0D0)))
IE1=(MP_IE(1)*MP_A(1))+(MP_IE(2)*MP_A(2))
SKIN1=(OO2)*((U1**2)+(V1**2))
E1=(R1*SKIN1)+IE1

!VECTOR OF CONSERVED VARIABLES NOW
end if

END IF

VECCOS(1)=R1
VECCOS(2)=R1*U1
VECCOS(3)=R1*V1
VECCOS(4)=E1
VECCOS(5)=MP_R(1)*MP_A(1)
VECCOS(6)=MP_R(2)*MP_A(2)
VECCOS(7)=MP_A(1)

END IF
```

B.4 Shock-Helium bubble interaction

```
IF (INITCOND.EQ.405)THEN
!TEST CASE 4.5 OF CORALIC & COLONIUS

IF (POX(1).GT.0.1D0)THEN
MP_R(1)=0.166315789d0
MP_R(2)=1.658d0
MP_A(1)=0.0D0
MP_A(2)=1.0D0
U1=-114.49D0
V1= 0.0D0
P1=159060.0d0



R1=(MP_R(1)*MP_A(1))+(MP_R(2)*MP_A(2))
MP_IE(1)=((P1+(GAMMA_IN(1)*MP_PINF(1)))/((GAMMA_IN(1)-1.0D0)))
MP_IE(2)=((P1+(GAMMA_IN(2)*MP_PINF(2)))/((GAMMA_IN(2)-1.0D0)))
IE1=(MP_IE(1)*MP_A(1))+(MP_IE(2)*MP_A(2))
SKIN1=(OO2)*((U1**2)+(V1**2))
E1=(R1*SKIN1)+IE1
!VECTOR OF CONSERVED VARIABLES NOW

ELSE

!FIRST WITHIN BUBBLE REGION

if (sqrt(((pox(1)-0.05d0)**2)+((poy(1)-0.05d0)**2)).LE.0.025d0)then
```

```
MP_R(1)=0.166315789d0

MP_R(2)=1.204D0

MP_A(1)=0.95d0

MP_A(2)=0.05D0

U1=0.0D0

V1=0.0D0

P1=101325


R1=(MP_R(1)*MP_A(1))+(MP_R(2)*MP_A(2))

MP_IE(1)=((P1+(GAMMA_IN(1)*MP_PINF(1)))/((GAMMA_IN(1)-1.0D0)))

MP_IE(2)=((P1+(GAMMA_IN(2)*MP_PINF(2)))/((GAMMA_IN(2)-1.0D0)))

IE1=(MP_IE(1)*MP_A(1))+(MP_IE(2)*MP_A(2))

SKIN1=(OO2)*((U1**2)+(V1**2))

E1=(R1*SKIN1)+IE1

!VECTOR OF CONSERVED VARIABLES NOW

else



MP_R(1)=0.166315789d0

MP_R(2)=1.204D0

MP_A(1)=0.0D0

MP_A(2)=1.0D0

U1=0.0D0

V1=0.0D0

P1=101325


R1=(MP_R(1)*MP_A(1))+(MP_R(2)*MP_A(2))

MP_IE(1)=((P1+(GAMMA_IN(1)*MP_PINF(1)))/((GAMMA_IN(1)-1.0D0)))
```

```
MP_IE(2)=((P1+(GAMMA_IN(2)*MP_PINF(2)))/((GAMMA_IN(2)-1.0D0)))

IE1=(MP_IE(1)*MP_A(1))+(MP_IE(2)*MP_A(2))

SKIN1=(OO2)*((U1**2)+(V1**2))

E1=(R1*SKIN1)+IE1


!VECTOR OF CONSERVED VARIABLES NOW

end if



END IF


VECCOS(1)=R1

VECCOS(2)=R1*U1

VECCOS(3)=R1*V1

VECCOS(4)=E1

VECCOS(5)=MP_R(1)*MP_A(1)

VECCOS(6)=MP_R(2)*MP_A(2)

VECCOS(7)=MP_A(1)



END IF



IF (INITCOND.EQ.406)THEN

!TEST CASE 4.5 OF CORALIC & COLONIUS


IF (POX(1).GT.0.1D0)THEN

MP_R(1)=0.166315789d0
```

```
MP_R(2)=1.658d0

MP_A(1)=0.0D0

MP_A(2)=1.0D0

U1=-114.49D0

V1= 0.0D0

P1=159060.0d0



R1=(MP_R(1)*MP_A(1))+(MP_R(2)*MP_A(2))

MP_IE(1)=((P1+(GAMMA_IN(1)*MP_PINF(1)))/((GAMMA_IN(1)-1.0D0)))

MP_IE(2)=((P1+(GAMMA_IN(2)*MP_PINF(2)))/((GAMMA_IN(2)-1.0D0)))

IE1=(MP_IE(1)*MP_A(1))+(MP_IE(2)*MP_A(2))

SKIN1=(OO2)*((U1**2)+(V1**2))

E1=(R1*SKIN1)+IE1

!VECTOR OF CONSERVED VARIABLES NOW


ELSE


!FIRST WITHIN BUBBLE REGION

u_cond1=0;u_cond2=0;u_cond3=0; u_cond4=0


 if (((pox(1).ge.0.01d0).and.(pox(1).le.0.02)).or.((pox(1).ge.0.03d0).and.(pox(1).l

    u_cond1=1

 end if

 if ((poy(1).ge.0.05d0).and.(poy(1).le.0.075))then

    u_cond2=1

 end if
```

```
 if ((poy(1).le.0.05d0).and.(poy(1).gt.0.02))then
    u_cond3=1
 end if
 if (u_cond3.eq.1)then
 if ((sqrt(((pox(1)-0.025d0)**2)+((poy(1)-0.05d0)**2)).LE.0.015d0).and.(sqrt(((pox(
    u_cond4=1
 end if
 end if


 if (((u_cond1.eq.1).and.(u_cond2.eq.1)).or.(u_cond4.eq.1))then

MP_R(1)=0.166315789d0
MP_R(2)=1.204D0
MP_A(1)=0.95d0
MP_A(2)=0.05D0
U1=0.0D0
V1=0.0D0
P1=101325

R1=(MP_R(1)*MP_A(1))+(MP_R(2)*MP_A(2))
MP_IE(1)=((P1+(GAMMA_IN(1)*MP_PINF(1)))/((GAMMA_IN(1)-1.0D0)))
MP_IE(2)=((P1+(GAMMA_IN(2)*MP_PINF(2)))/((GAMMA_IN(2)-1.0D0)))
IE1=(MP_IE(1)*MP_A(1))+(MP_IE(2)*MP_A(2))
SKIN1=(OO2)*((U1**2)+(V1**2))
E1=(R1*SKIN1)+IE1
!VECTOR OF CONSERVED VARIABLES NOW
```

```
else



MP_R(1)=0.166315789d0

MP_R(2)=1.204D0

MP_A(1)=0.0D0

MP_A(2)=1.0D0

U1=0.0D0

V1=0.0D0

P1=101325



R1=(MP_R(1)*MP_A(1))+(MP_R(2)*MP_A(2))

MP_IE(1)=((P1+(GAMMA_IN(1)*MP_PINF(1)))/((GAMMA_IN(1)-1.0D0)))

MP_IE(2)=((P1+(GAMMA_IN(2)*MP_PINF(2)))/((GAMMA_IN(2)-1.0D0)))

IE1=(MP_IE(1)*MP_A(1))+(MP_IE(2)*MP_A(2))

SKIN1=(OO2)*((U1**2)+(V1**2))

E1=(R1*SKIN1)+IE1

!VECTOR OF CONSERVED VARIABLES NOW

end if



END IF



VECCOS(1)=R1

VECCOS(2)=R1*U1
```

```
VECCOS(3)=R1*V1

VECCOS(4)=E1

VECCOS(5)=MP_R(1)*MP_A(1)

VECCOS(6)=MP_R(2)*MP_A(2)

VECCOS(7)=MP_A(1)



END IF
```

B.5 Underwater Explosion near a rigid wall

```
    IF (INITCOND.EQ.413)THEN
  !Under water Explosion first experiment gas-solid wall
  !Test Case from Z.H Ma et al

  !GAMMA_IN(1) = 7.15 !Water
  !GAMMA_IN(2) = 2.0  !Explosive
  !MP_PINF(1) = 6e8   !Water from Coralic and Colonius or 2.218e8(abgrall203)
  !MP_PINF(2) = 0     !Explosive



  !FIRST WITHIN BUBBLE REGION


  if (sqrt(((pox(1)-0.00d0)**2)+((poy(1)-0.00d0)**2)).LE.1.0d0)then


MP_R(1)=1270d0 ! Pressured gas bubble
MP_R(2)=1000D0 ! Water density
```

```
MP_A(1)=1.0D0  ! Bubbles volume fraction
MP_A(2)=0.00D0 ! Water volume fraction (in the explosion zone)
U1=0.0D0       ! m/s
V1=0.0D0
P1=8.29e8

SKIN1=(OO2)*((U1**2)+(V1**2))
R1=(MP_R(1)*MP_A(1))+(MP_R(2)*MP_A(2))
MP_IE(1)=((P1+(GAMMA_IN(1)*MP_PINF(1)))/((GAMMA_IN(1)-1.0D0)))
MP_IE(2)=((P1+(GAMMA_IN(2)*MP_PINF(2)))/((GAMMA_IN(2)-1.0D0)))
IE1=(MP_IE(1)*MP_A(1))+(MP_IE(2)*MP_A(2))
 ! !KINETIC ENERGY FIRST!
SKIN1=(OO2)*((U1**2)+(V1**2))
! !TOTAL ENERGY
E1=R1*(SKIN1+IE1)
!VECTOR OF CONSERVED VARIABLES NOW
else


MP_R(1)=1270         ! Air density
MP_R(2)=1000.0d0           ! Water density
MP_A(1)=0.005D0     ! Air volume fraction
MP_A(2)=0.995D0     ! Water volume fraction (everything is water here)
U1= 0.0D0                ! m/s
V1= 0.0D0                  ! m/s
P1= 101325                ! Pa

SKIN1=(OO2)*((U1**2)+(V1**2))
```

```
R1=(MP_R(1)*MP_A(1))+(MP_R(2)*MP_A(2))
MP_IE(1)=((P1+(GAMMA_IN(1)*MP_PINF(1)))/((GAMMA_IN(1)-1.0D0)))
MP_IE(2)=((P1+(GAMMA_IN(2)*MP_PINF(2)))/((GAMMA_IN(2)-1.0D0)))

IE1=(MP_IE(1)*MP_A(1))+(MP_IE(2)*MP_A(2))

    ! !KINETIC ENERGY FIRST!
SKIN1=(OO2)*((U1**2)+(V1**2))
    ! !TOTAL ENERGY
E1=R1*(SKIN1+IE1)

    !VECTOR OF CONSERVED VARIABLES NOW

END IF

VECCOS(1)=R1
VECCOS(2)=R1*U1
VECCOS(3)=R1*V1
VECCOS(4)=E1
VECCOS(5)=MP_R(1)*MP_A(1)
VECCOS(6)=MP_R(2)*MP_A(2)
VECCOS(7)=MP_A(1)

END IF
```

B.6 Underwater Explosion near a free surface

```
IF (INITCOND.EQ.414)THEN


IF (POY(1).gt.0.0D0)THEN
 MP_R(1)=1.225   ! Air density
  MP_R(2)=1000        ! Water density
  MP_A(1)=1.0D0  ! Air volume fraction
  MP_A(2)=0.0D0  ! Water volume fraction (everything is water here)
  U1= 0.0D0    ! m/s
  V1= 0.0D0
  P1= 101325.0     ! Pa



else

  if (sqrt(((pox(1)-0.0)**2)+((poy(1)+0.3)**2)).LE.0.12d0)then
  MP_R(1)=1250d0      ! Pressured gas bubble
  MP_R(2)=1000          ! Water density
  MP_A(1)=1.0D0      ! Bubbles volume fraction
  MP_A(2)=0.0D0      ! Water volume fraction (in the explosion zone)
  U1= 0.0D0        ! m/s
  V1= 0.0D0
  P1= 1000000000.0


  else
  MP_R(1)=1.225  ! Air density
  MP_R(2)=1000.0d0    ! Water density
  MP_A(1)=0.0D0  ! Air volume fraction
```

```
  MP_A(2)=1.0D0  ! Water volume fraction (everything is water here)
  U1= 0.0D0    ! m/s
  V1= 0.0D0           ! m/s
  P1= 101325         ! Pa
  end if



end if


SKIN1=(OO2)*((U1**2)+(V1**2))
R1=(MP_R(1)*MP_A(1))+(MP_R(2)*MP_A(2))
! MP_IE(1)=((P1+(GAMMA_IN(1)*MP_PINF(1)))/((GAMMA_IN(1)-1.0D0)*MP_R(1)))
! MP_IE(2)=((P1+(GAMMA_IN(2)*MP_PINF(2)))/((GAMMA_IN(2)-1.0D0)*MP_R(2)))
MP_IE(1)=((P1+(GAMMA_IN(1)*MP_PINF(1)))/((GAMMA_IN(1)-1.0D0)))
MP_IE(2)=((P1+(GAMMA_IN(2)*MP_PINF(2)))/((GAMMA_IN(2)-1.0D0)))

IE1=(MP_IE(1)*MP_A(1))+(MP_IE(2)*MP_A(2))
SKIN1=(OO2)*((U1**2)+(V1**2))
E1=(R1*SKIN1)+IE1
!VECTOR OF CONSERVED VARIABLES NOW


VECCOS(1)=R1
VECCOS(2)=R1*U1
VECCOS(3)=R1*V1
VECCOS(4)=E1
```

```
VECCOS(5)=MP_R(1)*MP_A(1)

VECCOS(6)=MP_R(2)*MP_A(2)

VECCOS(7)=MP_A(1)


END IF
```

B.7 Underwater Explosion in a closed rigid cylinder

```
IF (INITCOND.EQ.415)THEN
  !Under water Explosion in a closed rigid cylinder
  !Test Case from Z.H Ma et al + XIe PHD


  !GAMMA_IN(1) = 7.15 !Water
  !GAMMA_IN(2) = 2.0  !Explosive
  !MP_PINF(1) = 6e8   !Water from Coralic and Colonius or 2.218e8(abgrall203)
  !MP_PINF(2) = 0     !Explosive



  !FIRST WITHIN BUBBLE REGION


if (sqrt(((pox(1)-0.00d0)**2)+((poy(1)-0.00d0)**2)+((poz(1)-0.00d0)**2)).LE.0.015d0


MP_R(1)=1770d0 ! Pressured gas bubble
MP_R(2)=1000D0 ! Water density
MP_A(1)=1.0D0  ! Bubbles volume fraction
MP_A(2)=0.0D0  ! Water volume fraction (in the explosion zone)
U1=0.0D0       ! m/s
V1=0.0D0
```

```
w1=0.0d0
P1=2e9

SKIN1=(OO2)*((U1**2)+(V1**2)+(w1**2))
R1=(MP_R(1)*MP_A(1))+(MP_R(2)*MP_A(2))

MP_IE(1)=((P1+(GAMMA_IN(1)*MP_PINF(1)))/((GAMMA_IN(1)-1.0D0)))
MP_IE(2)=((P1+(GAMMA_IN(2)*MP_PINF(2)))/((GAMMA_IN(2)-1.0D0)))

IE1=(MP_IE(1)*MP_A(1))+(MP_IE(2)*MP_A(2))
SKIN1=(OO2)*((U1**2)+(V1**2)+(w1**2))
E1=(R1*SKIN1)+IE1
!VECTOR OF CONSERVED VARIABLES NOW
else

MP_R(1)=1770       ! Air density
MP_R(2)=1000.0d0         ! Water density
MP_A(1)=0.015D0   ! Air volume fraction
MP_A(2)=0.985D0   ! Water volume fraction (everything is water here)
U1= 0.0D0              ! m/s
V1= 0.0D0                ! m/s
P1= 100000              ! Pa

SKIN1=(OO2)*((U1**2)+(V1**2)+(w1**2))
R1=(MP_R(1)*MP_A(1))+(MP_R(2)*MP_A(2))

MP_IE(1)=((P1+(GAMMA_IN(1)*MP_PINF(1)))/((GAMMA_IN(1)-1.0D0)))
MP_IE(2)=((P1+(GAMMA_IN(2)*MP_PINF(2)))/((GAMMA_IN(2)-1.0D0)))
```

```
IE1=(MP_IE(1)*MP_A(1))+(MP_IE(2)*MP_A(2))
SKIN1=(OO2)*((U1**2)+(V1**2)+(w1**2))
E1=(R1*SKIN1)+IE1



END IF



VECCOS(1)=R1
VECCOS(2)=R1*U1
VECCOS(3)=R1*V1
VECCOS(4)=R1*w1
VECCOS(5)=E1
VECCOS(6)=MP_R(1)*MP_A(1)
VECCOS(7)=MP_R(2)*MP_A(2)
VECCOS(8)=MP_A(1)

END IF
```

B.8 Underwater Explosion of two bubbles placed horizontally near a free surface

```
IF (INITCOND.EQ.416)THEN

IF (POY(1).gt.0.0D0)THEN
```

```
  MP_R(1)=1.225  ! Air density
  MP_R(2)=1000        ! Water density
  MP_A(1)=1.0D0  ! Air volume fraction
  MP_A(2)=0.0D0  ! Water volume fraction (everything is water here)
  U1= 0.0D0    ! m/s
  V1= 0.0D0
  P1= 101325.0     ! Pa



else

  if (sqrt(((pox(1)-0.45)**2)+((poy(1)+0.3)**2)).LE.0.12d0)then
  MP_R(1)=1250d0      ! Pressured gas bubble
  MP_R(2)=1000          ! Water density
  MP_A(1)=1.0D0      ! Bubbles volume fraction
  MP_A(2)=0.0D0      ! Water volume fraction (in the explosion zone)
  U1= 0.0D0          ! m/s
  V1= 0.0D0
  P1= 1000000000.0


else

  if (sqrt(((pox(1)+0.45)**2)+((poy(1)+0.3)**2)).LE.0.12d0)then
  MP_R(1)=1250d0      ! Pressured gas bubble
  MP_R(2)=1000          ! Water density
  MP_A(1)=1.0D0      ! Bubbles volume fraction
  MP_A(2)=0.0D0      ! Water volume fraction (in the explosion zone)
  U1= 0.0D0          ! m/s
```

```
  V1= 0.0D0
  P1= 1000000000.0



  else
  MP_R(1)=1.225  ! Air density
  MP_R(2)=1000.0d0    ! Water density
  MP_A(1)=0.0D0  ! Air volume fraction
  MP_A(2)=1.0D0  ! Water volume fraction (everything is water here)
  U1= 0.0D0    ! m/s
  V1= 0.0D0           ! m/s
  P1= 101325         ! Pa
  end if
  end if


end if



SKIN1=(OO2)*((U1**2)+(V1**2))
R1=(MP_R(1)*MP_A(1))+(MP_R(2)*MP_A(2))
! MP_IE(1)=((P1+(GAMMA_IN(1)*MP_PINF(1)))/((GAMMA_IN(1)-1.0D0)*MP_R(1)))
! MP_IE(2)=((P1+(GAMMA_IN(2)*MP_PINF(2)))/((GAMMA_IN(2)-1.0D0)*MP_R(2)))
MP_IE(1)=((P1+(GAMMA_IN(1)*MP_PINF(1)))/((GAMMA_IN(1)-1.0D0)))
MP_IE(2)=((P1+(GAMMA_IN(2)*MP_PINF(2)))/((GAMMA_IN(2)-1.0D0)))

IE1=(MP_IE(1)*MP_A(1))+(MP_IE(2)*MP_A(2))
SKIN1=(OO2)*((U1**2)+(V1**2))
```

```
E1=(R1*SKIN1)+IE1

!VECTOR OF CONSERVED VARIABLES NOW


VECCOS(1)=R1

VECCOS(2)=R1*U1

VECCOS(3)=R1*V1

VECCOS(4)=E1

VECCOS(5)=MP_R(1)*MP_A(1)

VECCOS(6)=MP_R(2)*MP_A(2)

VECCOS(7)=MP_A(1)


END IF
```